Politecnico di Torino

Politecnico di Torino

Physics of Complex Systems
A.y. 2024/2025
July 2025

Analysis and evaluation of past tropical cyclone trends, assessments and simulations regarding possible future scenario, using models provided by CMCC.

Supervisors:
Prof. Andrea Antonio Gamba

Candidate:
Simone Pinciolla

Co-Supervisors:
Prof. Paolo Oddo (UniBo)
Mr. Enrico Scoccimarro (CMCC)
Dr. Lorenzo Sangelantoni (CMCC)

Abstract

A tropical cyclone (TC) is a rapidly rotating storm that develops over oceans at tropical latitudes and can vary in speed, size, and intensity. Together with other extreme events, their growing impact on society is a consequence of climate change, induced by natural forcings and human activity, mostly through emissions of greenhouse gases (GHGs) that alter the chemistry of the atmosphere. This document presents one of the possible future scenarios concerning the evolution of TCs, using simulation ran by the CMCC-CM3-LT (Centro Euro-Mediterraneo sui Cambiamenti Climatici – Climate Model version 3) model for the present (1980–2010) and future climate (2070–2100) according to the SSP5-8.5 (Shared Socioeconomic Pathway #5) scenario. The reliability of the data produced by CMCC-CM3-LT is confirmed by comparison with observational and reanalysis datasets. Then, surface wind and mean sea level pressure (MSLP) variables are used as input for the TC tracking performed by CyTRACK. Based on Accumulated Cyclone Energy (ACE) and minimum central pressure (MCP), the model suggests an increasing trend in TC intensity in the Central and Eastern North Pacific Ocean and the North Indian Ocean. Conversely, an opposite tendency is observed in the South Pacific and in the regions of the Indian and Western Pacific Oceans at low latitudes. Although spatially heterogeneous, the Atlantic Ocean also shows a general decrease in ACE. Consistent with the evolution of ACE and MCP, the size of cyclones follows the variation in intensity, with TCs being larger when more intense and vice versa. Looking instead at the frequency with which TCs are generated, a clear upward trend is revealed near all coasts, as well as in the Central North Pacific Ocean and in a strip right below the equator in the Eastern Pacific Ocean. In contrast, a notable decrease in TC occurrence is projected for the Western Pacific and the Eastern Indian Ocean away from the Australian coasts. In terms of duration, future cyclones show a distribution similar to the present one, but with a shift toward shorter durations, suggesting a potential decrease in the persistence of extreme events. Hence, in regions where ACE remains unchanged or increases, this behavior suggests that the intensification is primarily driven by increased storm intensity rather than prolonged duration.

Contents

1 Introduction (objectives)

In recent years there has been a substantial growth in social and collective interest and sensitivity to climate change. Since the 1980s, after the Villach conferences among international scientists in the climate branch, the climate issue spread into international politics to deal with a problem that was understimated until then and that was evolving more rapidly than expected.
After the foundation of the Intergovernmental Panel on Climate Change (IPCC) on 1988, several international events in support of the cause occur, starting from The United Nations Framework Convention on Climate Change (UNFCCC). It is an international environmental treaty adopted on 9 May 1992 and entered into force on 21 March 1994, whose objective was to counter the dangerous human interference with the climate system ([1]). It was the framework of the Conference of Parties held yearly, which lead to the drafting of the Kyoto Protocol and to the Paris agreement (respectively COP3, COP21).
But what does the expression climate change stands for? And What is the difference between climate and weather?
As defined by the World Meteorological Organization (WMO), Climate is the average weather conditions for a particular location over a long period of time, ranging from months to thousands or millions of years. Climate change is instead any systematic change in the long-term statistics of climate variables such as temperature, precipitation, pressure, or wind sustained over several decades or longer, which can be induced by natural external forcing or by human activity. IPCC cited above was founded with the objective of providing review and recommendations with respect to the state of knowledge of the science of climate change, its social and economic impact, and potential response strategies and elements for inclusion in a possible future international convention on climate. Their results are made available through reports named Assessment Reports, whose latest is AR6. Results exposed on it tell how human activities, principally through emissions of greenhouse gases, have unequivocally caused global warming (graphs in figure 1 show the human activity and global warming correlation, [2]). Climate system is a complex system whose main components, atmosphere, hydrosphere, cryosphere, lithosphere and biosphere interact each other ([3]). However, these interactions occur through several processes and at different time scales ([4]). For example while the evaporation and precipitation formation take seconds to minutes to days to cycle water through the atmosphere, the water that falls onto ice sheets may remain there for hundreds of thousands of years. Or the variation of the energy budget varies for both the Earth's revolution (time order of the year), and for rotation (time order of day). The climate system, then, evolves in time not only for its own internal dynamics but also due to changes in external factors that are called 'forcings'. And along with natural phenomena such as volcanic eruptions and solar variations, a change on the atmospheric composition, as result of human activity, belongs to them ([5]). Since solar radiation powers the climate system, changing greenhouse gas concentrations modifes the radiation balance of the Earth, initiating a series of consequences over a longer or shorter period of time as anticipated in the previous lines, and thus making it difficult to study the system's responses. In figure 2 there is a simplified scheme the of radiation balance. It's then clear how an increase of GHGs concentration can match with raising of temperature, as figure 1 proved.

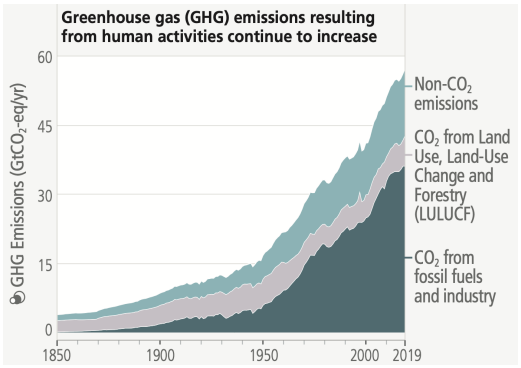

(a)

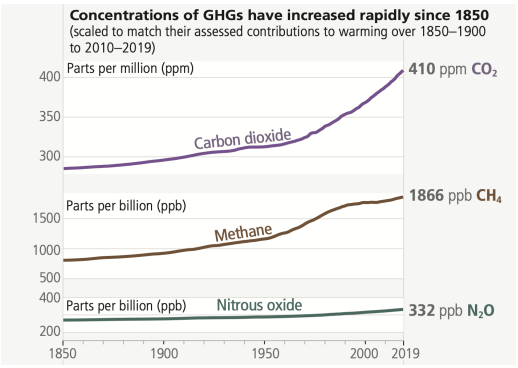

(b)

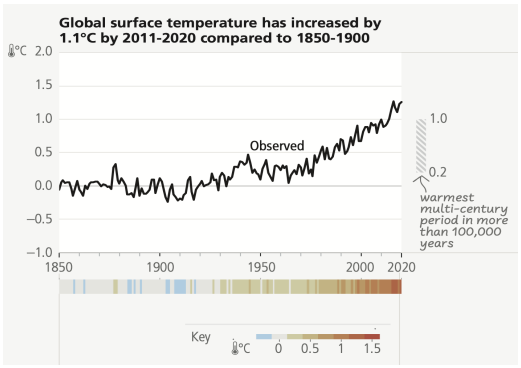

(c)

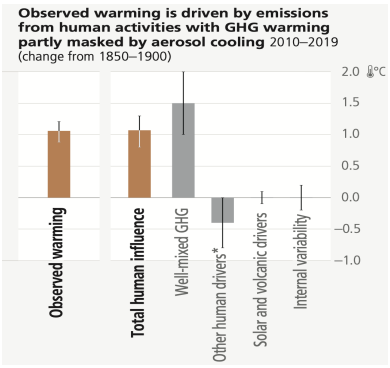

(d)

Figure 1: Scheme coming from [2] displaying the relation between emissions and global warming. In (a) the concentration increase of the 3 main GHGs, dued to emissions of (b). In (c) an observed global surface increase is recorded, while (d) prove the human complicity over it. Together the 4 images represent the causal chain from emissions to resulting rising temperatures, since the middle of the XX century.

Extreme events

Human-caused climate change is also responsible for many weather and climate extremes in every region across the globe. This has produced impacts on food and water security, human health, economies, society and related losses and damages to nature and people. Since after AR5, changes observed in extreme events such as heat waves, heavy rainfall, droughts, and tropical cyclones (TCs) are increasingly evident, as shown in figure 3 where the comparison is made with respect to the 1950s. According to IPCC climate change has negatively affected human physical health and, in some cases, mental health, contributing to humanitarian crises where climate risks interact with high vulnerability. The vulnerability of human, socioeconomic, and biological systems along with exposure to extreme events and change in the climate system are in fact linked to what are named climate-related risks (Figure 4). These variables are needed to provide greater clarity on the effects of climate change, especially extreme events, on society. As defined by AR5 ([7]) vulnerability corresponds to the propensity or predisposition to be adversely affected, while exposure is the

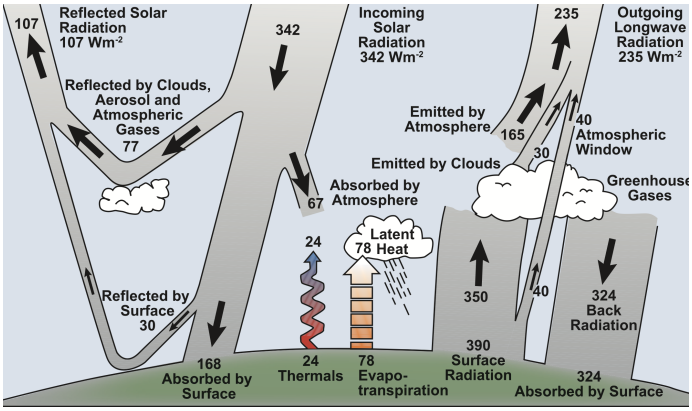

Figure 2: Estimate of the Earth's annual and global mean energy balance (from [5]), based on the study of Kiehl and Trenberth (1997), [6]. The units of the values in figure are $\frac{W}{m^2}$

presence of people, livelihoods, species or ecosystems, environmental functions, services, resources, infrastructure, or economic, social, or cultural assets in places and settings that could be negatively affected. The other factor which contributes to the risk increase are the hazards (Figure 4). They consist in potential occurrence of a natural or human-induced physical event or trend or physical impact that may cause loss of life, injury, or other health impacts, as well as damage and loss to property, infrastructure, livelihoods, service provision, ecosystems, and environmental resources. So high values of these factors are index of a warning value of the risk, often represented as probability of occurrence of hazardous events or trends multiplied by the impacts if these events or trends occur.

Tropical cyclones and their correlations with climate change

According to the WMO definition, a tropical cyclone is a rapidly rotating storm that begins over tropical oceans, that could vary in speed, size, and intensity. Depending on the location thy are named differently ([8]). They are defined hurricanes in the Caribbean Sea, the Gulf of Mexico, the North Atlantic Ocean and the Eastern and Central North Pacific Ocean, typhoons in the Western North Pacific Ocean, cyclones in the Bay of Bengal and Arabian Sea, in Western South Pacific and southeast Indian Ocean, they are called severe tropical cyclones and tropical cyclones in the southwest Indian Ocean, although tropical cyclone stands for all of them. They should include several hazards, such as extreme winds, heavy rainfall and flooding, which can interact each other, and hence increase the risk and impact on the society, through death or damage to infrastructure (more than 750,000 people have been killed by TCs since 1970). Referring to data obtained in different regions and in different periods, all between in a range between 1950 to 2005, TCs have a great impact on the total precipitation over global ocean basins. For example their contribution is up to 15%–20% of rainfall along the U.S. Gulf and Mexican coasts, 20%–30% in most of Taiwan and the China coastline south of 25°N, 30%–40% in most of Hainan and some locations of Taiwan and the coastline, 40%–45% in southernmost Taiwan and westernmost Hainan, and 50%–60% of the total rainfall between 18° and 26°N during peak TC season from July to October along 125°E ([9]).

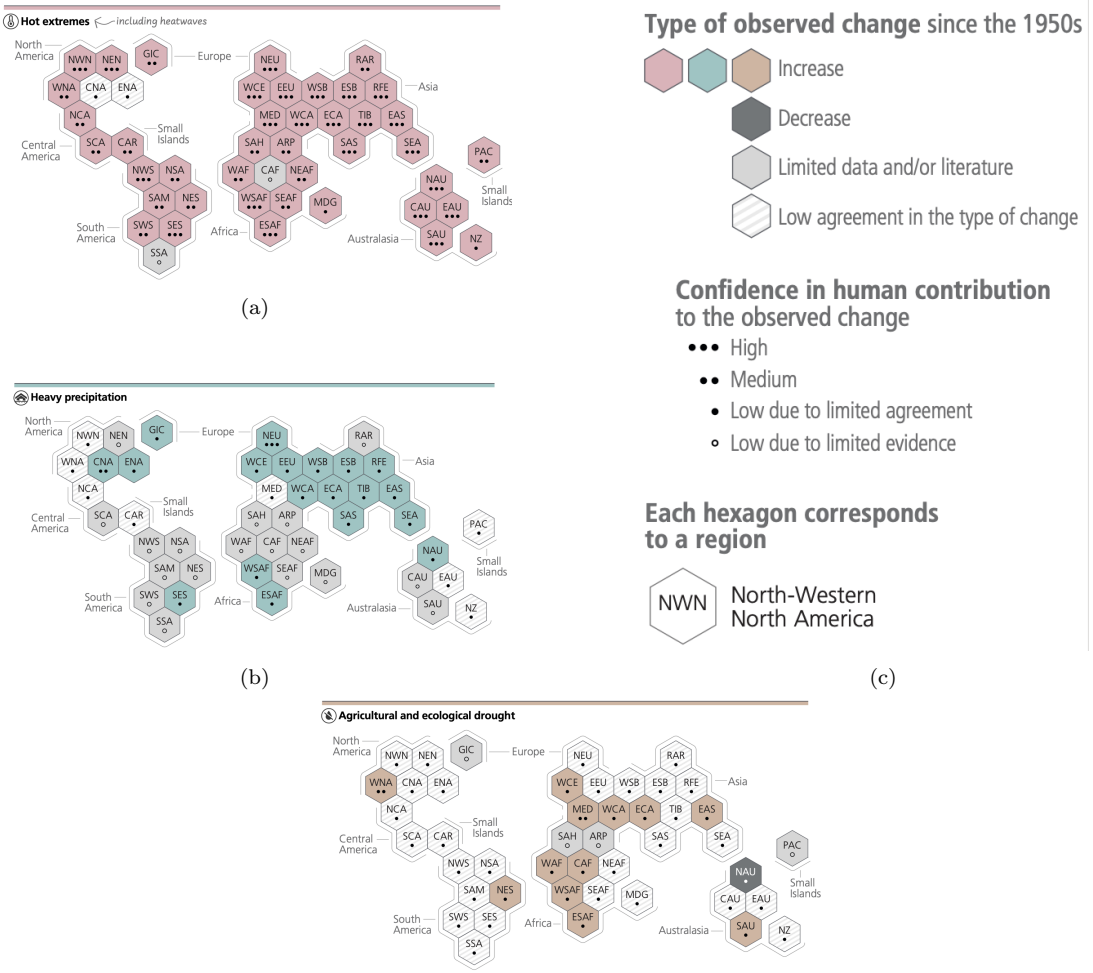

Figure 3: Representation of changing rate of extreme events occurrence (from [2]). While for hot extremes and heatwaves a global increase is recorded (3a), for drought and heavy precipitation about the half of regions suffered a growth of the two events. Note that concerning the rest of the planet there is no sufficient informations about them or there is low agreement in the type of change. Only in Northern Australia (NAU) a decrease in such extreme events is recorded (3d). Panel 3c gives informations about the structure of the three figures.

Focusing on their structure, TCs are composed by the eye, a warm and relatively calm area, the eyewall, where the most instense wind and raifalls occur, and the outer spiral rainbands extended for hundreds of km, as shown in figure 5. The cyclone intensification is fed by warm, moist air drawn towards the inner core, which, rising along the eyewall, cools by adiabatic expansion and releases latent heat by condensation. This raises temperatures in the middle and upper troposphere,

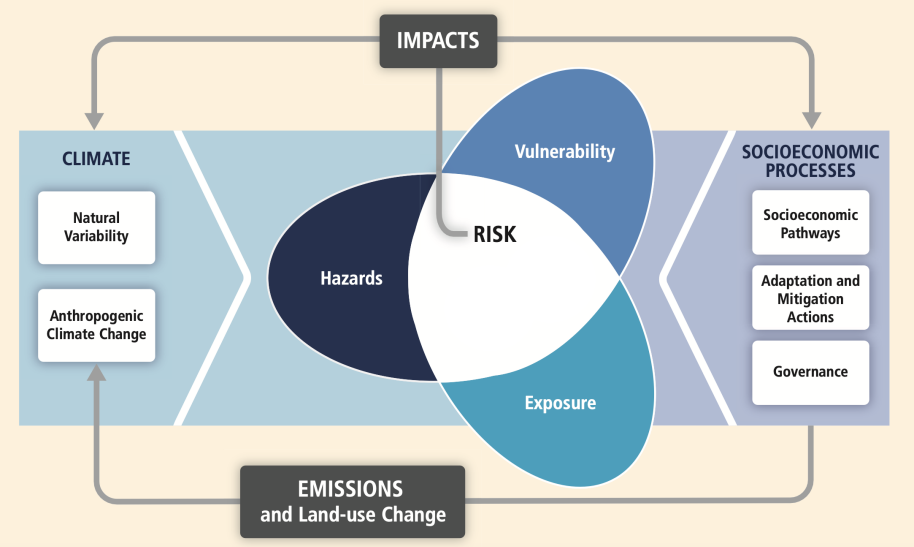

Figure 4: The scheme provided by [7] places on the right side vulnerability and exposure as the result of socioeconomic pathways and societal conditions. On the left side Climate produces natural hazards. Together vulnerability, exposure and hazards produce risk.

lowering the central pressure and strengthening the circulation. Hence the sea surface temperature (SST) play a fundamental role in this terms. Other elements as the atmospheric boundary-layer structure and the large-scale circulation patterns also modulate energy transfer, together with secondary circulations in the inner core (figure 7), eyewall replacement and vortex Rossby waves ([10]).
In figure 6 is shown a diagram of the intensity evolution during the eyewall replacement cycle.

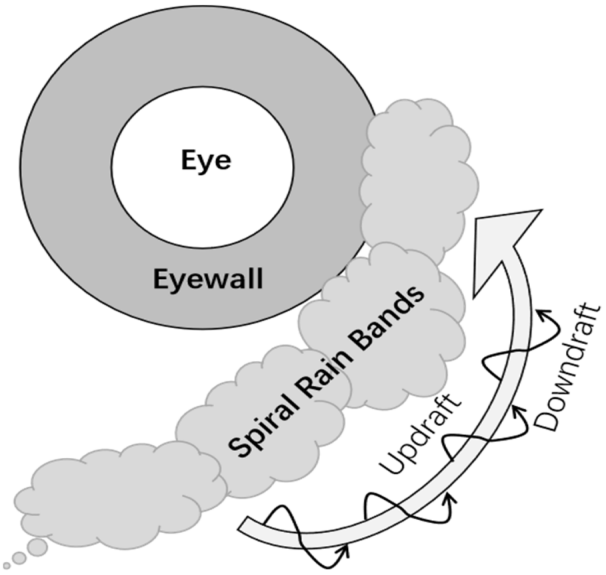

Figure 5: TC structure (from [10]). The gray arrow follows a counterclockwise direction imaging to be in the northern hemisphere. It represents the overall surface level flow. The spiral black lines stands for the small-scale upward and downward motions.

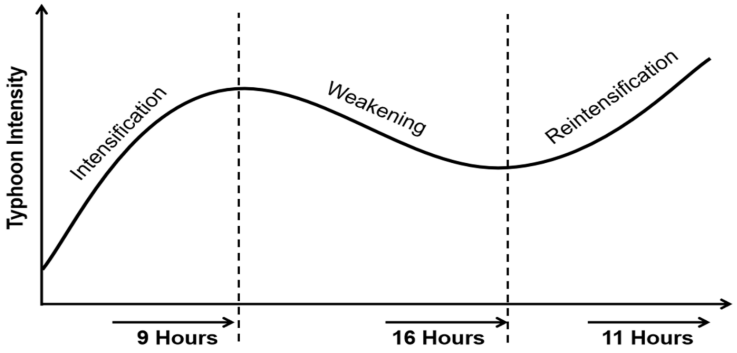

Figure 6: The three phases of an eyewall replacement cycle with the respective average durations (from [10]).

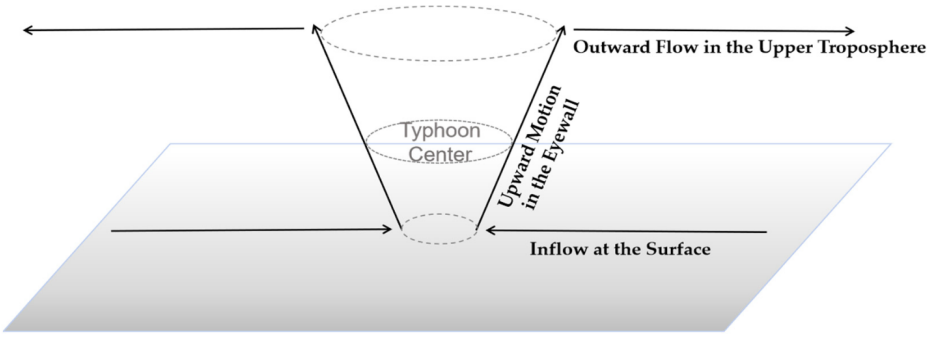

Figure 7: A simplified scheme of the secondary circulation of a TC provided by [10].

The inner core is a crucial area for energetic dynamics where the energy needed to maintain and intensify the system is concentrated. The energy, mainly provided by the sea as latent heat, creates a low pressure centre and is responsible for maintaining convective processes and for the rising temperatures in the mid troposphere, causing a positive feedback cycle. Infact the increase in thermal wind enforces the surface winds and intensifies heat and moisture fluxes. TC intensity is instead strictly related to the eyewall symmetry, but phenomena as wind shear make it asymmetric with the consequent genesis of a second eyewall or external rain bands. If this happens weakening phases occurs followed intensification phases (figure 6). Rapid intensifications need moist air and high SST, as well as the convergence of moisture between low and high levels and the opening of moisture transport channels. On the other hand when the TC meets the land surface its energy decrease. The secondary eyewall genesis plays a key role on the TC intensity. Infact it subtract energy to the primary eyewall causing lower winds and lighter rain, with a reintensification of the process when the two eyewall merges. The timing is crucial because depending on the stage of the TC cycle when it meets the land, the impact can be more or less heavy. The inner core is also the region where most intense precipitations and winds occurs, as well as the brief period oscillations. They are due to the interaction between the rotation of the system and environmental conditions such as vertical wind shear. These processes produce convective asymmetries and eyewall oscillations, distinct from other larger-scale oscillations (such as Rossby waves), and cause rapid variations in TC intensity. Indeed, it should be noted that the tropical cyclone intensity is controlled by environmental parameters besides the internal dynamics. Environmental parameters act on what is considered upper bound on tropical cyclone intensity, or maximum potential intensity (MPI), for given ocean and atmospheric conditions ([11]). According to the MPI theory a tropical cyclone can be treated as a Carnot heat engine in terms of its energy cycle, taking its primary energy from the underlying ocean and working in 4 phases: isothermal expansion, adiabatic expansion, isothermal compression, and adiabatic compression. MPI is reached when the net energy input for mechanical work is balanced by the mechanical energy loss to the underlying ocean. However external environmental variables such as vertical wind shear, dry air entrainment and SST cooling due to air-sea interaction, interacting with the tropical cyclones do not allow most of them to reach their MPI. A typical TC life cycle is represented in figure 8. Guaranteed a required environment with the necessary thermodyamic capacity, a sustained convection develops a surface mesoscale (order of 10-100 km) or synoptic (order of 1000 km) vortex. Then a self-sustaining phase occurs, supplied by both internal and external processes, till the climax is reached, when an intense vortex

is able to extract enormous energy from the ocean. The end of the cycle occurs when it enters a region with cold SST, or strong vertical wind shear, or moves inwards, in other words when it falls into an unfavourable environment ([12]).

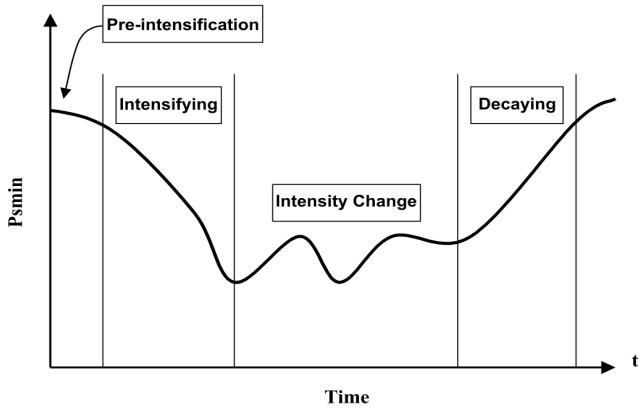

Figure 8: Lifecycle of Tropical Cyclone, from [12].

Instead, concerning internal dynamics, variables as SAI (Storm Activity Index) , ACE (Accumulated Cyclone Energy) , PDI (Power Dissipadion Index) assume particular relevance. As expressed in the equation below SAI depends on V_{max} , on life-time (τ) and number of occurences (N) of cyclones that occur yearly in a specific basin. When $n = 1$ SAI corresponds to the sum of the intensities, while for $n = 2$ and $n = 3$ SAI becomes ACE and PDI respectively.

$$SAI = \sum_{0}^{N} \sum_{0}^{\tau} V_{max}^{n} \tag{1}$$

Regarding their link with climate change recent studies ([13]) exhibit how the increase in the proportion of intense cyclones was consistent with the corresponding changes in the ocean and atmosphere environment during 1980–2015, as also proven by an intensification of North Atlantic tropical cyclones in response to both increased greenhouse gases (GHGs) and aerosol changes during the current century. Globally an average increase in tropical cyclone intensity of 1.3 $\frac{m}{s}$ over the past 30 years was recorded, at the expense of a decrease in their frequency ([11]).
However, due to the interaction with the described physical processes that influence their development and intensification, predicting and understanding the behaviour and characteristics of TCs remains challenging.

Objectives

The objective of this thesis is to analyse climate change according to the SSP5-8.5 scenario, a scenario called “Taking the highway” ([14]) that aims at rapid technological progress and human capital development. However, this includes an exploitation of abundant fossil resources associated with an increase in greenhouse gases and radioactive forcing. The analysis focuses on the evolution and distribution of tropical cyclones, tracked along all longitudes in the tropical belt between 40°S

and 40°N, with particular focus on their frequency, intensity and spatial variability in different basins. Variations of selected climatic variables will be examined, such as surface wind, precipitation, MSLP and temperature at different pressure levels. Finally, differences between periods or scenarios will be analysed to distinguish changes in mean climate and in the frequency and intensity of extreme events associated with cyclones. These differences will be assessed through statistical significance tests in order to identify any robust correlations between climate change and cyclone characteristics. With the purpose of predicting the evolution of TCs at the end of the century, the thesis is divided into 4 additional paragraphs. The next describes and explains the datasets and methods used for their evaluation, while the following two paragraphs describe the present and future climate, with special focus on cyclone behavior. The last section contains conclusions and considerations of the results achieved.

2 Data and methods

In order to study the present and future climate before moving the focus to cyclones, the chosen variables for the evaluation are SST, MSLP, precipitation flux, and surface wind in its components. From the ESGF portal, the available observational datasets of the mentioned variables were then downloaded and exploited to study their seasonal mean and standard deviation over the reference period. Next, a comparison with the reanalysis results will show the reliability of ERA5, and a subsequent comparison with the CMCC climate model used in the following paragraphs will verify its validity. In the following lines there is a list of the datasets used accompained by a brief description of them.

2.1 Observational data sets used

The firsts datasets analyzed regard data obtained through satellite retrieval, all of them avaialble on the Earth System Grid Federation (ESGF) portal and referred to five different variables.
Table 6 describes the dataset that collected the precipitation flux starting from the 1979 with a monthly frequency. The term Obs-GPCP stands for observations from the GPCP (Global Precipitation Climatology Project), which version used is the V2.3. The GPCP was established by the World Climate Research Program (WCRP) in 1986. It consists in combining precipitation informations from different sources, studied and assembled by the Global Precipitation Climatology Centre (GPCC). In this sense geostationary satellites operated by the United States, Europe, and Japan, and secondarily polar-orbiting satellites contribute to infrared precipitation estimates (IR). Microwave estimates are instead obtained from the Defense Meteorological Satellite Program (DMSP, United States) satellites that fly in sun-synchronous low-earth orbits [15]. Compared with the previous version, GPCP V2.3 corrected the cross-calibration of incoming satellite data and updated the gauge analysis. In particular V2.3 uses TIROS Operational Vertical Sounder (TOVS) estimates up to the end of 2002 and Atmospheric Infrared Sounder (AIRS) estimates thereafter, with the cross-calibration achieved through the METH (Microwave Emission Temperature Histograms, [16]) algorithm, whose microwave estimates are exploited as a calibration standard for comparison of the TOVS and AIRS. Adjustments concerning gauge analysis in V2.3 consist in using the GPCC V7 Full analysis ([17]) for 1979–2013 and the GPCC Monitoring analysis V5 for 2014 and beyond ([18]).
The Table 6 specifies also the index node, which tell us where the file can be downloaded, while the institute suggests the data were processed by the NASA Goddard Space Flight Center, a space flight complex founded in 1959 and located in Greenbelt, Maryland. The Obs4MIP project (Observations for Model Intercomparison Projects ,[19]) refers to a collection of datasets that have been organized according to the output requirements of the CMIP5 model. It provides technical documentation for each dataset, including information on uncertainty, dataset merits, and limitations, sharing data through ESGF platforms.
The second dataset analyzed (Table 7) retrieves satellite data with a monthly frequency following the Sea Surface Temperature project of the European Space Agency Climate Change Initiative (ESA-CCI-SST). The results are derived from three series of thermal infrared sensors: the Advanced Very High Resolution Radiometers (AVARRs), the Along-Track Scanning Radiometers (ATSRs), and the Sea and Land Surface Temperature Radiometers (SLSTRs); and two microwave sensors: the Advanced Microwave Scanning Radiometers (AMSR).
In Table 8 and 9 the documentation of the observational data concerning the Northward and East-

ward wind is shown. The datasets produced by NASA-JPL (Jet Propulsion Laboratory) and released on the ESGF portal, make use of the QuickSCAT spacecraft that takes 400000 measurements over 93% of Earth's surface every day. In fact, it circles the Earth every 100 minutes, operating in a near-polar, Sun-synchronized orbit of 800 kilometers. In addition it is equipped with a specilized microwave radar (SeaWinds scatterometer) that is able to measure speed and direction of winds near the ocean surface in all weather conditions.

All the datasets above are results of satellite retrieval, but not all the periods and variables are available for the analysis of interest. For this reason data coming from ERA5 reanalysis are considered as reference observational data for the validity of the model used in the next sections.

ERA5 description

ERA5 is a dataset coming from the fifth generation of atmospheric reanalysis produced by the ECMWF (European Centre for Medium-Range Weather Forecasts), which historical list is shown in figure 9 . Their fundamental role on climate reasearch is is proven by the use of ERA-Interim reanalysis as one input to the WMO (World Meteorological Organization) annual assessment of the State of the Climate and in the assessments carried out by the IPCC.
ERA5 is based on the CY41R2 version of the Integrated Forecast System (IFS), whose data assimilations methodology is based on a hybrid incremental system. The dataset contains two realizations: HRES (High Resolution) and EDA (Ensemble of Data Assimilation, lower resolution). In this thesis only data coming for the former are studied, whose main components of its assimilation system are 4D-Var and LDAS (Land Data Assimilation System). An assimilation diagram is shown in figure 10. The data assimilation system consists in 12-hourly windows going from 09:00 to 21:00 UTC, and from 21:00 to 09:00 UTC the following day, when the observations are used. On each window an analysis field is hourly produced, together with a short forecast from 18:00 and 06:00 UTC, used later as the starting point for the next assimilation. In these forecasts the ERA5 components are coupled, as atmosphere generates ocean waves through the surface wind, waves influence atmosphere with the roughness of the sea surface, and because of the interaction between the atmosphere and land. So, given an assimilation time window let's consider the parameter x as the background forecast valid at the start of the window, and y^o the observations falling within that window. Since the 4D-Var aim is to to find the best estimate of the state of the atmosphere, it corresponds in reducing the value d:

$$d = y^o - y \tag{2}$$

where y are the modelled equivalents of the observations. Note that each parameter refers to a particolar time and all locations. The vector of simulated observations is hence:

$$y = H(x) + b(x, \beta) \tag{3}$$

where x and β, parameters describing biases b in observation space, have to be adjusted in order to obtain the expected result.
In ERA5 the cost function is minimized through a 4D-Var scheme using three different terms which describe the discrepancy with the background, the observations and the model error. In this sense by involving observations and model background in their processes, and guaranteeing space-time consistency, the analysis results may be considered the best estimate of the climate system. As shown in figure the land data assimilations system (LDAS) is weakly coupled with 4D-Var, and its 3 components consists in:

- A 2D optimal interpolation (OI) for 2m temperature, relative humidity and snow;
- A point-wise Simplified Extended Kalman Filter (SEKF) for three soil moisture layers in the top 1m of soil;
- A 1D OI for soil, ice and snow temperature.

Concerning the two OI, they are based on 6 hour sub-windows along the 12 hours assimilation windows of 4D-Var, each only providing an analysis at the central time of its window, while for the soil moisture the analysis products follow the temporal evolution of the SEKF along the 12 hours. The SST and SIC products are stored hourly.

ERA5 dataset is archived in the ECMWF MARS but in order to guarantee fast access to data, a post-processed product is available on the CDS cloud server, where data used in this thesis were taken, after a conversion from the native reduced-Gaussian grid to a regular latitude–longitude grid with a resolution of 0.25°. ERA5 vertical resolution follows a 137 level subdivision, whose top level is 1 Pa, and the covered historical period goes from 1950 to 2024, thanks to a recent extension that goes from 1950 to 1978, which benefits from the assimilation of initial conventional and satellite data. The ERA5 generation until the 1979 has been realized through a suddivision process of 4 parallel fluxes, each with a year overlaid in order to get fluid transition (1950-1959, 1959-1965, 1965-1974, 1974-1979). Concerning the period that goes from 1979 to present, ERA5 use conventional observations coming originally from ERA-40 and later from the ECMWF operational archive through GTS, also including observations from external sources such as ISPD (International Surface Pressure Databank), ICOADS (International Comprehensive Ocean-Atmosphere Data Set), UADB (Upper Air Data Base), CHUAN (Comprehensive Historical Upper-Air Network). The number of observations assimilated in ERA5 are 94.6b billion in 4D-Var, 65 million in the OI ocean-wavecomponent and about one billion each of surface air temperature and relative humidity by the LDAS, improving the number per day from 1979 to 2019. ERA5 uses measurements from many satellite platforms (a brief list of some of them is shown in Table 1), considering that only the 4D-Var component uses observations from over 200 satellite instruments or types of conventional data. The latters can be classified in 5 different groups: SYNOP, measurements made near the surface at land stations, DRIBU, made by drifting and moored buoys, TEMP, radiosondes and dropsondes, PILOT, balloon observations and wind profilers, and AIRCRAFT-based atmospheric observations.

In particular ERA5 gets informations from PILOT, radiosonde, dropsonde and aircraft measurements concerning upper-air obserservatonso of wind, temperature and humidity, while for 10m wind over sea, 2m humidity over land, and pressure over land and sea, it benefits of the 'in situ' observations (SYNOP). Similarly, LDAS extract informations form 'in situ' observations of the global SYNOP network for temperature and humidity at screen level, soil moisture and snow depth. Upper-air temperature and humidity data come also from GNSS-RO bending angles.

GMS(-1,-3,-4,-5)	ASCAT (MetOp-A,-B)	GOME(ERS-2)
MTSAT-1R	CrIS (S-NPP/NOAA-20)	MIPAS(ENVISAT)
GOES-9	DMSPSSMI(F-08to-15)	OMI(EOS-AURA) BUV(Nimbus-4)
AVHRR(NOAA-7to-18)	IASI (Metop-A,-B)	AltiKaonSARAL
SCHIAMACHY(ENVISAT)	AMIonERS-1,-2	RAonERS-1,-2

Table 1: Some of the satellite instruments used by ERA5

Reanalysis	**Period covered**	**Grid resolution**	**Assimilation scheme**	**IFS model cycle (year)**
Atmospheric reanalyses				
FGGE	1979	208 km	OI	(1980)
ERA-15	1979–1994	125 km	OI	13r4 (1995)
ERA-40	1957–2002	125 km	3D-Var	23r4 (2001)
ERA-Interim	1979–2019	80 km	4D-Var	31r2 (2006)
ERA5	1950–present	31 km	4D-Var	41r2 (2016)

Figure 9: ECMWF atmospheric reanalyses list, from [20].

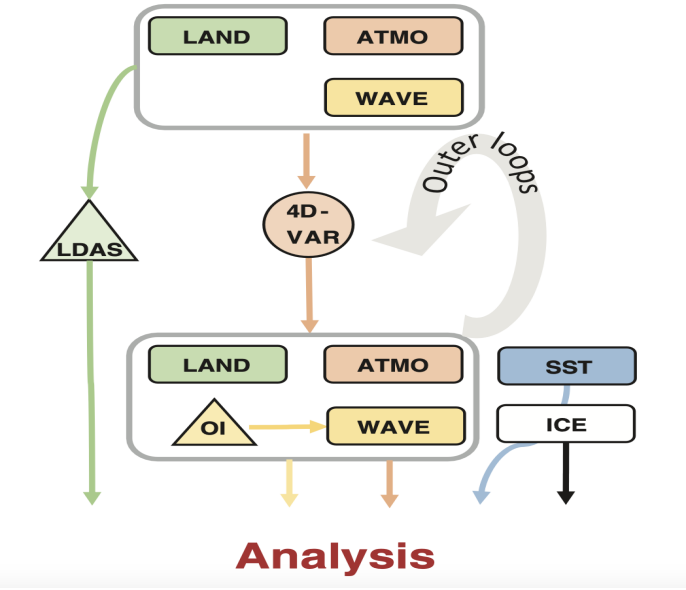

Figure 10: Assimilation diagram for ERA5 ([20]). **ATMO**=atmosphere, **LAND**=surface temperature, **WAVE**=ocean waves, **SST**=sea surface temperature, **ICE**=sea ice. Large boxes stand for outer loop integrations and contain coupled components. Circle indicate 4D-Var inner loops, and triangles refer to land-data assimilation (LDAS) and ocean wave optimal interpolation (OI). 4D-Var minimizes a linearized quadratic cost function at reduced resolution in inner loops, with non-linear updates at full resolution in outer loops (trajectories).

2.2 Climate models

Concerning the analysis of future scenarios presented in AR6, it refers to the the sixth phase of the CMIP. As a project of the World Climate Research Programme (WCRP), CMIP objective is providing climate projections to understand past, present and future climate changes, through a comparison of climate models.
A climate model is a complex computer program that use mathematical formulas to re-create the chemical and physical processes that drive Earth's climate, analyzing processes and interactions between parts of Earth's climate system: the atmosphere, ocean, land surface, cryosphere and biosphere. Clearly simplifications on climate system characterize every model, each in a different way. In this sense comparing models to real world observations and simulations from different models is useful for understanding which results are consistent across models, and which results are not in agreement.
Global climate models (GCMs) couple an atmospheric model, or atmospheric general circulation model (AGCM), with an ocean model (Ocean General Circulation Model, OGCM), so they are often referred to as atmosphere-ocean general circulation models (AOGCMs).
An AOGCM is composed by seven basic mathematical equations and seven basic variables that describe atmospheric motion and processes. The set of equations, sequentially solved across the grid space for each time step, respect the 4 principles ([21]):

- conservation of mass

- conservation of energy
- conservation of momentum
- elemental kinetic theory of gases

AGCM simulate the circulation of the atmosphere and the atmospheric flow, with its exchange and energy transport processes. It uses equations that link the mass distribution and the wind field, through a spherically spatial grid field that has many levels related to the depth of the atmosphere. But not all the processes occur on a grid scale, as turbulence and latent heat of condensation in cloud formation, that arise on a scale below, leading to a modification of flow equations for their representation.
OGCM plays a fundamental role as dynamic thermal reservoir that, through energy exchange with the atmosphere, contributes to the transport of energy. In this sense processes that regulate heat, moisture, and momentum exchanges between the ocean and atmosphere are crucial. Other two important factors are given by the land surface and surface ice sheet with their energy processes (e.g. extension or contraction of ice sheets represent respectively a lowering or increase in total energy of the climate system).
In order to study the climate system and its evolution, radiation processes that regulate the input and output of energy, where GHGs play a fundamemental role as said before, has to be involved. During the cycle of season infact, Earth alternately warms and cools, when respectively the infrared radiation loss to space increases such that it exceeds the solar input and warming ceases, and the infrared radiation loss to space decreases such that solar radiation exceeds the infrared radiation loss and cooling ceases.
It's important to highlight that just because laws of physics are used does not mean a process is predictable. Infact, as anticipated before, within the AOGCM there are many processes that operate on scales below the resolution of the computational grid (called sub-grid scale processes) and regulate local temperature, moisture and momentum. For example clouds and their interaction with the climate system are difficult to model, as the convection or atmospheric processes such as thunderstorms, with their energy exchange processes.
There are also physical processes for which there is no precise formulation, and then parametrizations are used. There could be unavailable data to set initial conditions or measurement error and uncertainty associated with the initial conditions at the beginning of the forecast period, which propagate and amplify in the system. Therefore, any atmospheric or climate model is an object that represents our best estimate of how the atmosphere or climate works. It is the best approximation of the main processes of the represented system and the mechanisms that link them.

However, it remains an international priority to improve knowledge about the climate system in order to find solutions for adaptation and mitigation actions. In this sense, starting by running 18 GCMs in its first two phases, the 6th phase of CMIP (CMIP6) involve more models and more experiments than its predecessors, thanks to the partecipation of more than 50 modeling centers around the world, including CMCC. In particular, CMIP6 structure consists in three main parts. First, the identification of DECK (Diagnostic, Evaluation and Characterization of Klima) experiments and CMIP simulations in order to evaluate and describe the characteristics of climate models. Second, common standards, coordination, infrastructure, and documentation that facilitate the distribution of model outputs and the characterization of the model ensemble, and finally a more federated structure, by preferring more autonomous CMIP-Endorsed MIPs ([22]). Considering the huge amount

of data, CMIP6, as its previous version, relies on the Earth System Grid Federation (ESGF) portal, that provides secure, web-based, distributed access to climate model data.
As already highlighted, Climate Model Intercomparison Projects (CMIP) simulations are essentials for IPCC ARs, and in this thesis CMCC-CM3 simulations, for their contributions on CMIP6, are used for the main objective of the work. As anticipated it consist in studying the present and future climate focusing on the behavior of the tropical cyclones over the last 30 years and predict it at the end of the century, highlighting their important contribution over the mean climate. Several variables (as precipitation flux, sea surface temperature and superficial wind) at global level are analyzed in the former chapter, during a period going from 1950 to the present day (based on the available period for datasets coming from satellite observation). They are later used for the comparison with results coming from reanalysis data (ERA5), and then with dataset obtained from the model CMCC-CM3, concerning the period 1975-2014. Once proved the reliability of the latter simulations and the model used, it will be possible compare them with the same variables used for the simulation of the mean climate over the 2070-2100, moving then the focus over the tropical cyclones statistics and their evolution over time.

2.3 The climate model. Description of the systems and the simulations

The model used in this thesis for the next sections is a general circulation coupled model developed by the CMCC, named CMCC-CM3-LT (Table 10). It is composed by several components, synchronized through a coupler.

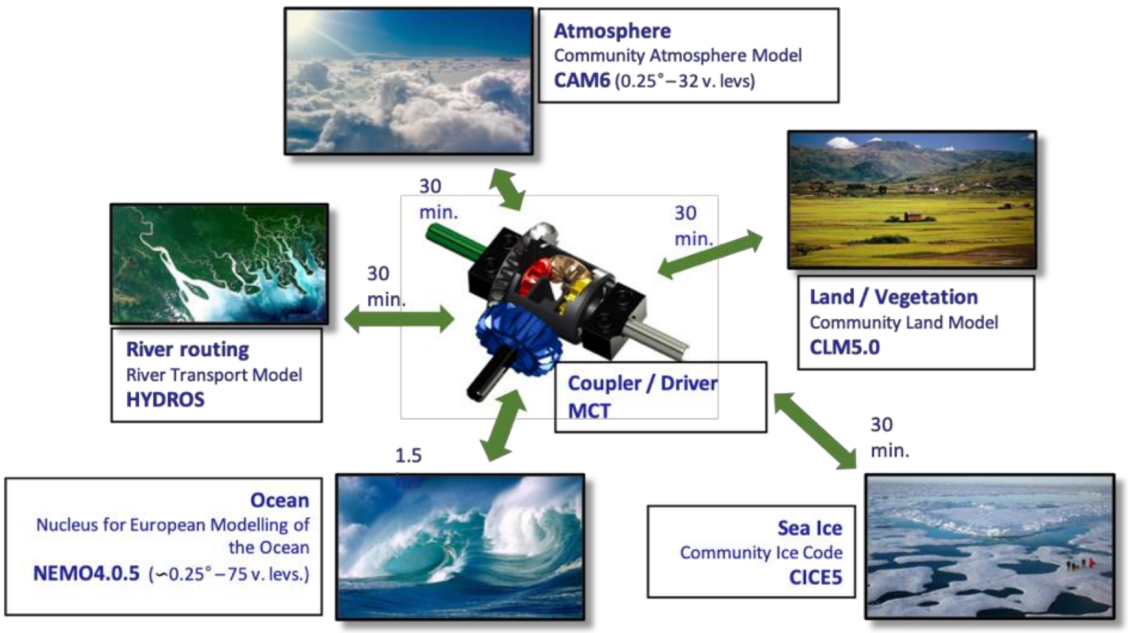

Figure 11: Scheme of CMCC-CM3 coupled model components, provided by [23]

CMCC-CM3-LT simulations follow CMIP6 standards regarding the forcings and initial conditions used in the initialization of climate simulations, and its third version (CM3) present several improvements with respect to the previous version (CMCC-CM2), as increased number of vertical levels and horizontal resolution (25 km), both for atmosphere and oceans. For the purposes of this thesis two simulation family are employed. The historical simulations (1975-2014), that starts by exploiting a restart file created through a spin-up run for several decades, and future simulations (2070-2100) forced by the SSP5-8.5 emission scenario ([23]). Next lines contain a brief description of the CMCC-CM3-LT structure and the latests versions of its components.

2.3.1 CMCC-CM3

The CMCC-CM3-LT structure is composed by 5 dynamical models that share informations through a coupler. They are coupled with 30 min frequency, except for the oceanic component whose exchange processes occur every hour and a half. They are the Community Atmosphere Model (CAM), the oceanuc engine Nucleus for European Modelling of the Ocean (NEMO), the sea ice model Community Ice CodE (CICE), the Community Land Model (CLM) and river transport model HYDROS. In the following paragraphs a brief desscription of the firsts 4 components.

CAM

As product of the National Center for Atmospheric Research (NCAR), CAM corresponds to the atmospheric component of CMCC-CM3-LT, where it is used in its sixth version (CAM6). The following lines analyse the updates for its latest CAM5 and CAM6 versions ([24], [25]).

- A moist turbolence scheme

  It analyzes stratus-radiation-turbolence interactions in order to simulate full aerosol indirect effects within stratus, operating in any layer where the Richardson number (Ri) is larger than 0.19.

  $$Ri = \frac{buoyancy\_term}{flow\_shear\_term} = \frac{g}{\rho}\frac{\partial\rho/\partial z}{(\partial u/\partial z)^2}$$

  where u is the flow speed, ρ stands for density and z represents the vertical depth. The main role of the scheme is to vertically transport heat, moistures, horizontal momentum and tracers by symmetric turbulences. It's based on a diagnostic Turbolent Kinetic Energy formulation (TKE), and uses a first order k-diffusion scheme [26].

- A shallow convection scheme ([26])

  Its role is to transport heat, moisture, horizontal momentum and tracers vertically through asymmetric turbulence, and is performed by CAM5 right after the deep convection scheme. Differences with the latter refer to cloud top height, existence of convective precipitation and convective downdraft. It is structured in 8 main processes: reconstruction of mean profiles and cloud condensate partitioning, computation of source air properties of a single ensemble-mean updraft plume at the PBL (Planetary Boundary Layer) top, cloud base mass flux and updraft vertical velocity closures, vertical evolution of a single entraining-detraining buoyancy, penetrative entrainment in the overshooting zone near cumulus top, computation of convective fluxes, computation of grid-mean tendencies of conservative and non conservative scalars.

- New methods for stratiform microphysical processes ([27])

  It is based on a prognostic, two-moment formulation for cloud droplet and cloud ice. Liquid and ice particle size comes from gamma functions, whose evolution in time is subject to grid-scale advection, convective detrainment, turbolent diffusion and other microphysical processes. Cloud droplets formation occurs on a multi-modal lognormal aerosol size distribution based on the scheme of ([28]) dependent on aerosol chemistry, temperature and vertical velocity. The cloud microphysics scheme used in CAM5 was later replaced by an updated version in CAM6 ([29]).

- An updated radiation scheme ([30])

  It exploits a modified correlated k-method for calculating radiatve fluxes and heating rates in the clear sky and for condensed phase species

- The inclusion of the unified turbulence scheme Cloud Layers Unified By Binormals in CAM6, proposed in ([31]).

CAM separates the parametrization suite from the dynamical core, that can be coupled together in a time split way. Hence the general prediction equation for a generic variable ψ is:

$$\frac{\partial \psi}{\partial t} = D(\psi) + P(\psi) \tag{4}$$

where D corresponds to the dynamical core and P is the parametrization suite. The parametrization package is composed by a sequence of components indicated as $P = \{M, R, S, T\}$, representing respectively moist precipitation processes (M), cloud and radiation parametrizations (R), surface processes (S), and turbolent mixing (T). Instead, the dynamic core used is of the finite-volume (FV) type, whose horizontal discretization is based on a conservative "flux-form semi- Lagrangian" scheme described by [32], while the vertical discretization is a quasi-Lagrangian. The horizontal resolution is about 1°, on a regular grid of $0.9° \times 1.25°$, while the vertical resolution is composed by 32 vertical levels and a model top at 2.26 hPa (about 40 km). CAM receives from the coupler informations about: surface albedo, land, ice and ocean fractions, sea surface temperature, surface wind stresses, sensible and latent heat fluxes, upward longwave radiation, evaporation, and dust emissions. Quantities sent to the coupler are instead: zonal and meridional velocities, atmospheric temperature, humidity and precipitation, downward shortwave and longwave radiation.

NEMO

The ocean component of the model is based on the general model of ocean circulation NEMO ([33]), composed by three related engines: OPA (Océan Parallélisé) TOP, (Tracer in the Ocean Paradigm) and LIM (Louvain Ice Model).
NEMO is able to solve the primitive equations, Navier Stokes along with a nonlinear equation of state, which couples temperature and salinity with the fluid velocity, under the conditions of the following assumptions: spherical earth approximation, thin-shell approximation, turbolent closure hypotesis, hydrostatic hypotesis, Boussinesq hypotesis and incompressibility hypotesis. Prognostic variables used in NEMO are the three components of velocity, the sea surface height, the potential seawater temperature, and salinity.
Concerning the time domain, the time stepping used in NEMO can be expressed as:

$$x^{t+\Delta t} = x^{t-\Delta t} + 2\Delta t RHS_x^{t-\Delta t, t, t+\Delta t} \tag{5}$$

where x is one of the prognostic variables Δt is the time step and RHS stands for the right hand side of the corresponding time evolution equation. Two different methods are used for diffusive and non diffusive processes. In the first case the RHS is replaced with the term D_x with $t - \Delta t$ as exponent. Instead for non diffusive processes a time centered scheme, hence evaluated at time step t, is used, named leapfrog scheme. Since a divergence of odd and even time steps may occur, in order to avoid it the Robert Asselin time filter is exploited. The equation takes the following form:

$$x_F^t = x^t + \gamma[x_F^{t-\Delta t} - 2x^t + x^{t+\Delta t}] \tag{6}$$

where F denotes filtered values and γ is the Asselin coefficient. The grid in NEMO is ORCA, a tripolar grid developed according to the semi-analytical method proposed by [34]. The orthogonal curvilinear oceanic mesh that is generated has no points of singularity within the computational domain. The method is based on defining an analytical set of parallels in the stereographic polar plane, from which the corresponding set of meridians is derived. The resulting grid is finally projected onto the spherical surface. Horizontal resolution can be approximated to 0.25° while vertically the model is divided into 75 geopotential levels.

- Total Variance Dissipation scheme (TVD) In this formulation the tracer at velocity points is evaluated using a combination of an upstream and a centred scheme, where the advective part is time stepped with a leap-frog scheme and the diffusive part follow a forward scheme
- Turbolent Closure Scheme (TKE closure, [35]) It is used in order to compute the vertical eddy viscosity and the diffusivity coefficients, exploiting a prognostic equation for the turbulent kinetic energy ($\hbar e$), and a closure assumption for the turbulent length scales. The time evolution of $\hbar e$ is the result of its production through vertical shear, its destruction through stratification, its vertical diffusion, and its dissipation.

The interfaces involved in the model are 4, each treated differently with respect to the others. The land-ocean interface contributes to the changing in sea surface salinity through a mass exchange of fresh water through river runoff occurring as major flux, while regarding solid earth-ocean interface the heat and salt fluxes are usually neglected, unlike momentum exchanges happen through frictional processes. For the atmosphere-ocean interface an important role plays horizontal momentum (wind stress), and heat exchanges, together with the fresh water PE (the precipitation minus evaporation budget). The ocean and sea ice instead exchange heat, salt, fresh water and momentum. Salt and fresh water are important for their role in the cycle of freezing and melting. The ocean model gets from the other components of the CMCC-CM3-LT, after the coupler processes, fluxes of momentum, heat, and freshwater at the air-sea interface as surface boundary conditions.

CICE

CICE in its fifth version (CICE5) is used by the CMCC-CM3-LT as sea ice component, ([36], [37]). It is employed in order to study thermodynamics for vertical fluxes, ice dynamics and transport. For the sea ice transport CICE solves the fundamental equation:

$$\frac{\partial g}{\partial t} = -\nabla \cdot (gu) - \frac{\partial}{\partial h}(fg) + \Psi \tag{7}$$

in which the three terms of the r.h.s describe 3 kinds of transports: horizontal transport, transport in thickness space dued to thermodynamic growth and melting, and transport in thickness dued

mechanical processes, like ridging and rafting. The terms used in the equation above stands for horizontal ice velocity (u), thermodynamic ice growth rate (f), ridging redistribution function (Ψ) and the ice thickness distribution function (g). The method used to solve it consists in splitting the ice pack into 5 thickness categories, and for each of them defining the following state variables: ice and snow volume, the internal ice and snow energy in the layer, the surface temperature and the volume weighted mean ice age. In the horizontal transport the continuity equation below is solved.

$$\frac{\partial a_{in}}{\partial t} = -\nabla \cdot (a_{in} u) \tag{8}$$

where a_{in} is the fractional ice area in the n-thickness category that can be replaced by other variables as ice or snow volume, and ice or snow energy. For tracers transport the equation becomes:

$$\frac{\partial a_{in} T_n}{\partial t} = -\nabla \cdot (a_{in} T_n u) \tag{9}$$

If interested in ice transport in thickness space the equation assumes the form:

$$\frac{\partial g}{\partial t} = -\frac{\partial}{\partial h}(fg) \tag{10}$$

in which the thickness distribution function g can be approximated to a linear function of h in each category. The five categories are treated as Lagrangian grid cells with boundaries projected forward in time. The last kind of transport involves mechanical redistribution. Its scheme is adopted to convert thinner ice to thicker ice, after the horizontal transport, and the thickness distribution depends on the weighting function $b(h)$, that favors ridging of thin ice and closing of open water rather than ridging of thicker ice. In the following equation $G(h)$ stands for the fractional area covered by ice thinner than h, while G^* is an empiric constant.

$$b(h) = \begin{cases} \frac{2}{G^*}\left(1 - \frac{G(h)}{G^*}\right) & if \quad G(h) < G^* \\ 0 & otherwise \end{cases}$$

For ice dynamics it's employed the Elastic-Viscous-Plastic model (EVP). It consists in a modification of the VP model for ice dynamics [38]. In CICE5 it was updated by the revised EVP method, while for the observed sub-continuum anisotropy of the sea ice cover viene usato the Elastic-Anisotropic-Plastic (EAP) model ([37]). As regards thermodynamics for vertical fluxes the model computes changes in ice and snow thickness for each category, and vertical temperature profile resulting from radiative, turbolent and conductive heat fluxes. Additionally ice has a specific-heat dependent on temperature to simulate the effect of brine pocket melting and freezing. CICE use the same horizontal grid of the oceanic component and the time step is of 30 minutes. It is linked with the other components of CMCC-CM3-LT through the coupler concerning the properties of the surface sea and near-surface air (temperature, salinity, humidity and heat fluxes). Among the updates added with CICE5 there are a method for prognosing sea ice salinity, including improved snow-ice formation, two new explicit melt pond parameterizations (topo and level-ice ponds) and the addition of ice and snow enthalpy as tracers ([37]).

CLM

The CLM is used in CMCC-CM3-LT in its version 5.0, As a terrestrial component, its purpose is to study physical, chemical, and biological processes through which terrestrial ecosystems affect (and

are affected by) climate. In the following lines can be seen which updates characterised the two latest versions, CLM4.5 and CLM5 ([39], [40]). Their implementations result in the reduction of biases in simulations like low soil carbon stocks, dry soil bias in Artic soils, transient 20^{TH} century carbon responces inconsistent with observational results and other inconsistency. Among the updates of CLM4.5 there are revisions of canopy radiation scheme, revisions to photosynthetic parameters, introduction of an ice impedence function and a new more realistic lake model [41]. Moreover a new scheme of soil biogeochemistry is implemented, with with base decomposition rates modified by soil temperature, water, and oxygen limitations. It includes also vertical mixing of soil carbon and nitrogen due to bioturbation, cryoturbation, and diffusion [42]. A methane production, oxidation, and emissions model is implemented while the crop model is extended to guarantee a good representation of interactive fertilization, organ pools [43], and irrigation [44]. As regards Earth surface-atmosphere interaction the carbon (C) and nitrogen (N) cycles of soil and vegetation that are analyzed follow the CENTURY model [45]. In the model, however, vegetation functional types (PFTs) can not change in response to climate change. The CLM is then initialized separately from the other components, using the results of a long offline spinup simulation until the equilibrium for the soil pools is reached. Then CLM4.5 is coupled with the River Transport Model (RTM), for transport from the earth's surface to the ocean. In particular it linearly transports water from a cell to its downstream neighboring cell whose velocity depends on the grid cell mean topographic slope. While RTM operates with a regular resolution of 0.5° and a time step of 3 hours, CAM4.5 uses the same horizontal grid as the atmospheric component and a 30 min time step. However, in the model used by the CMCC-CM3-LT, CLM5.0, further updates were made regarding parameterizations and structure for hydrology and snow, plant hydraulics and hydraulic redistribution, nitrogen cycling, global crop model, urban building energy, carbon isotopes, and stomatal physiology.

2.4 CyTRACK framework

Underlined the relevance of the cyclones occurence on the impacts on climate and people's life and the functionality of climate models, this paragraphs describes the CyTRACK algorithm (Cyclone TRACKing framework), tracker used in this work ([46]). CyTRACK is an open-source and user-friendly python toolbox for tracking cyclones. It detects their centres and trajectories in certain data sets, as well as frequency, duration and spatial distribution. The detection method consists of two parts, searching critical centers and pairing them across time steps.
Critical centres are detected as minimums of MSLP under a set of conditions and/or minimum or maximum thresholds that can be modified by the user ([46]).
In this sense in the following lines are listed the necessary boundary variables for the tracking process with an explanation of them. The specific parameter values adopted in this study are detailed in the paragraph 3.3.

- *core_criteria_length*: number of consecutive time steps a system must satisfy the criteria.
- *max_wind_speed_threshold*: minimum wind speed (in m/s) required to consider a low-pressure grid point as a tropical cyclone (TC) center.
- *outer_wind_speed_threshold*: outer wind speed threshold (in m/s) used to compute the TC outer radius.
- *filter_center_threshold*: minimum distance (in km) between two critical centers.

- *dist_threshold*: maximum distance (in km) allowed between centers at consecutive time steps.
- *critical_outer_radius*: critical outer radius (in km) to consider a low-pressure point as a TC center.
- *dr_res*: radial resolution (in km) for radial leg analysis.
- *d_ang*: angular resolution (in degrees) for radial leg analysis.
- *rout*: external search radius (in km).
- *terrain_filter*: elevation threshold (in m) to exclude terrain-affected grid points.
- *intensity_threshold*: maximum wind speed threshold (in m/s) for the system along its trajectory.
- *dt_lifetime*: minimum lifetime (in hours) for a candidate system to be retained.
- *vorticity_threshold*: relative vorticity threshold (in 1/s) to filter TC centers.
- *min_slp_threshold*: maximum sea level pressure (in hPa) to consider a grid point as a TC center.
- *minimum_distance_travelled*: minimum distance (in km) a system must travel to be considered valid.
- *great_circle_distance*: radial distance (in degrees) over which the MSLP increase is evaluated.
- *dmslp_great_circle_distance*: required increase in MSLP (in Pa) over the great-circle distance to confirm the pressure minimum.
- *radius_for_msw*: radius (in km) used to compute the maximum surface wind around a candidate center.
- *mslp_anomaly_threshold*: MSLP anomaly threshold (in hPa) to identify candidate cyclone centers.

Then, in order to assess the cyclone trajectory, if two storms centres occur within a time step dt from t_0 and a critical distance from the centre in t_0 CyTRACK links them together, thus moving to the next step. When the trajectory is interrupted then the lifetime, the minimum distance travelled and the max velocity along the path are calculated.
CyTRACK also makes it possible to determine the radius of the cyclone (by finding the outermost closed isobar) via the MSLP, using the method described in [47]. After mapping in a polar coordinate system centred in the cyclone and analysing the MSLP along each radius, critical values are identified. These are then compared to find the minimum value corresponding to the pressure of the outermost closed isobar. Through the wind speed, the tracker is able to determine the size of the cyclone by calculating the radial distance from the centre when the 10-m azimuthal wind reaches a certain critical threshold. CyTRACK first determines an approximate size for each radial leg and then averages it to find the size of the cyclone.
Finally, although this ability is not exploited in this document, CyTRACK can be used to classify cyclones by the thermal structure at each point of the path, using the cyclone phase space (CPS) proposed in [48]. It is based on the use of three parameters related to cyclone thermal symmetry and the cold or warm core of the cyclone.

2.5 Methods: description of the statistics used to evaluate the model performances and the traking algorithm

Data coming from datasets commented so far are used in the next chapter in order to evaluate the model reliability, through several comparisons between observationl data and ERA5 results, and between ERA5 and simulations results.
But, before starting the comparison it is useful to define the metrics used in this thesis:

1. MB : *Mean Bias error*
   It measures the difference between the mean of the simulated data and the mean of the observed data:
   $$MB = \bar{m} - \bar{o}$$

2. SDE : *Standard Deviation Error*
   It is the difference between the standard deviation of the simulated data and the standard deviation of the observed data, and its formula is:
   $$SDE = \sigma_m - \sigma_o$$

3. CC : *Cross Correlation*
   The Cross Correlation measures the correlation between two datasets giving as result a value ranging from -1 to 1:
   $$CC = \frac{1}{\sigma_o}\frac{1}{\sigma_m}\frac{1}{N}\sum(m_i - \bar{m})(o_i - \bar{o})$$

4. $uRMSE$: *unbiased Root Mean Square Error*
   It corresponds to the quadratic mean of the product of differences between the observed and simulated data and their mean value:
   $$uRMSE = \sqrt{\frac{1}{N}\sum[(m_i - \bar{m})(o_i - \bar{o})]^2}$$

3 Results: Present climate (1975-2014)

3.1 Evaluations of the mean climate

This paragraph contains an analysis of the results coming from the observational datasets listed and described before, concerning the variables of interest already mentioned. However, the observational datasets presented exhibit some limitations. In fact, the time periods covered by the different datasets are not the same, and the MSLP data cannot be collected. Therefore, in the case of the MSLP variable, ERA5 will be used directly as a reference.
For each dataset 8 graphs divided by season are produced, 4 inherent to the average climate and 4 to the standard deviation along the period of interest. For semplicity each season is indicated by 3 letters corresponding to 3 months: MAM (March, April, May), JJA (June, July, August), SON (September, October, November) and DJF (December, January and February).

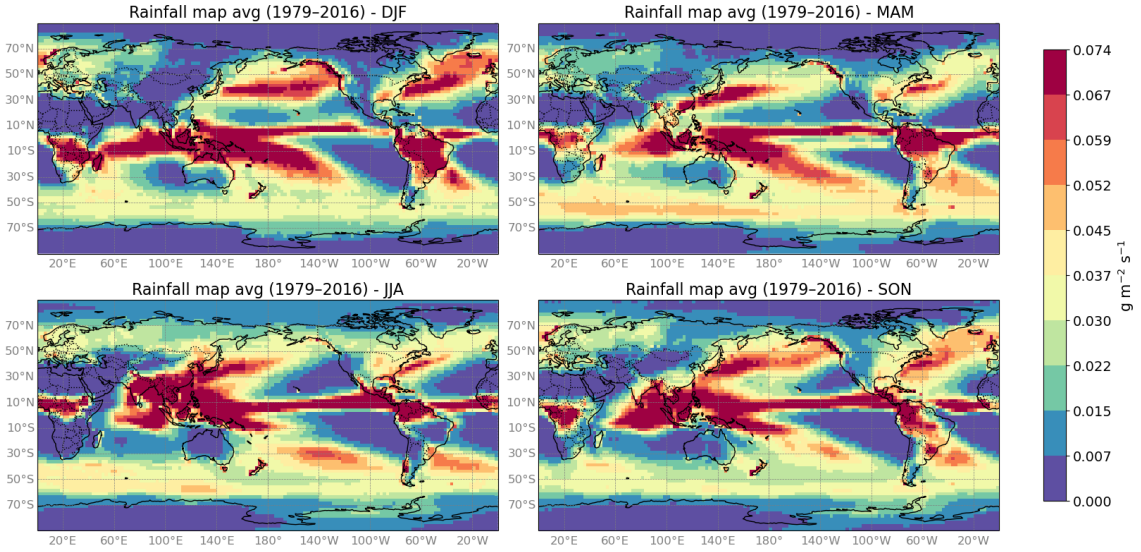

Figure 12: Mean precipitation flux divided by seasons obtained from the dataset of Table 6

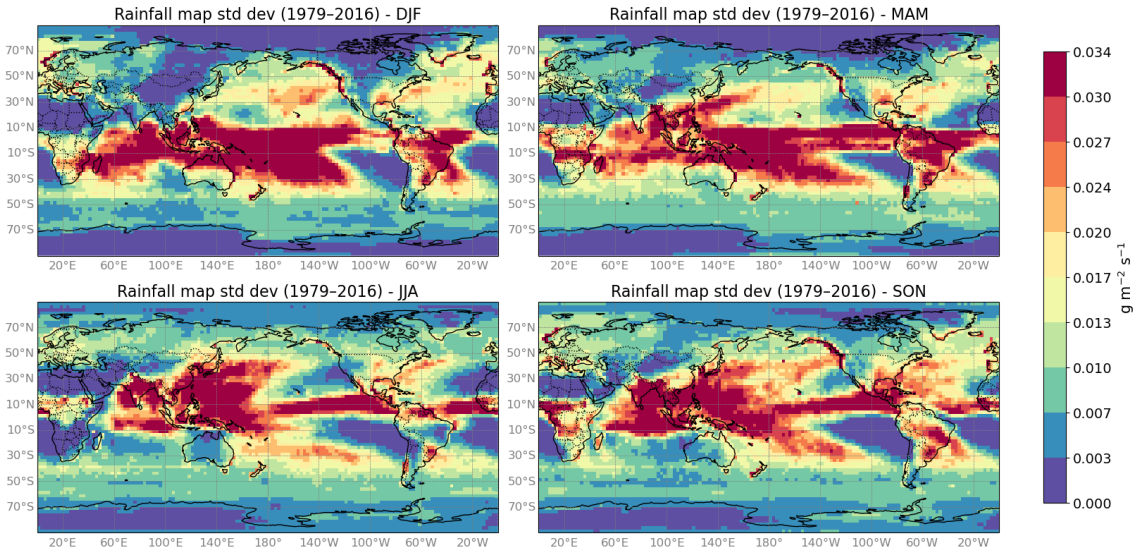

Figure 13: Precipitation flux std dev divided by seasons obtained from the dataset of Table 6

The first figures regard the precipitation flux expressed in $\frac{g}{m^2 s}$ during the period from 1979 to 2016. The most affected regions to high precipitation rates are in the equatorial area, as proven by islands in the Indian Ocean, some areas in central Africa, and Latin America. As expected, on the other hand, the least affected areas with values close to 0 are North Africa, especially in DJF, and South Africa in the JJA months. In fact the major seasonal differences can be noted between DJF and JJA. In JJA the precipitation rate is higher then in DJF closed to the equatorial line and in the soth of Asia, while it is lower in the north of Australia, in Brazil, in the south of Africa and in other points in South America far from the equator. The Pacific Ocean presents a similar pattern in all the seasons with the Western Pacific subject to heavy precipitaions and the eastern side with rare occurrences of rainfall, except along the equatorial line. The second set of images shows that areas where the seasonal mean precipitation is high, so is the variability, approaching values of 0.07 $\frac{g}{m^2 s}$ in some points, while in areas where the seasonal mean is approximately zero even the standard deviation is low, signifying how most of the time there is no precipitation. In correlation to the differences in mean precipitation, the variability measured in JJA in the less rainy areas mentioned above is lower than that observed in the same areas but in DJF. Different seasonal variability is also found in the west coast of North America, whose standard deviation decreases from DJF to JJA, and in the middle of the Pacific Ocean, which is subject to less variation in JJA than in the other months of the year.

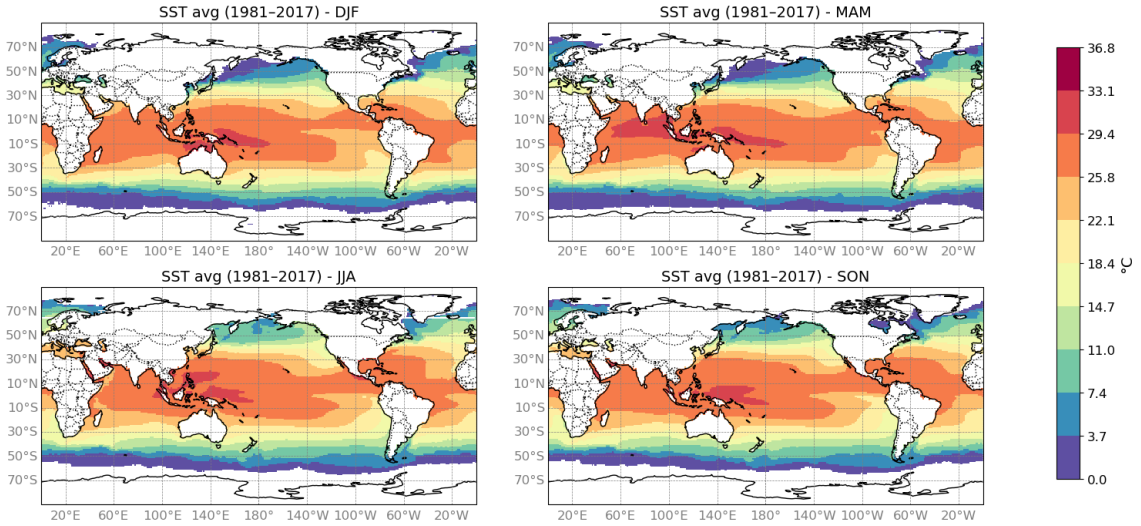

Figure 14: Mean sea surface temperature divided by seasons obtained from the dataset of Table 7

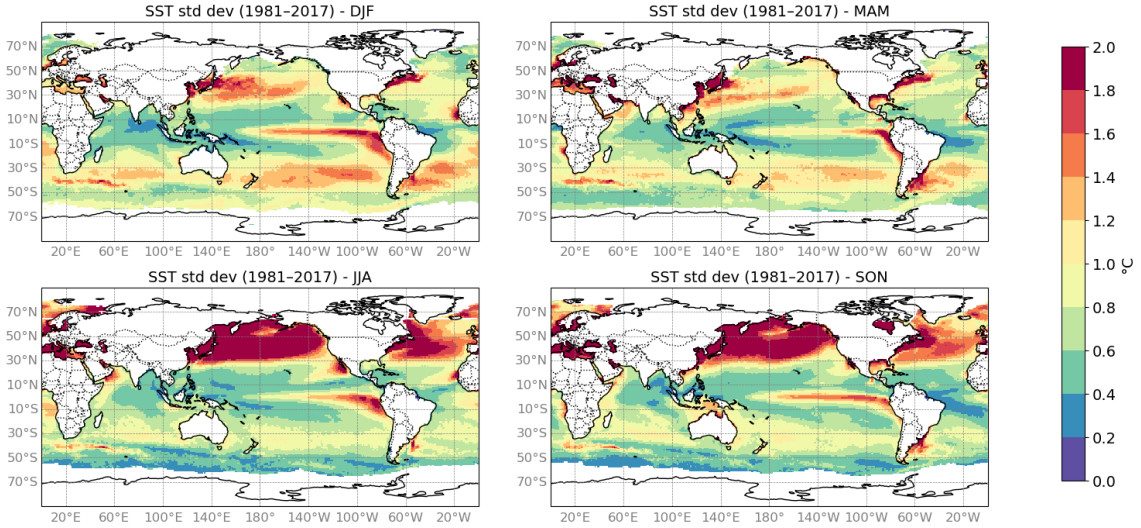

Figure 15: Sea surface temperature std dev divided by seasons obtained from the dataset of Table 7

Results shown in figure 14 and 15 refers to the average and standard deviation of the SST between the years 1981 and 2017. Maximum values are recorded in the tropical belt with decreasing temperature approaching South America from the Pacific Ocean and the west coast of the south part of Africa in the SOuth Atlantic Ocean in each season. An other evidence is the decrease of SST moving toward the poles. Regarding the mean values there are no significant differences between the season, but this is not true for the SST variability. In fact while in MAM and DJF the standard

deviation is quite heterogeneous around the globe, in JJA and SON the unmasked area between 30°N and 60°N is characterized by a SST standard deviation around 2°C, so much more than the rest of the chart.

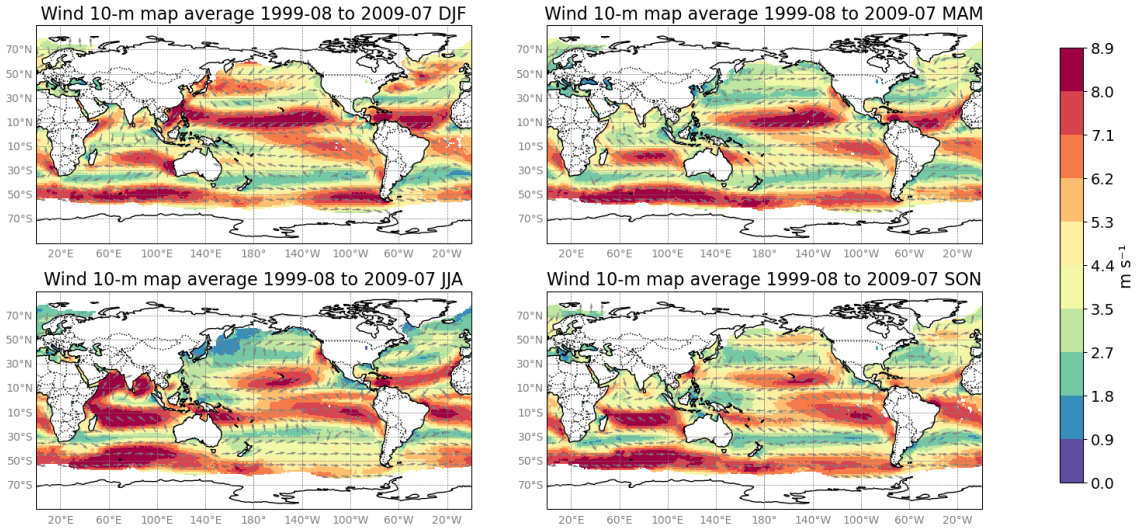

Figure 16: Mean wind speed and direction divided by seasons obtained from the dataset of Table 9 and 8

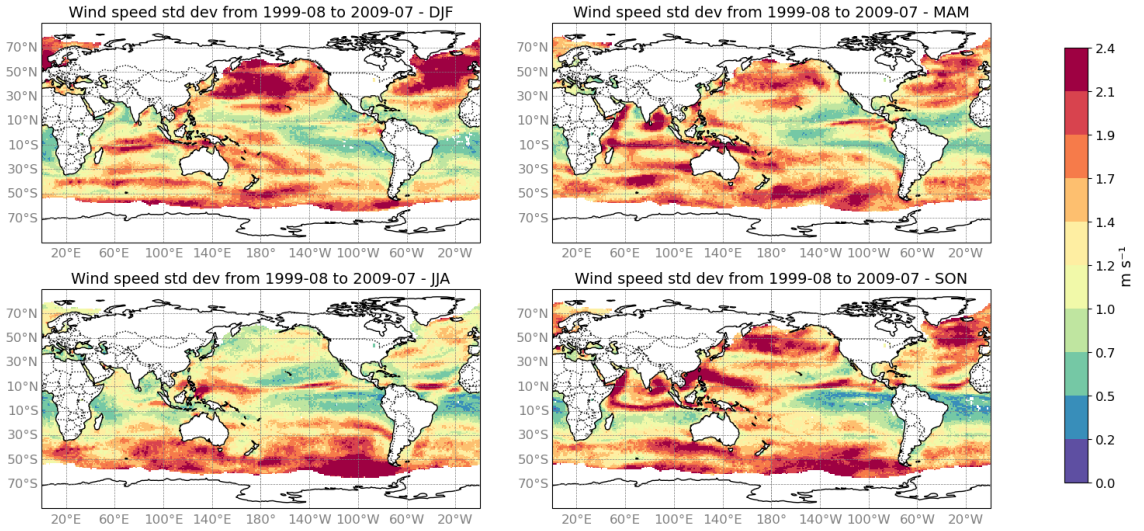

Figure 17: Wind speed std dev divided by seasons obtained from the dataset of Table 9 and 8

Figures 16 and 17 refer, respectively, to the mean speed-direction of surface wind over sea, and the standard deviation of its speed season by season. It can be seen that the areas most affected

by sustained winds are in the tropical area and at latitudes corresponding to the area just above Antarctica, with the difference that near-zero latitudes the standard deviation is close to 1°C, except for the Indian Ocean in MAM and SON. A clear seasonal difference characterizes the Indian Ocean near the coast in JJA, with sharply stronger winds than the rest of the year. High variability, on the other hand, affects the high latitudes in DJF, when winds also have higher speeds than in other months.
As for directions, the gray vectors give an idea of their seasonal average. As will also be seen from the results obtained from the next datasets referring to the surface winds, they go westward in the tropical zone, especially when looking at the Pacific and Atlantic Oceans, and eastward in the outer bands up to 70°N and 70°S. Along the coasts, however, they undergo variations, following trajectories tangent to the land, which is why in the tropical zone of the Indian Ocean it's not recorded a clear average westward wind direction.
In order to verify the validity of the results obtained so far, it is necessary to compare them with the product of ERA5 reanalysis through the metrics defined in the previous section.

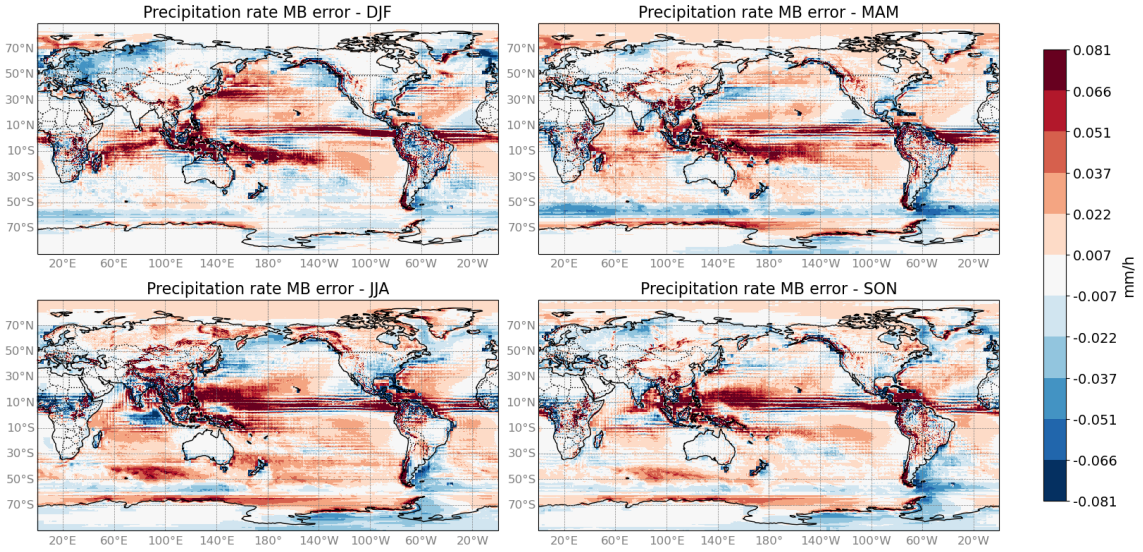

Figure 18: MB error precipitation rate comparing observational data and reanalysis data coming from ERA5

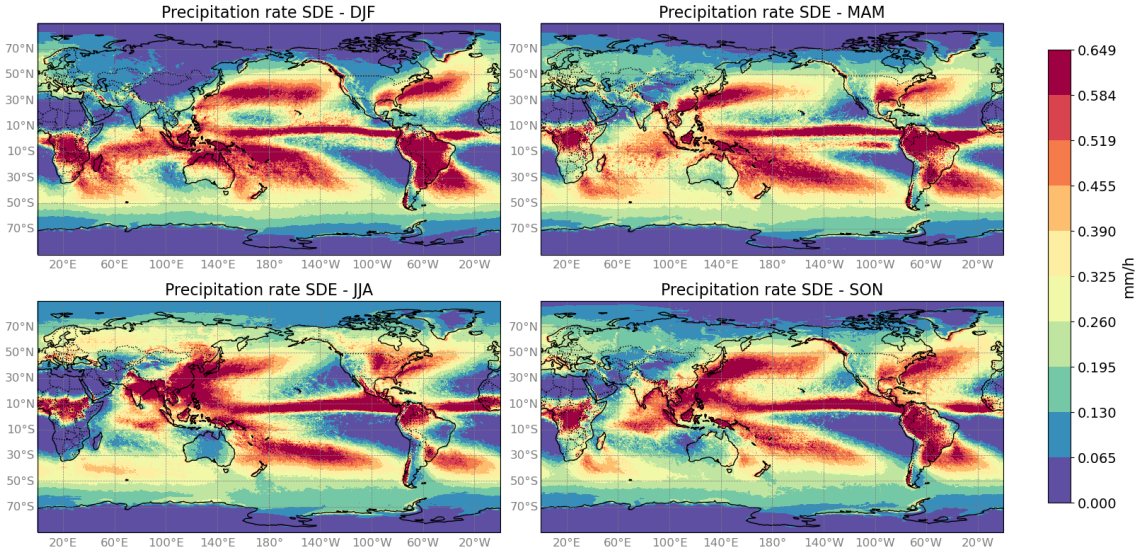

Figure 19: SDE precipitation rate comparing observational data and reanalysis data coming from ERA5

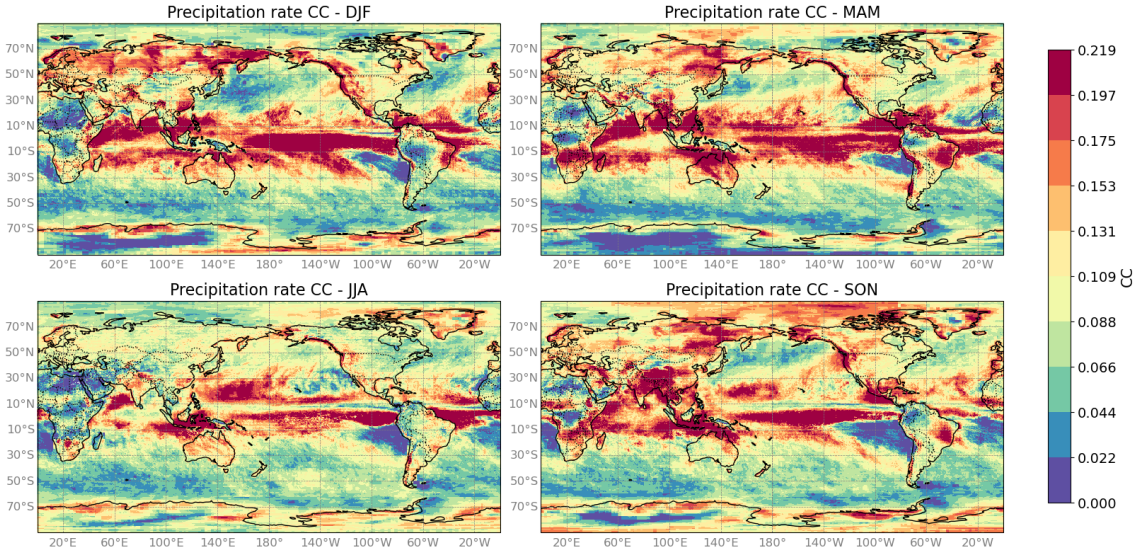

Figure 20: CC precipitation rate comparing observational data and reanalysis data coming from ERA5

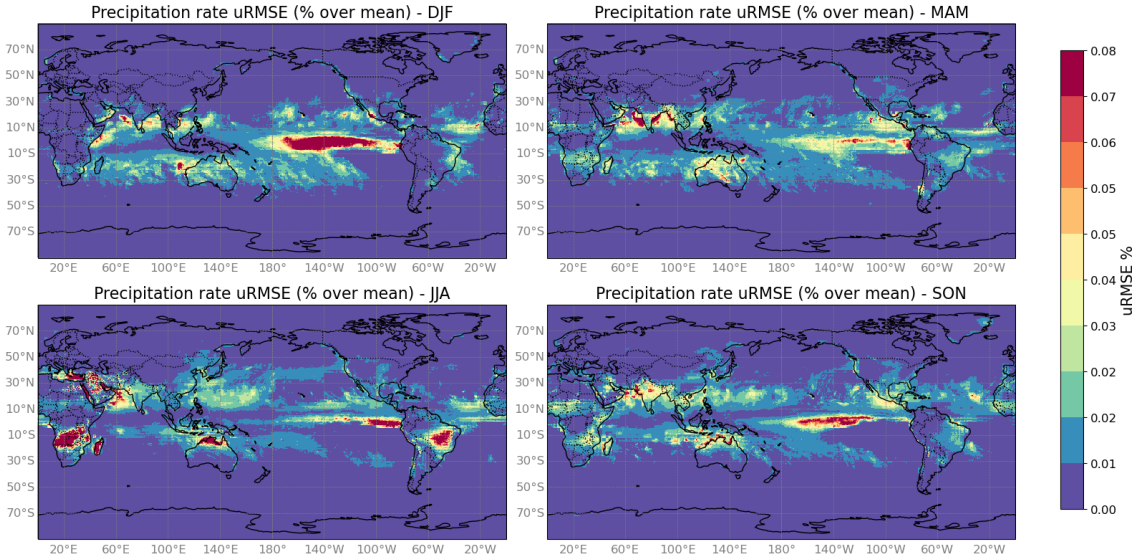

Figure 21: uRMSE precipitation rate comparing observational data and reanalysis data coming from ERA5

For an initial evaluation of the reliability of the datasets used, the MB error was calculated (figure 18) after converting precipitation flux in precipitation rate, from $\frac{kg}{m^2 s}$ to $\frac{m}{h}$ simply multiplying by 3.6. As a result, the red points related to higher values tend to occur on mountain ranges such as the Andes, South Asia, or Central Africa, while globally larger errors correspond to points on the map where precipitation is greater than average (equatorial line and West PAcific Ocean). On the other hand, with regard to the SDE (figures 19), in areas subject to greater precipitation the difference between the two standard deviations touches and exceeds 0.6 $\frac{mm}{h}$. This is due to the fact that the data available from satellite observations are provided at a monthly frequency unlike ERA5 data obtained with a 6 hr time step, which will be subject to greater variation and thus to higher values of standard deviation. In figures 20 the correlation between the two datasets is relatively low (around 0.1 for each season) with some negative values in areas where precipitation is rare, such as near the west coasts of Latin America, some areas between Central and North Africa, and Antarctica. As in the case of the SDE, the uRMSE also records values on the order of of $10^{-6}\,\frac{mm}{h}$ in the less rainy areas and two orders higher in the areas most affected by precipitation. In **??** high values of uRMSE appear in the Eastern Pacific along the equator, mostly in DJF, in the south of Africa, in the north of Australia and in the middle of Brazil in JJA. Also the Indian Ocean is colored by reddish colours in all the seasons, signifying high values of uRMSE.

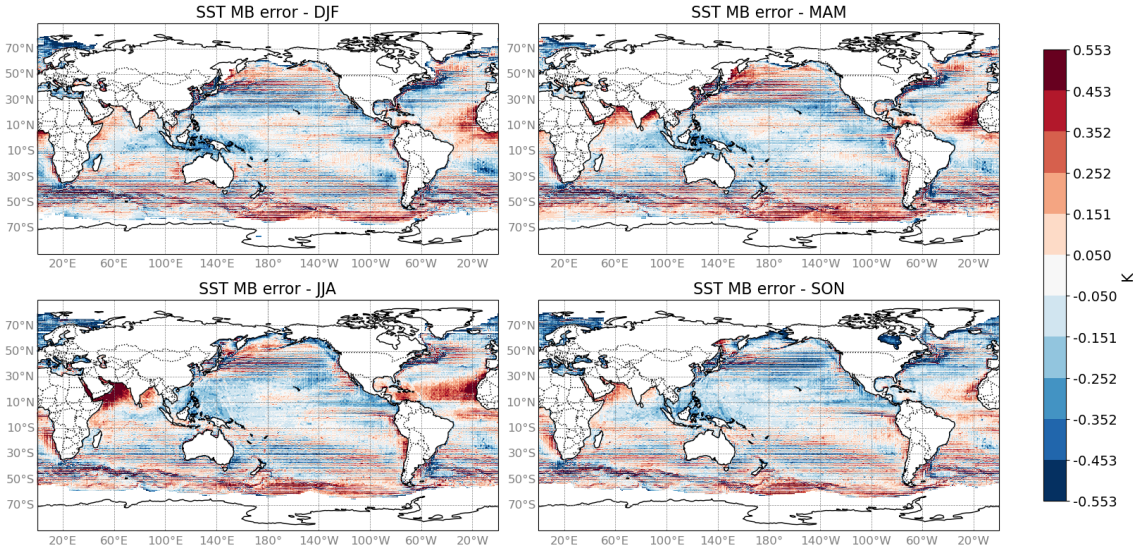

Figure 22: MB error sea surface temperature comparing observational data and reanalysis data coming from ERA5

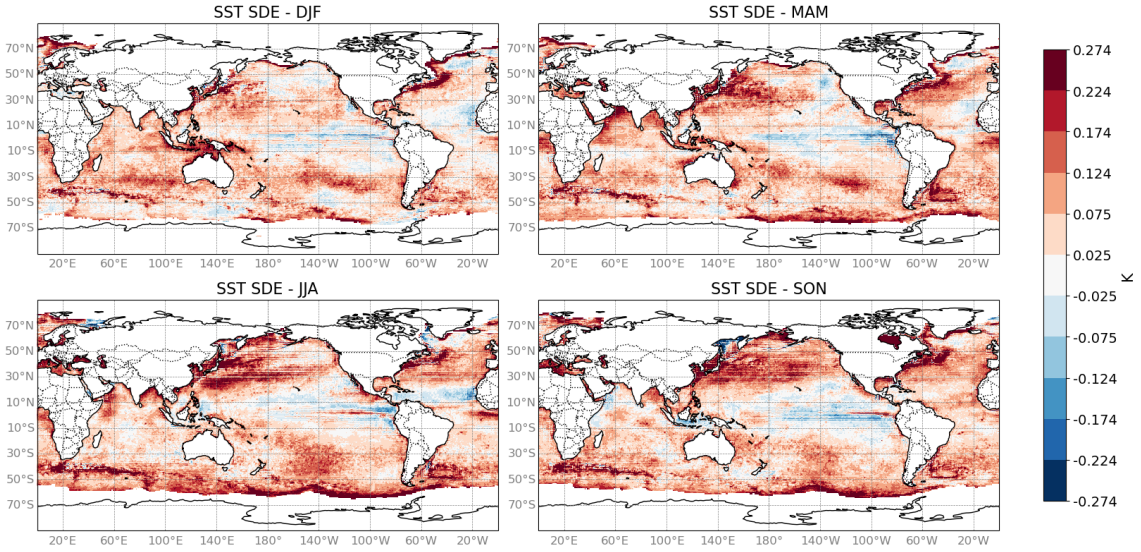

Figure 23: SDE sea surface temperature comparing observational data and reanalysis data coming from ERA5

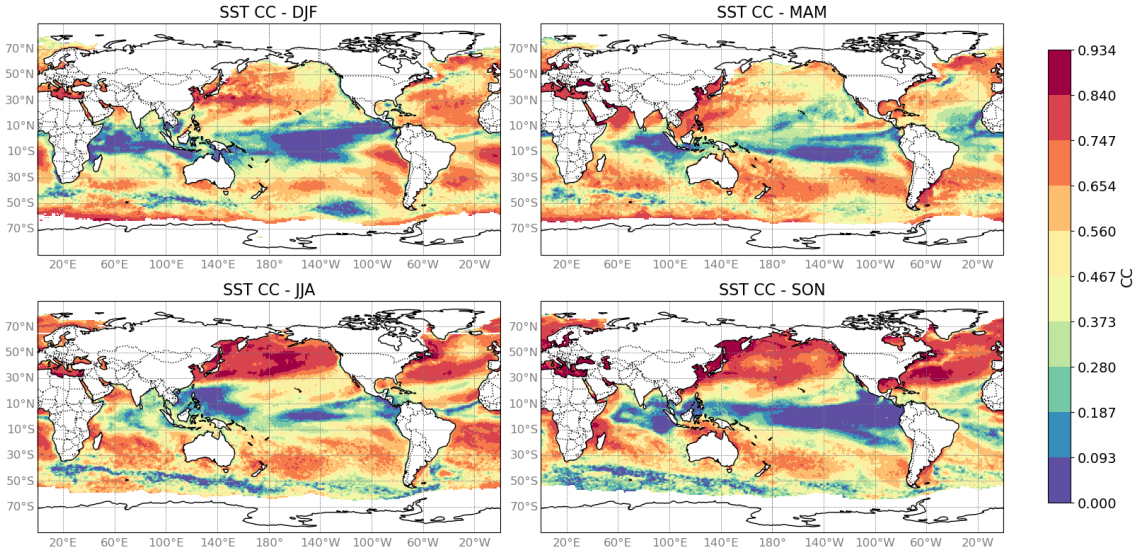

Figure 24: CC sea surface temperature comparing observational data and reanalysis data coming from ERA5

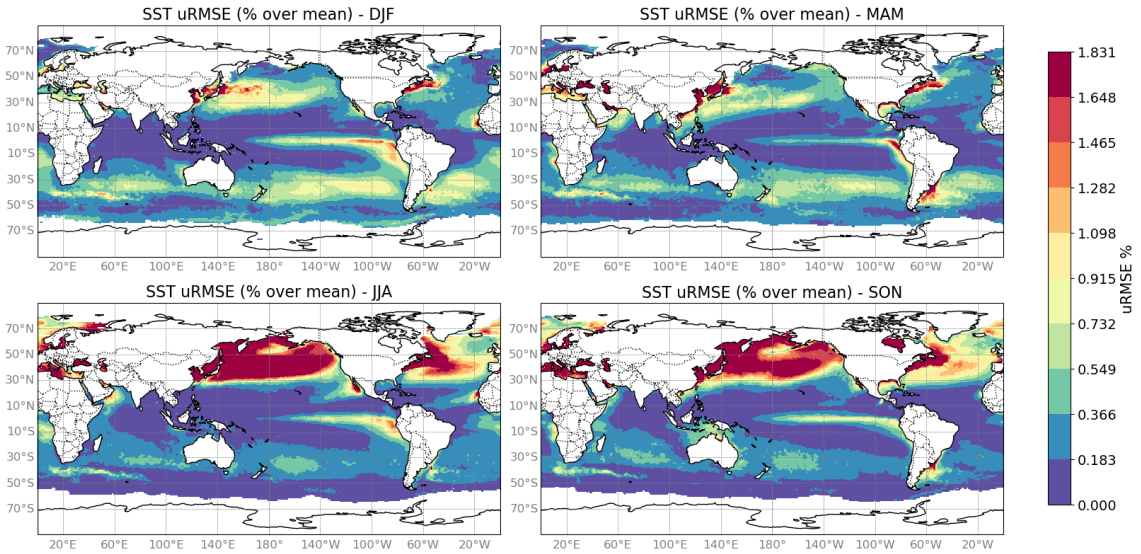

Figure 25: uRMSE sea surface temperature comparing observational data and reanalysis data coming from ERA5

Regarding the SST observational and reanalysis results, although the regions where MB values are lowest are around the equator, figures 22 exhibits ethereogenicity on unmasked points, rarely reaching values close to 0.5 K, mainly in the west african coast in all the seasons and in the North

Indian along the coasts in JJA and MAM. The prevalence of the blue colour indicates that globally the observational values are higher than the reanalysis. The opposite occurs for the SDE (figure 23) with the prevalece of reddish colours except along the equator, while observing the cross-correlation values in the eastern area of the mid-Pacific Ocean, particularly in DJF and SON, and in parts of the Indian Ocean in DJF, MAM and SON, they are close to 0, while on average the values are above 0.5, with latitudes above 30°N characterised by a strong correlation especially in JJA and SON (figures 24). Substantial differences, on the other hand, in the values of uRMSE (figure 25) with the Mediterranean area and other coastal areas (Latin America-Eastern Pacific Ocean, Asia-Western Pacific Ocean) with which values above the 1.5% of the mean are associated in all 4 panels, as is the case for the belt north of 30°N in JJA and SON. uRMSEs of an order of magnitude lower, however, are recurrent at in the Indian Ocean and the Western Pacific Ocean, as well as the band above the Antarctic zone mainly in SON and JJA. Next lines refer to MSLP data resulting from a reanalysis process (ERA5). From the images produced below it can be observed the higher resolution and the advantage of having more information on points that were not covered in previous datasets.

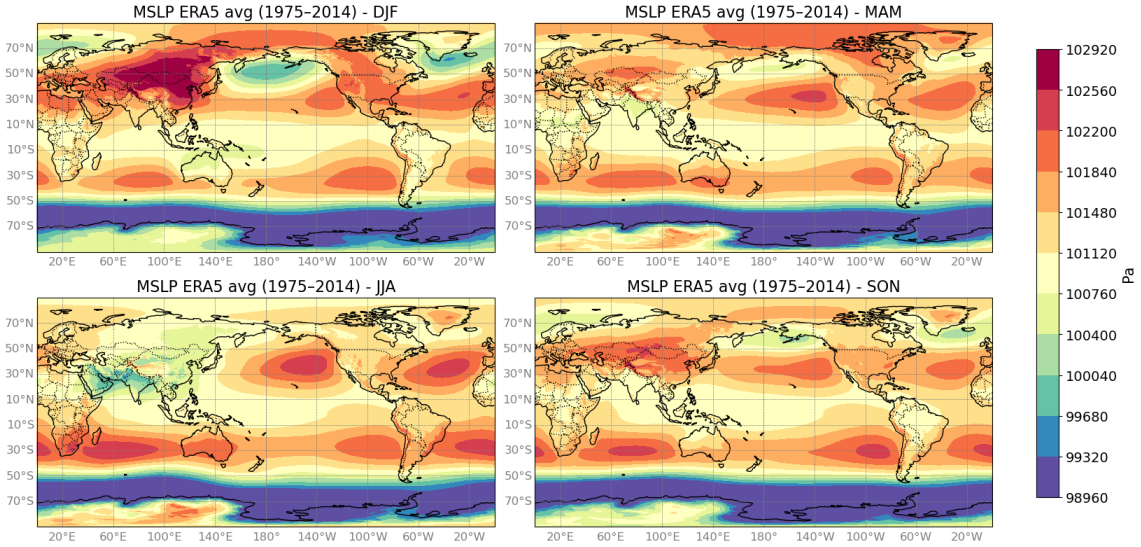

Figure 26: Mean sea level pressure averaged over the period 1975-2014, as results coming from ERA5

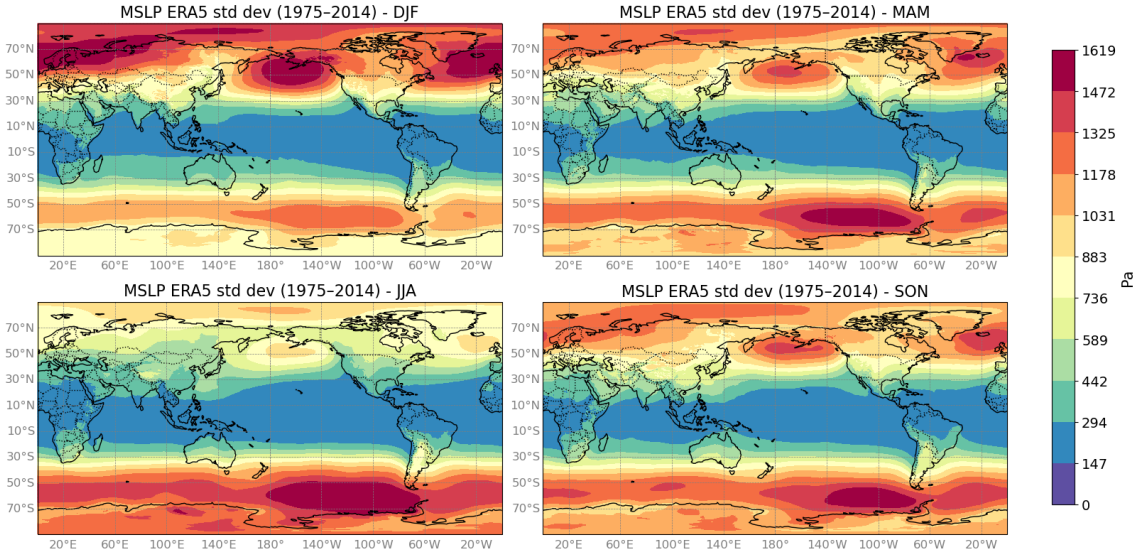

Figure 27: Mean sea level pressure std dev over the period 1975-2014, as results coming from ERA5

Analyzing the mean sea level pressure over the globe, there is a consistency among the 4 seasons under 30°S of latitudes (figure 26). Above that latitude generally the DJF season differs from the others, with a low mean sea level pressure recorded in the Central North Pacific Ocean and in the North Atlantic Ocean, and high values in central Asia. The standard deviations plots (Figure 27) suggests that the variance increase going towards the poles. Its minimum values are reached in the tropical area along all the latitudes, whilw the maximum variability affects high latitudes. During DJF above 50°N the standard deviation assume high values, reducing them in JJA.

	Precipitation Flux	**Sea Surface Temperature**	**Northward and Eastward Wind**
Start Date	1979-01-01	1981-09-01	1999-08-01
End Date	2017-10-01	2017-12-31	2009-10-31
Frequency	Monthly	Monthly	Monthly
Spatial Resolution	1.25° x 1.25°	100 km	1° x 1°
Source ID	GPCP-V2.3	ESA-CCI-SSTv2-1	QuickSCAT-v20110531
Units	$\frac{Kg}{m^2 s}$	° C	$\frac{m}{s}$

Table 2: Overview of observational variables and their attributes.

3.2 Evaluation of the CMCC-CM3 model

This paragraph is devoted to the analysis of the variables already mentioned above in the current climate, obtained through simulations using the CMCC-CM3-LT model. In this sense, confirmed

the reliability of the ERA5 data, the following charts show the seasonal comparison between the simulated and reanalysed data in the present.

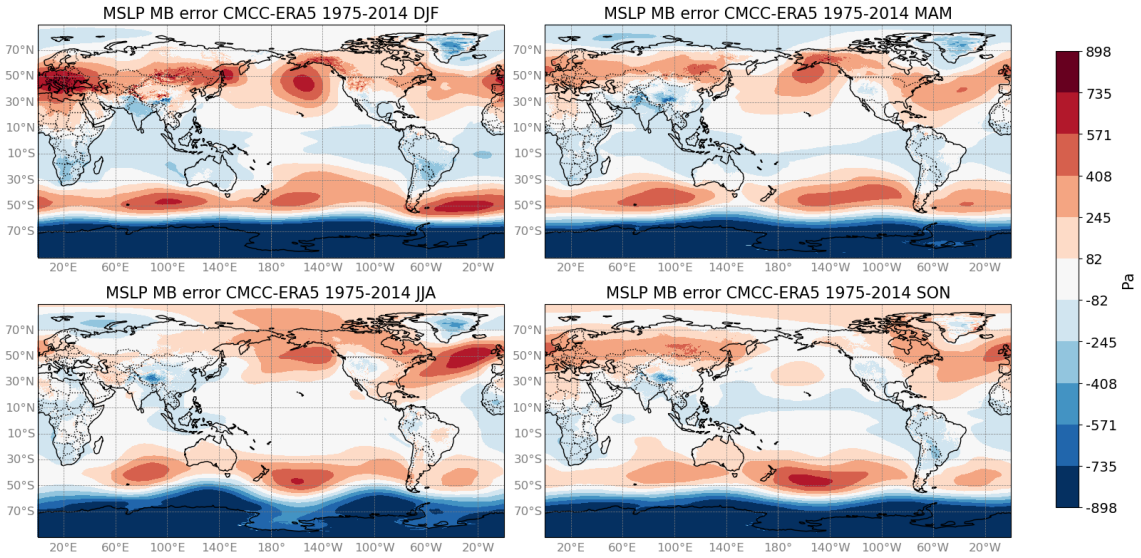

Figure 28: MB error mean sea level pressure comparing CMCC-CM3 simulations and reanalysis data coming from ERA5

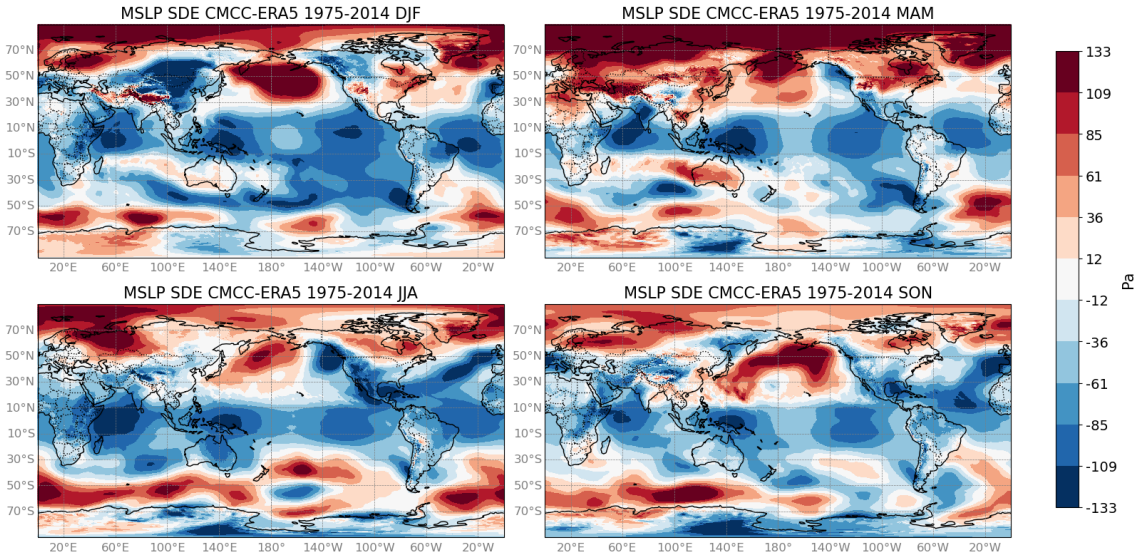

Figure 29: SDE mean sea level pressure comparing CMCC-CM3 simulations and reanalysis data coming from ERA5

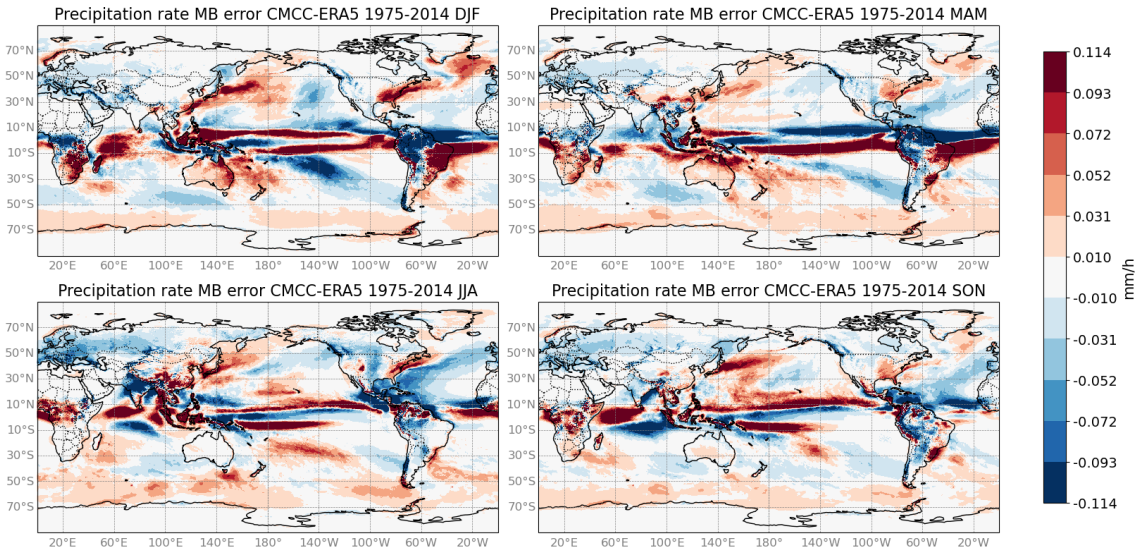

Figure 30: MB error precipitation rate comparing CMCC-CM3 simulations and reanalysis data coming from ERA5

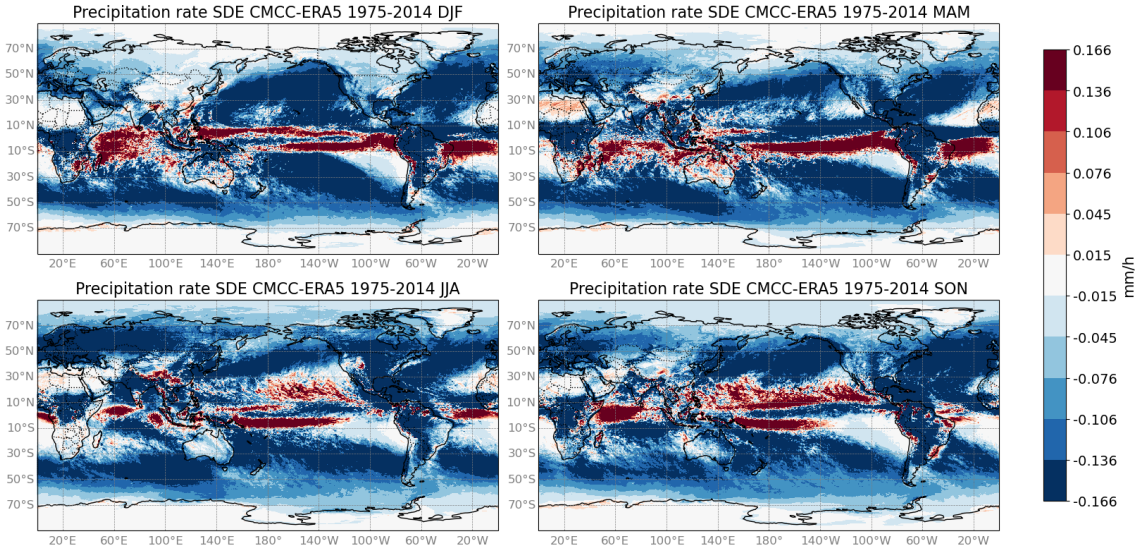

Figure 31: SDE precipitation rate comparing CMCC-CM3 simulations and reanalysis data coming from ERA5

Figures 28 and 29 plot the values of MB and SDE about the mean sea level pressure comparison between ERA5 and CMCC-CM3 data. While the MB values at low latitudes seem to be in a negligible way understimated by the model, at latitudes below 60°S in all seasons the ERA5 data

give seasonal averages of MSLP up to 700 Pa compared to simulations. In the range between 30°S and 60°S, higher values are systematically obtained from simulations, as for the North Atlantic, the North Pacific, Europe, which reaches its peak in DJF, and Asia, except in JJA. In contrast, SDE values are more heterogeneously distributed with a prevalence of negative values, corresponding to higher ERA5 averages, in the tropical region.
Figures 30 and 31 report the seasonal values of MB error and SDE about precipitation rate. Larger differences between averages occur in the rainiest areas (12) such as the equatorial zone, with alternating overstimated and understimated values, while almost no differences are detected in North Africa, Antarctica and, only in JJA, in the southern Africa, corresponding to the areas with the least precipitation on average. In Europe, the greatest discrepancy between model and reanalysis results is measured in JJA, with low values, however, in the Mediterranean Sea. Other areas whose MB error values vary seasonally are South America, with high differences in the northern area, mainly in DJF and MAM with the west coast tendencyally understimated by the model and the east coast overstimated. In Australia high differences are returned only in DJF and MAM. Indonesia and other islands between the Pacific and Indian Oceans are always subject to high MB error values. As regards the SDE reddish colours occupies the low latitudes, but taking into account that the model data were produced at a daily frequency as opposed to the 6hrly frequency of the reanalysis data, leading to highest values found where the mean precipitation flux is higher. In fact, the SDE takes values close to zero in North Africa, especially in DJF, and in South Africa in JJA. Other near-zero values are recorded towards the east coasts of Africa and South America between 10°S and 30°S, areas also characterised by low rainfall, while high SDE values colour the regions of India and Central America and the tropical area of South America, mainly in DJF and MAM.

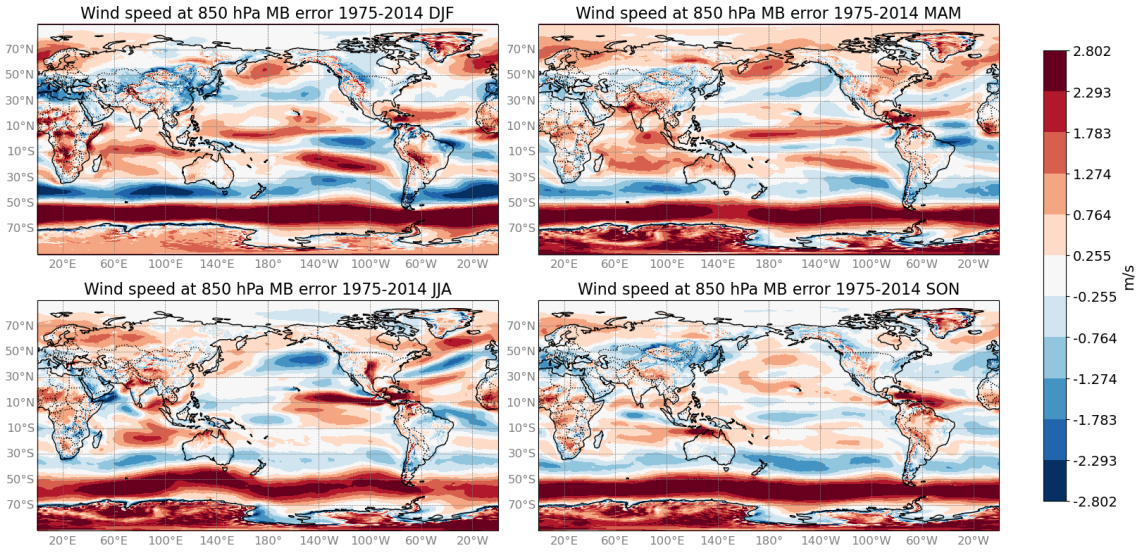

Figure 32: MB error wind speed at 850 hPa comparing CMCC-CM3 simulations and reanalysis data coming from ERA5

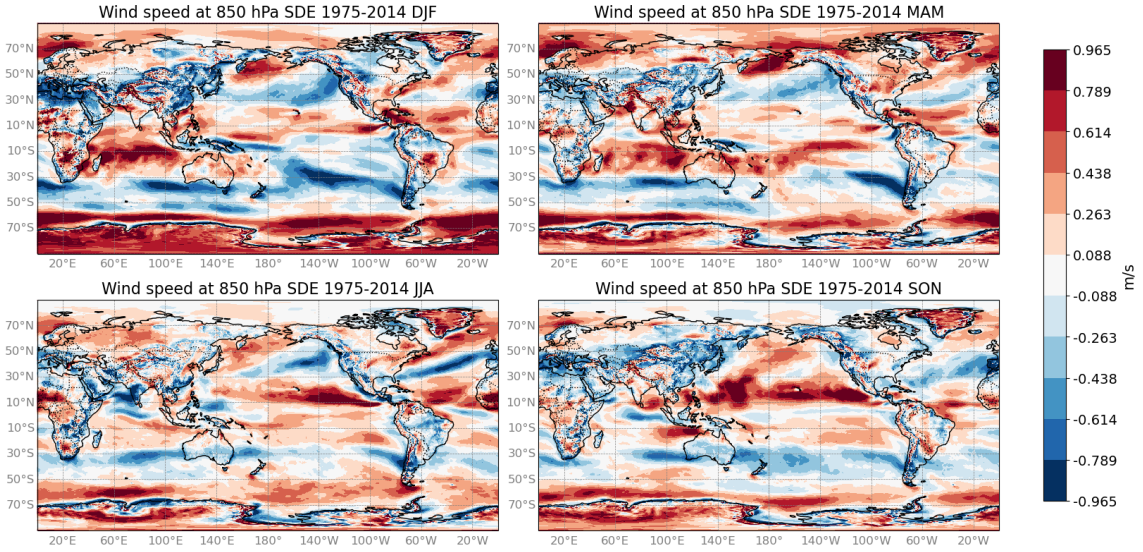

Figure 33: SDE wind speed at 850 hPa comparing CMCC-CM3 simulations and reanalysis data coming from ERA5

Substantial differences in MB values, above 2 $\frac{m}{s}$, are mainly observed at latitudes between 50° S and 70° S. On land, the largest deviations between the calculated averages are found in Western Europe during SON and DJF and along the East Asian coasts during DJF, understimated by the model, and in Central Africa during DJF and JJA, in India during MAM, where the model returns higher values than reanalysis. Significant systematic errors are also observed in several polnts aong the western coasts of North and South America in all seasons. As regards the Ocean, the mean bias values in SON are smaller overall, although they show high values along the equatorial line in the Atlantic Ocean. In DJF, on the other hand, there is a particularly pronounced mean bias in the South Atlantic with higher reanalisys values, and South Pacific and South Indian basins with higher simulation results, while in JJA high values are shown in the East North Pacific, North Atlantic and North Indian oceans. During MAM, the highest differences are concentrated in the tropical band, with the entire Indian Ocean characterised by simulated results higher than the values given by ERA5. The difference in standard deviation, shown in Figure 33, appears heterogeneous in many regions, with error peaks along the equatorial strip in JJA and SON, and in the South Indian Ocean in DJF. Other maxima are observed in the Mediterranean basin during DJF and SON, over East Asia in DJF, both understimated by the model, and along the western coasts of the Americas in all seasons. In DJF, at latitudes under 60°S, the red colour prevalence indicates an higher variability suggested by the CMCC-CM3-LT.

3.3 Evaluation of Tropical Cyclone tracks

Results obtained in the previous paragraph let the climate model simulations to be used in order to studying the TCs evolution. In this section are exposed the outputs derived from tracking reanalysis and simulation data over the years 1980-2010. To validate the CyTRACK performances, they are compared with results extracted from IBTrACS (International Best Track Archive for

Climate Stewardship, [49]), a dataset that collects tropical cyclone observational data from WMO agencies, Regional Specialized Meteorological Centers (TCWCs) and other national agencies ([50]). The results shown below come from what are referred to in the dataset as *usa_agency*, of which NHC (National Hurricane Center), JTWC (Joint Typhoon Warning Center), CPHC (Central Pacific Hurricane Center) as well as data for the WMO Regional Specialized Meteorological Center at Miami and Honolulu [51] are part. As anticipated in the introduction paragraph about the Cy-TRACK algorithm descripion, next lines indicate the values used about the tracking process over ERA5 and CMCC data.

- *core_criteria_length* = 3
- *max_wind_speed_threshold* = 8 m/s
- *outer_wind_speed_threshold* = 6 m/s
- *filter_center_threshold* = 400 km
- *dist_threshold* = 650 km
- *critical_outer_radius* = 100 km
- *dr_res* = 100 km
- *d_ang* = 10 degrees
- *rout* = 1000 km
- *terrain_filter* = 0 m
- *intensity_threshold* = 10 m/s
- *dt_lifetime* = 36 hours
- *vorticity_threshold* = 1.45e-5 1/s
- *min_slp_threshold* = 1015 hPa
- *minimum_distance_travelled* = 0 km
- *great_circle_distance* = 5.5 degrees
- *dmslp_great_circle_distance* = 200 Pa
- *radius_for_msw* = 100 km
- *mslp_anomaly_threshold* = -2 hPa

Once set the thresholds and selected the datasets containing MSLP and surface wind variables, data are given as input for the tracking algorithm. After it has been run, the code returns an output file with detailed information on the detected cyclones. The resulting file is divided in groups, corresponding to the number of identified cyclones. Each group starts with a row containing general information on the system, i. e. the searching region, an identifying number, the year of occurrence and the total number of critical points detected. The following lines describe instead the individual

critical points that form the cyclone's trajectory. In particular, for the analysis of interest in this document, each point is described by nine columns. First two regards the date and the hour, which is purely superfluous since data are daily averages, followed by the latitude and longitude of the cyclone center. Fifth column denotes the minima central pressure (MCP), while the sixth and seventh the maxima wind speed velocity (MSW) and the size of the system computed with the method based on the wind threshold, as explained in the introduction paragraph. The last two columns concern the radial size (Radius of Outer Closed Isobar, ROCI) and its pressure (PROCI), through it's useful in order to compute the baric gradient as the difference between PROCI and MCP.

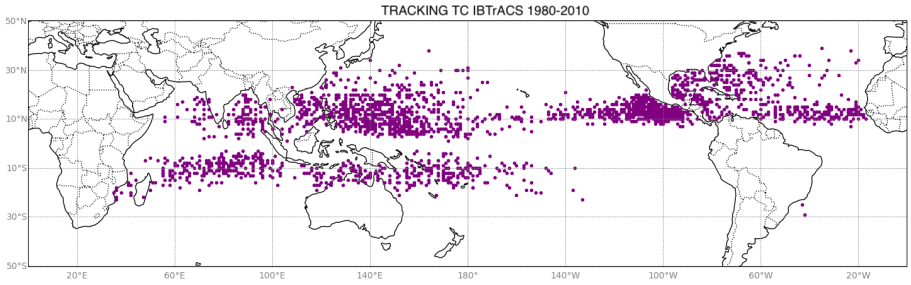

(a)

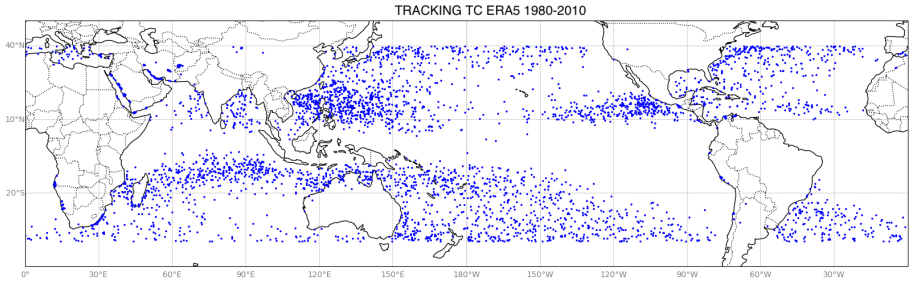

(b)

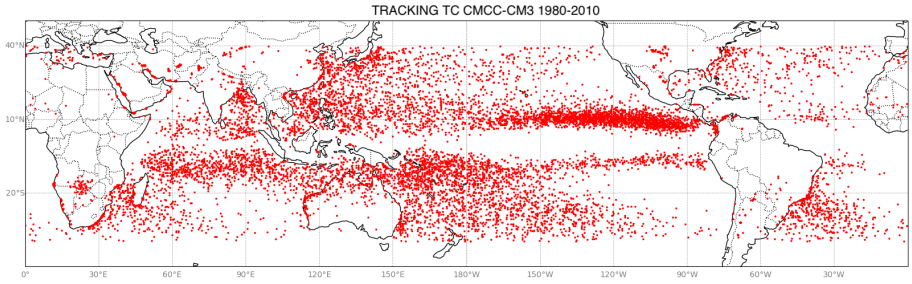

(c)

Figure 34: Initial points collected by IBTrACS (a) and detected by CyTRACK from reanalysis (b) and simulation data (c) between 1980-2010

Figures shown in figure 34 represents the initial point of the detected TCs from IBTrACS, reanalysis data and simulated data. As expected, cyclonic genesis is absent at the equator due to the lack of the Coriolis force. Likewise, cyclone formation on land is almost null, due to the lack of energy support provided by the ocean surface. However, numerous points of genesis are observed near the coasts, for example in southern Africa, the Middle East, along the east coast of North America and around Australia. Although the number of events tends to increase from IBTrACS to ERA5 and finally to simulations, the spatial distribution remains broadly similar among the three sources. The areas with the highest concentration are in the Western Pacific Ocean, between about 5° and 10°N latitude, and in a strip just above 10°N in the Eastern Pacific, near the coast of Mexico. The density plots created grouping the points in figure 34 in 3°x3° cells, make the presence of particularly active areas more evident. These include the South Indian Ocean around 10°S, the North Indian Ocean near the Indian coast, and the area north of Australia, where activity extends towards the middle of the South Pacific in a gradually decreasing manner. Significant cyclonic density is also observed in the Atlantic Ocean. Observations and reanalyses show increased activity in the North Atlantic, while simulations also indicate high density near the eastern coasts of Latin America. In all sources, cyclonic activity tends to decrease moving eastwards, being almost absent near Africa and Europe.

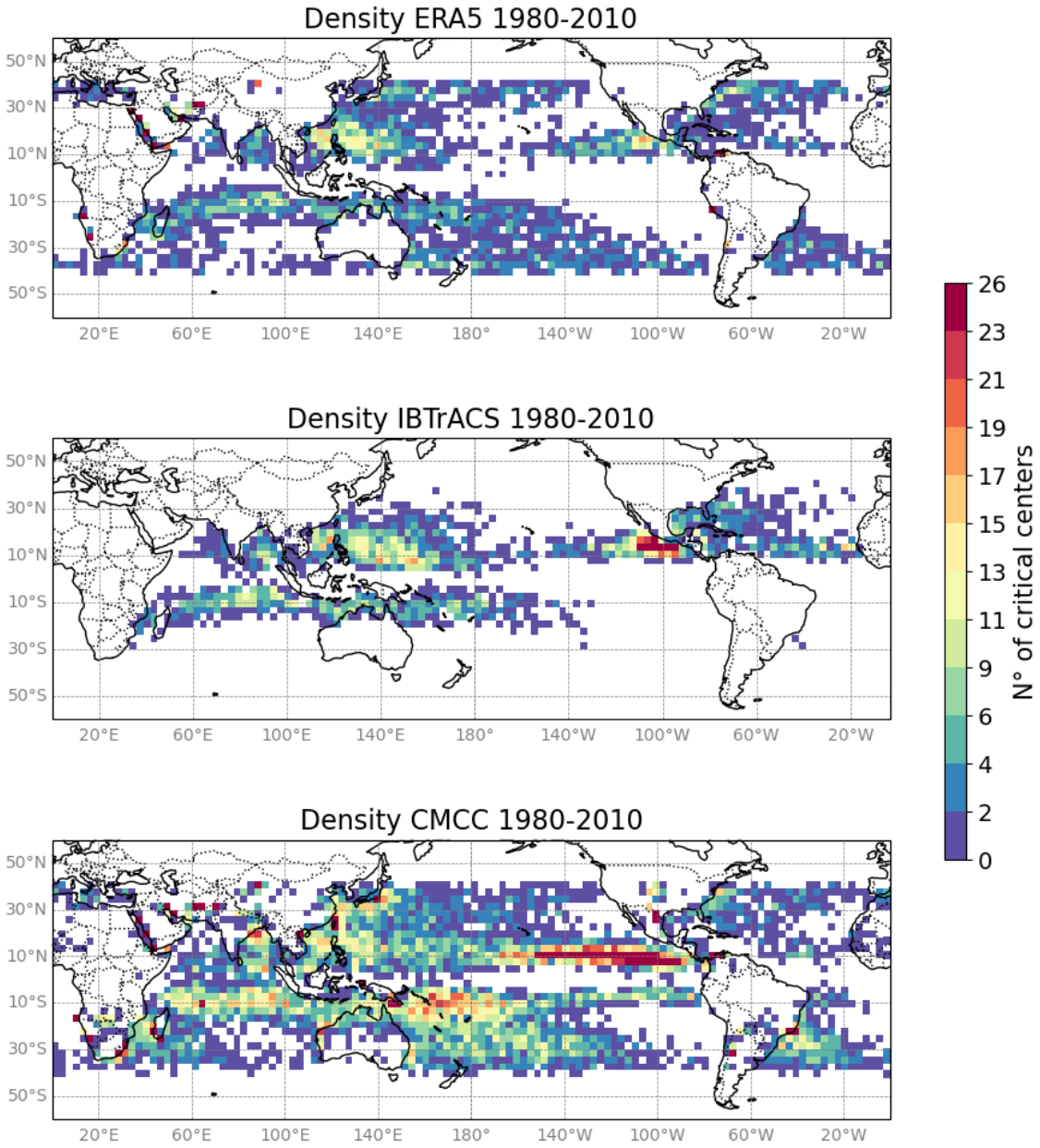

Figure 35: Density chart of initial points represented in figure 34 grouped in 3°x3°cells.

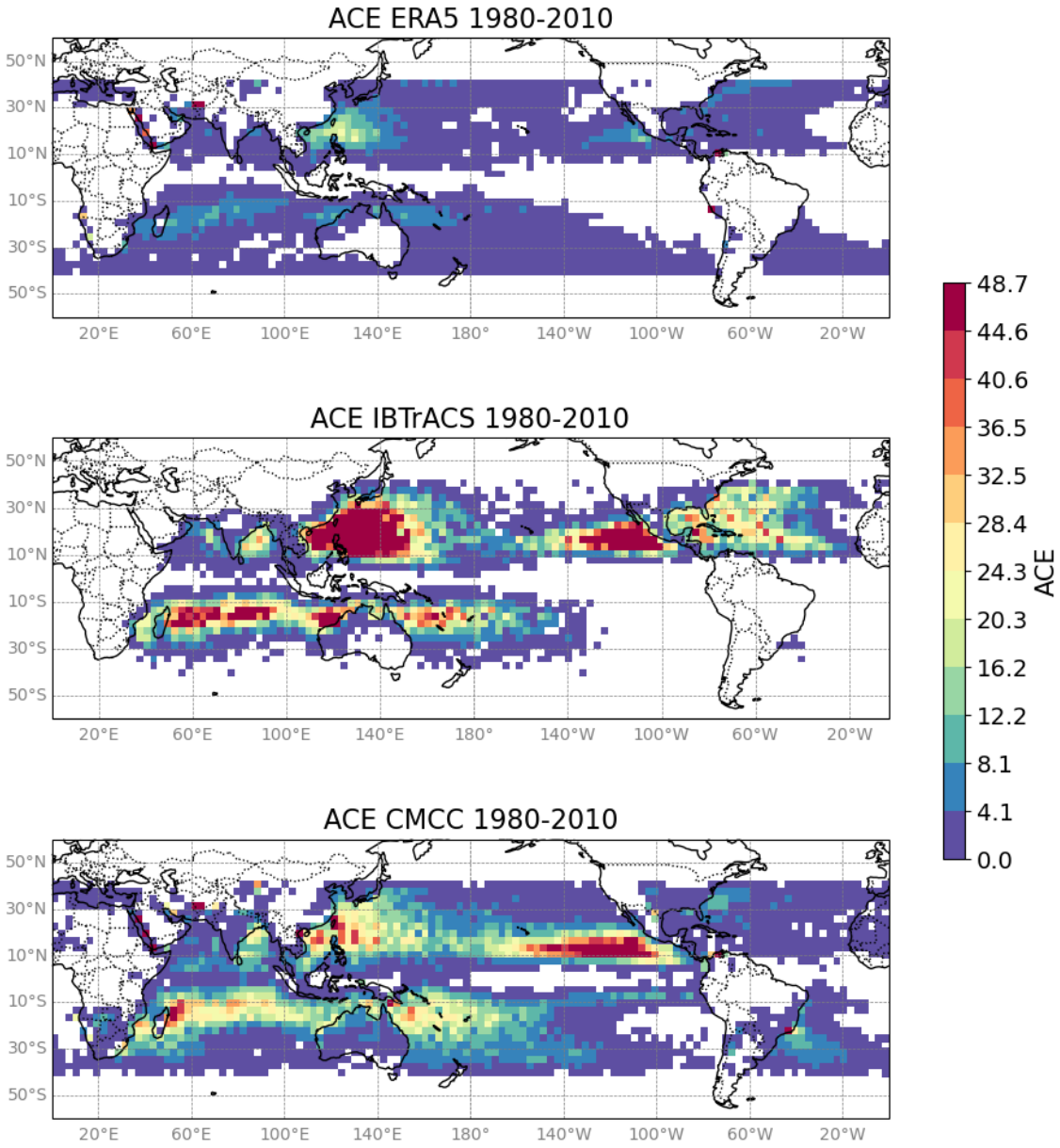

Figure 36: ACE index computed through the summation of the MSW square of all the points detected by CyTRACK and collected in IBTrACS, in 1980-2010 and with a daily frequency. The values are scaled by a factor 10^4.

To analyse cyclone intensity, the ACE index, mentioned in the first paragraph, was employed, which represents the summation of the MSW recorded during the lifetime of each cyclone, thus including information on both duration and intensity. The results are illustrated in figure 36. Al-

though the three representations show different absolute values, the general pattern is consistent: the areas with the highest ACE are located in the South Indian Ocean, on the southwest and the north of the Pacific with growing values towards the coasts.
Of particular interest is also the analysis of three specific parameters: MCP, the size of the TC and the difference between PROCI and MCP. The maps show a trend consistent with the other metrics, with lowest MCP values in the Northwest Pacific, in the band between Central America and the South Indian Ocean, and in the Southwest Pacific, similar to what was observed for ACE. In particular, IBTrACS shows more extreme and polarized MCP values, while reanalyses tend to be more moderate. The maximum cyclone size computed by CyTRACK for each cell also follows a similar behavior (38). At low latitudes areas with higher values of the size coincide with those with lower MCP, confirming the association between low central pressure and greater extent, while going towards higher altitudes the extension of the cyclone tends to increase. CyTRACK also provides PROCI values, allowing direct calculation of the pressure gradient. The resulting maps (figure 39) show similar behavior between ERA5 and CMCC, with slightly higher mean values in the reanalysis but smaller maximum peaks than in the simulations.
As highlighted by the images supplied, in IBTrACS there are significantly fewer points of cyclonic origin, concentrated in areas where the ACE and MCP indices indicate greater cyclonic activity. This suggests that IBTrACS contains data for more intense cyclones than those detected by CyTRACK in this work, discarding weaker storms, although the threshold criteria adopted in IBTrACS for the detection of MCP and MSW are less restrictive (1050 hPa and 10 knots, respectively).

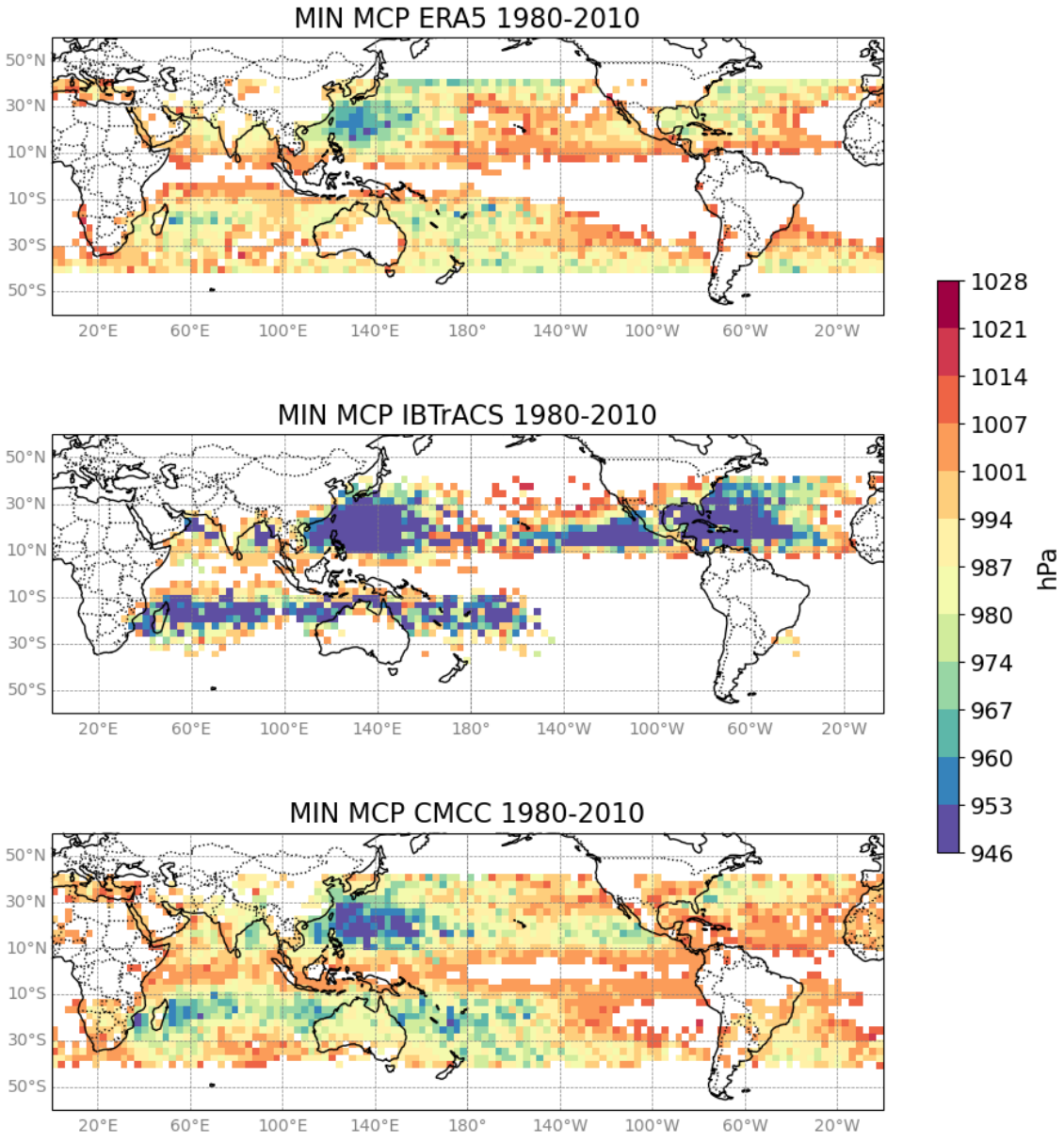

Figure 37: Minimum values for each cell of the MCP found in the three different systems.

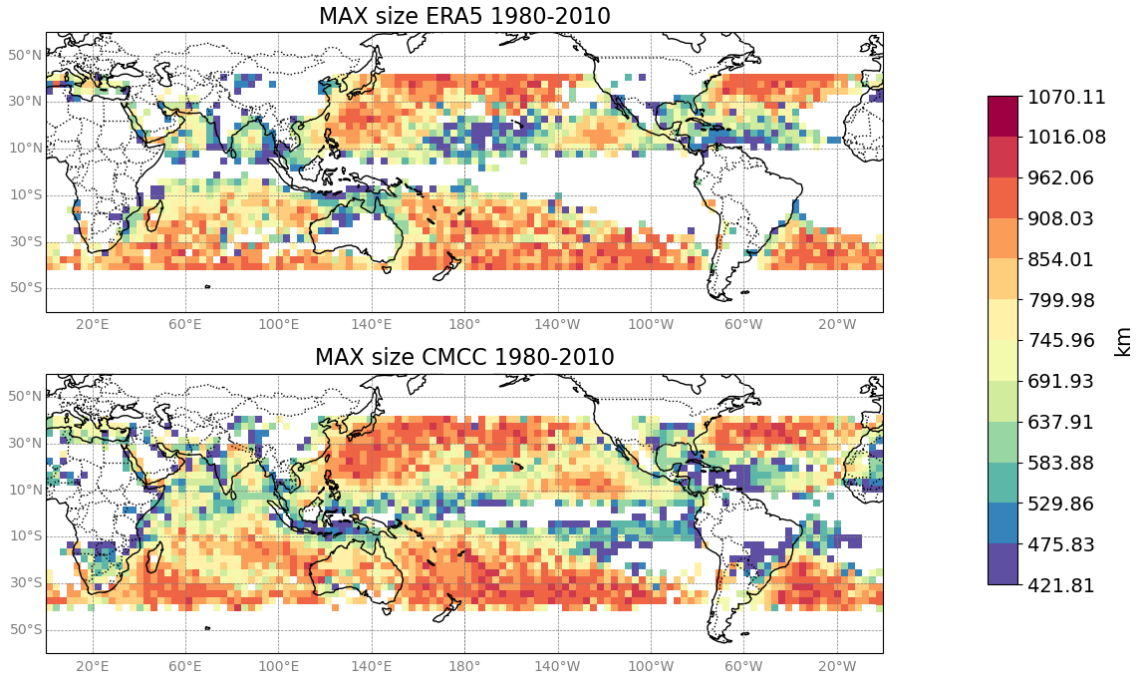

Figure 38: Maximum size of the cyclone for each cell computed by CyTRACK.

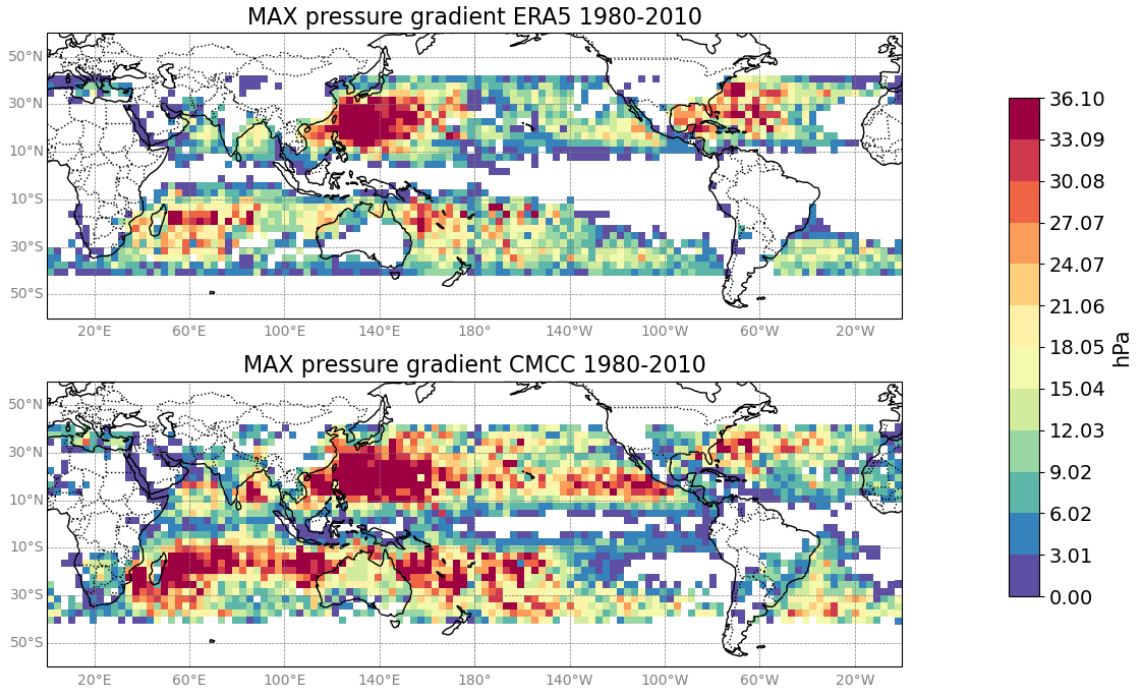

Figure 39: Maximum baric gradient between the pressure of ROCI and the MCP computed for each cell, as CyTRACK results of ERA5 and CMCC.

4 Results: Future climate (2070-2100)

Thus moving the focus to future climate, possible changes in the mean seasonal climate are analyzed here, exploiting the CMCC-CM3-LT model datasets, previously validated through comparisons with reanalyses. As anticipated in the introductory chapter, the future scenario used is SSP5, for which MSLP, surface winds, precipitation rate and the air temperature average and variability would change according to the following results.

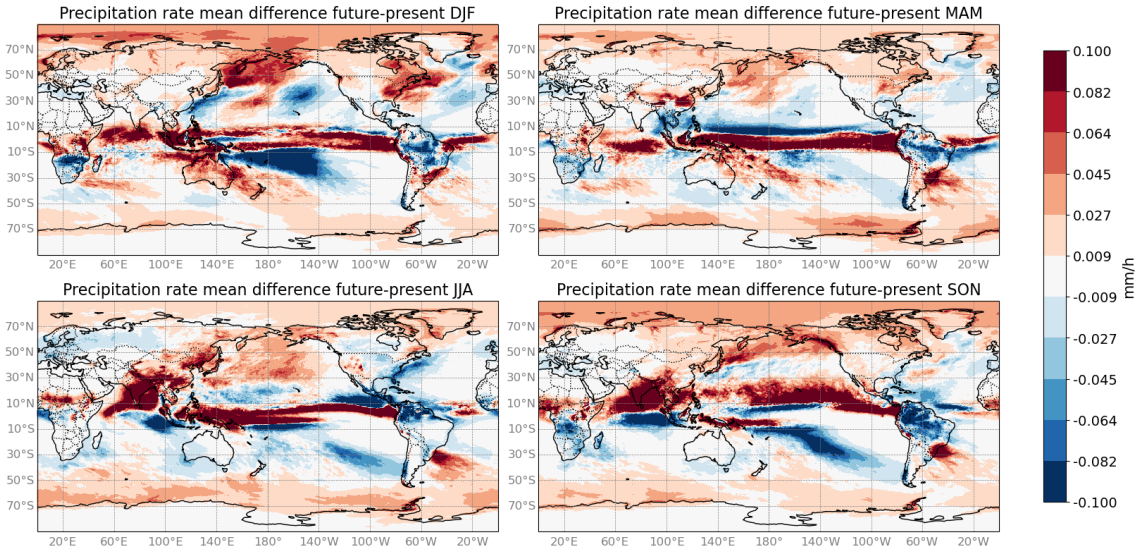

Figure 40: Difference of the mean precipitation rate between the future and present temporal periods as simulated by the CMCC-CM3-LT model.

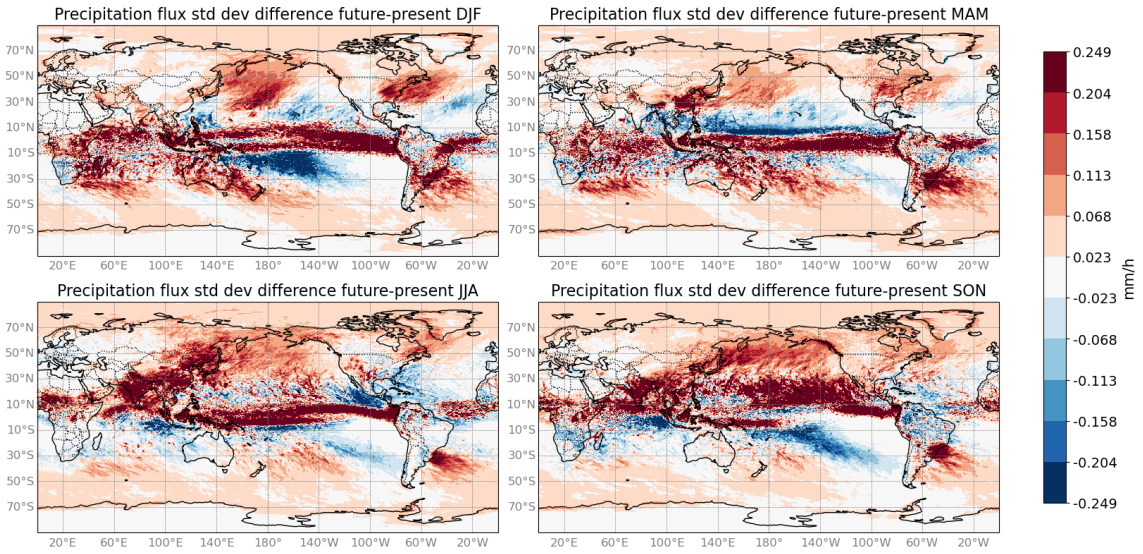

Figure 41: Difference of the standard deviation of the precipitation rate between the future and present temporal periods as simulated by the CMCC-CM3-LT model.

The figures 40 and 41 illustrate the change in seasonal mean precipitation and its variance. At high latitudes, there is an increase in both mean seasonal precipitation and its standard deviation, as well as along the equatorial line, where the sharpest increase is evident in all seasons. In the tropical belt of interest, the South Pacific is characterised by almost steady values of the precipitation rate as it approaches South America at all periods of the year. However, in its westernmost region, which extends towards more southerly latitudes, it shows an increase in precipitation, with a consistent pattern even in the standard deviation difference. Regarding the North Pacific Ocean, different trends are observed depending on the season. In DJF, a small area of the Central North Pacific toward the Asia is subject to an increase in average precipitation, while the rest of the basins show a decrease. In MAM, negative differences prevail, while in JJA, a decrease is observed at low latitudes and an increase at higher latitudes. In SON, rainfall increases almost everywhere, with the exception of a band around 30°N. In the North Indian Ocean, average rainfall increases in all seasons. In the South Indian, there is an slight increase in the centre of the basin and a decrease along the coasts in JJA, MAM and SON, while the trend reverses in DJF, with an increase along the coasts and a decrease in the centre. The South and North Atlantic Oceans show similar behaviour in all seasons, where the area characterised by reduced precipitation starts in the low latitudes and expands eastwards. The exception is the conditions in DJF, when increasing trend is observed along the coasts in th north, while in SON, MAM and JJA, the mean precipitation, as well as the variance, tend to decrease. Peaks of increase are also observed in all seasons in a region of the South Atlantic, along the southern coast of Brazil.

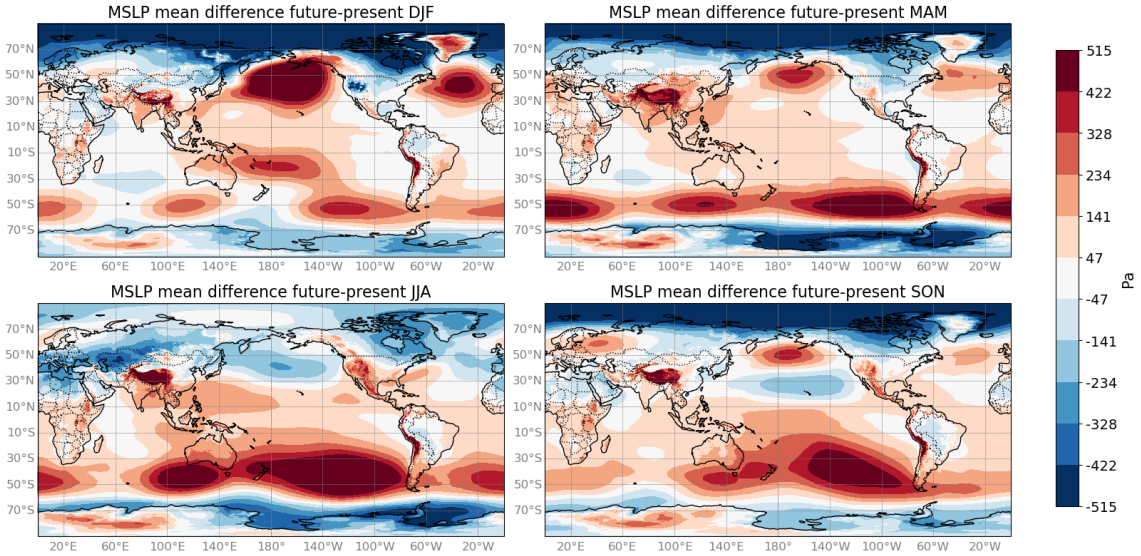

Figure 42: Difference of the mean sea level pressure between the future and present temporal periods as simulated by the CMCC-CM3-LT model.

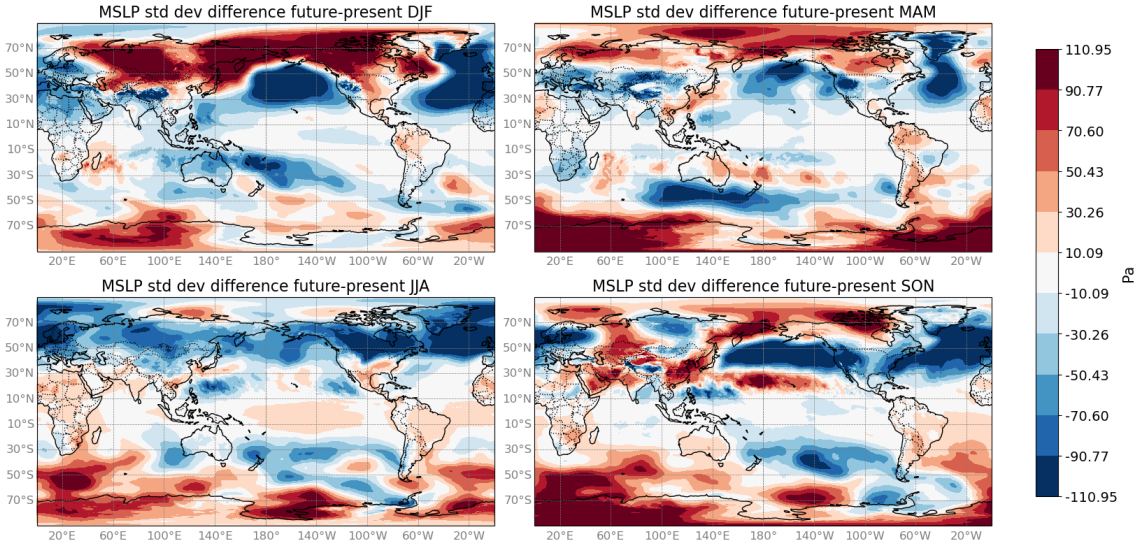

Figure 43: Difference of the standard deviation of the sea level pressure between the future and present temporal periods as simulated by the CMCC-CM3-LT model.

The evolution of the MSLP, used as input for present and future cyclonic tracking, is depicted in figures 42 and 43. At high latitudes, in both the northern and southern hemispheres, the mean pressure tends to decrease in all seasons. However, focusing on the area of interest for cyclonic

analyses, the South Pacific Ocean shows an increase in mean pressure in all seasons, with DJF and MAM that are characterised by a slighter values. The North Pacific Ocean shows a more variable behaviour according to season, with a clear increase in mean pressure during DJF and MAM, that weakens near the North American coast. A especially noticeable negative change is observed in the Central Pacific Ocean during JJA and SON, where blue colours clearly stands out. As for the Indian Ocean, the mean pressure tends predominantly to increase, as suggested by the soft red colours, with some localised exceptions along the coasts of the Middle East in SON and DJF, and in the southern sector of the ocean in DJF and MAM. The Atlantic also shows a slight increase in mean pressure, with localised almost steady values near the coasts of North America during DJF and MAM, along some coastal areas of North Africa in MAM and SON, while the JJA period is the only season with decreasing pattern. Globally, the standard deviation of the MSLP tends to decrease, as indicated by the predominance of blue tones in Figure 43. In particular, the Pacific Ocean shows a slight increase in JJA variability at low latitudes and a more pronounced increase between 10° and 30° N in SON, while between 30° and 50° N the variance decreases significantly, especially in DJF. The North Atlantic Ocean is affected by a reduction in variability in all seasons, most pronounced in DJF, while the South Atlantic shows greater variability in JJA and SON. The Indian Ocean also shows similar behaviour in the four seasons, with the western coasts tending to higher standard deviation values than the rest of the basin.

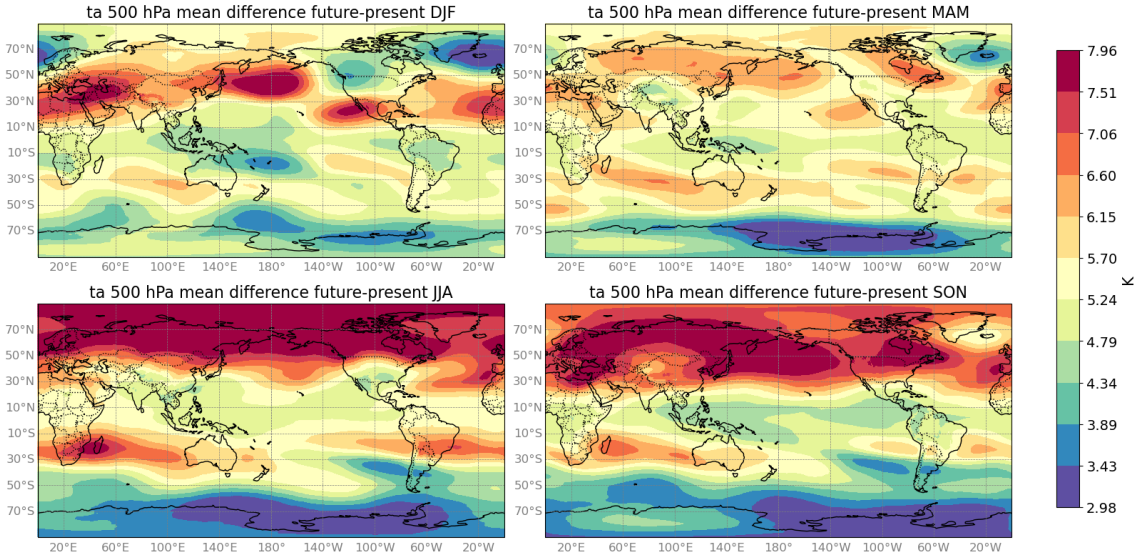

Figure 44: Difference in the mean air temperature at 500 hPa between the future and present temporal periods as simulated by the CMCC-CM3-LT model.

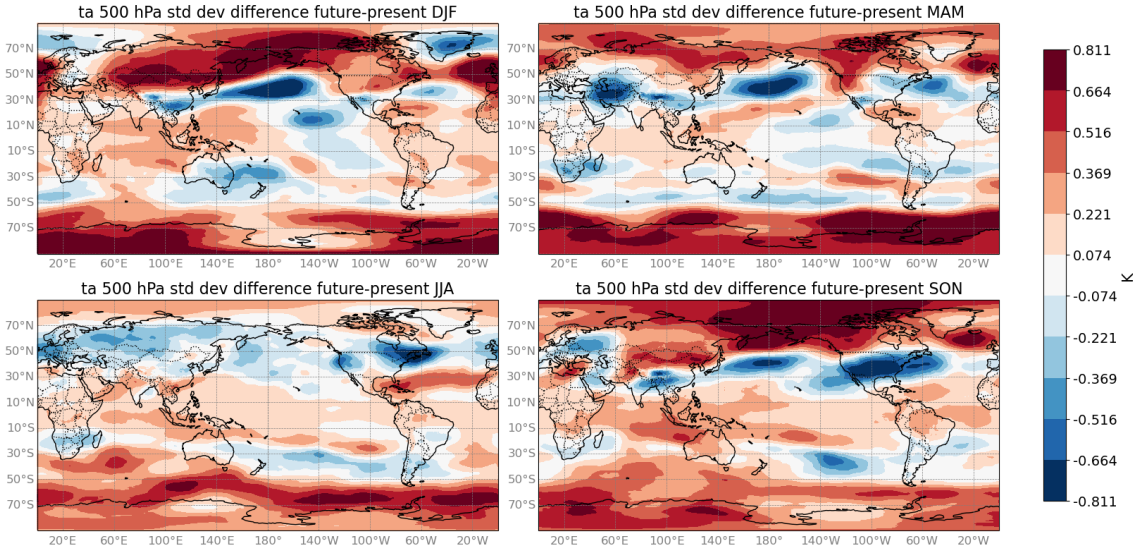

Figure 45: Standard deviation difference of air temperature at 500 hPa in the future and present temporal periods as simulated by the CMCC-CM3-LT model.

The averages temperatures at 500 hPa show positive differences in the seasonal mean. In every basin an increase is predicted following the SSP5 scenario. At latitudes above 50°N, the change is particularly marked in SON and JJA, with values above 7°C. In contrast, under the 50° S, except for DJF, the increase remains smaller, around 2°C. In the other seasons and regions the warming remains rather homogeneous between 5 and 6°C, with slightly smaller increases close to the equator, and some peak values predicted in DJF in the Eastern North Atlatic, Mediterranean Sea e North Pacific. Seasonal variability shows a general tendency to increase. Areas with less variability in the future scenario are placed mostly at mid latitudes, as well as some regions at low latitudes over the Eastern Pacific Ocean in DJF and MAM. Also the analysis regarding the air temperature at 300 hPa exhibits interesting results (figures 46 and 47). Differences among seasonal means show positive increments, while the variability, expressed as standard deviation, decrease only in few areas. In DJF the reduction is concentrated over the Eastward Pacific Ocean at low latitudes and at mid latitudes in the Westward Pacific Ocean. Also in MAM the standard deviation decrease in the Eastward Pacific Ocean, together with some areas over Asia and South Africa, while in JJA and SON the regions subject to a reduction are less extended and mainly over land. The seasonal average temperaure increase results particularly marked at mid and low latitudes, with increments above 7°C. At high latitudes the variability arise but less pronounced, excepting for the northern hemisphere, where also in JJA and SON the values are high.

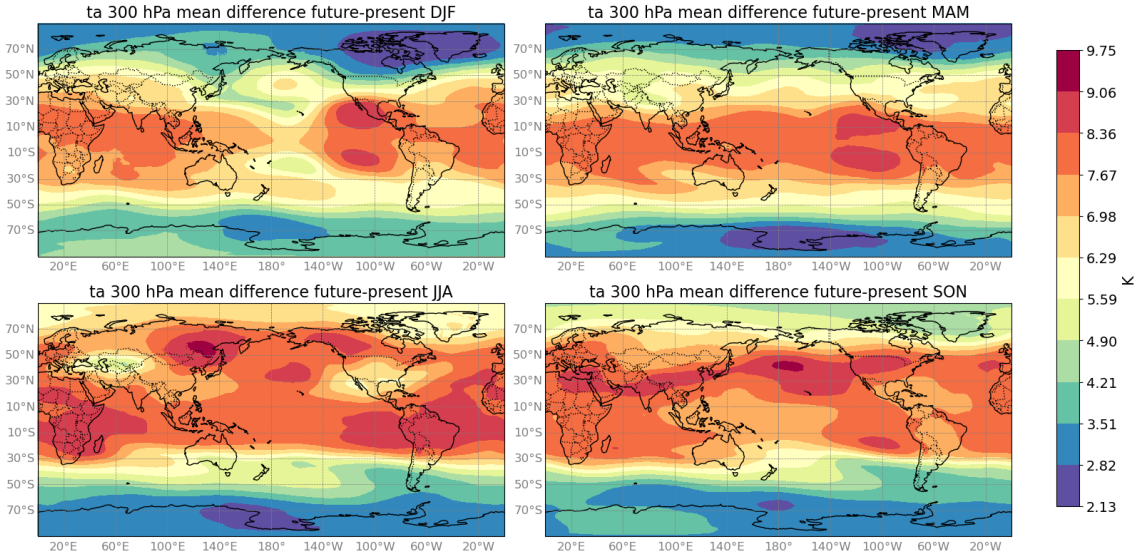

Figure 46: Difference in the mean air temperature at 300 hPa between the future and present temporal periods as simulated by the CMCC-CM3-LT model.

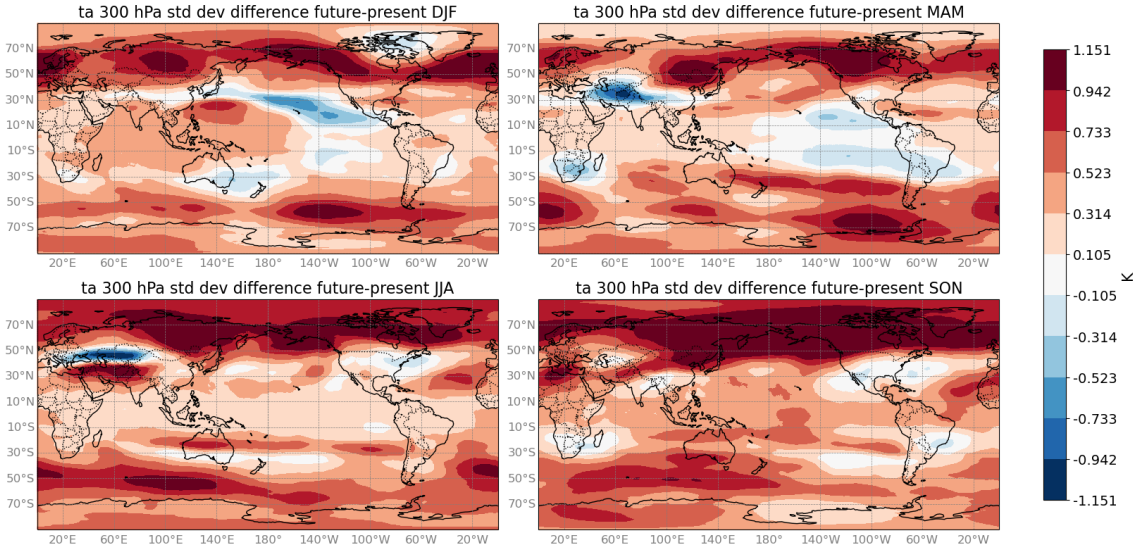

Figure 47: Standard deviation difference of air temperature at 300 hPa in the future and present temporal periods as simulated by the CMCC-CM3-LT model.

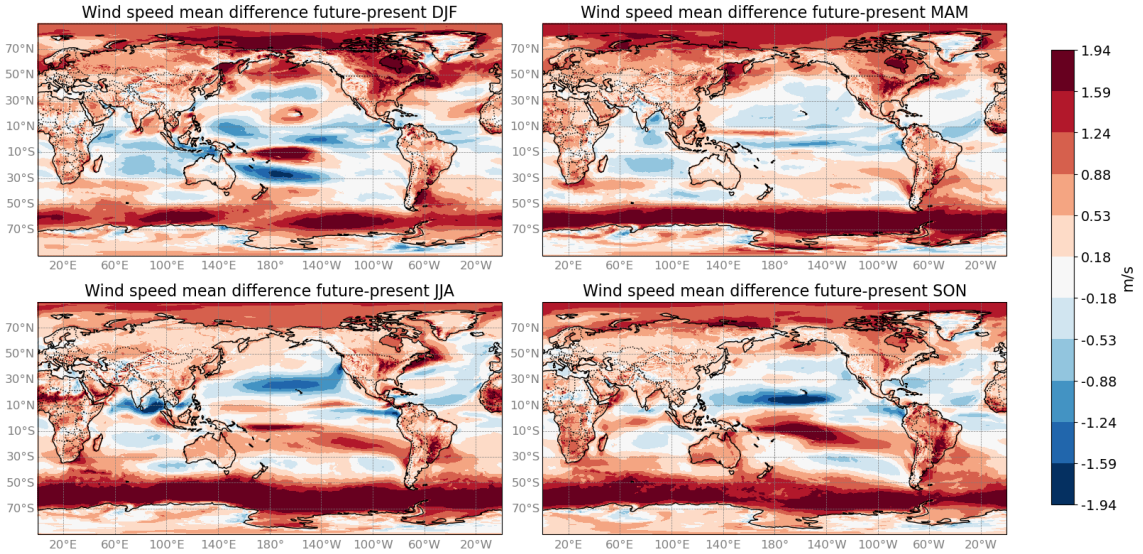

Figure 48: Difference in the mean surface wind speed between the future and present temporal periods as simulated by the CMCC-CM3-LT model.

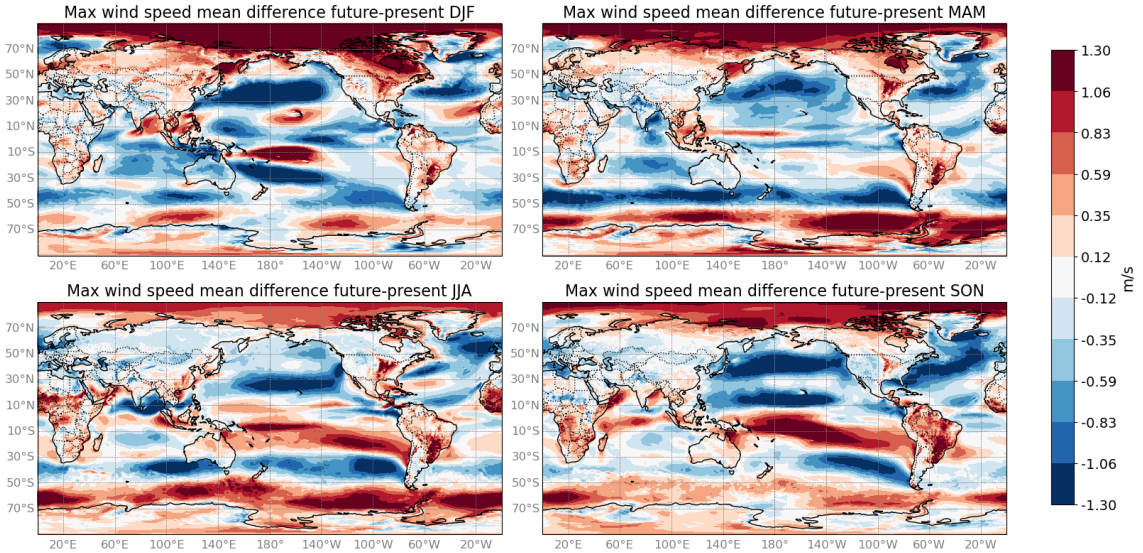

Figure 49: Difference in the mean maximum surface wind speed every 6hr between the future and present temporal periods as simulated by the CMCC-CM3-LT model.

The surface wind data, also used as input for tracking, also provide important indications of the climate changes simulated by the model. Figures 48 and 49 show a prevalence of positive differences (in red) at high latitudes of the mean surface wind speed and the average peaks every

6 hours, while areas subject to decreasing trends are mostly located at lower latitudes. However, the figures 50 and 51 display a prevailing decrease in variance, excepting for high latitudes above 70°. Analysing the individual ocean basins, the North Pacific Ocean shows a decrease in wind intensity especially in MAM and JJA, while in DJF, and to a lesser extent in SON, an area in the Central Pacific with increasing values emerges. In the South Pacific Ocean there is an increase in average wind speed at low latitudes, while at higher latitudes decreases are observed, most marked in DJF. The Indian Ocean is subject to a decrease in wind in DJF and MAM, while an increase is observed along the equator in JJA and SON. In these periods and the same basin, along the coasts an increase in wind intensity is detectable. The Atlantic Ocean, instead, shows a more variable behaviour. Infact at low latitudes a decreasing trend prevails, while at mid and high latitudes the mean differences vary seasonally. The North Atlantic Ocean is predominantly characterised by negative variations in MAM and SON, an eastward decrease in JJA, and an increase in DJF. Along the coasts, positive changes generally appear. The South Atlantic Ocean is dominated by positive values in all seasons, especially far from the equator, with a greater extent of decreasing areas in DJF. Although the seasonal mean wind tends to increase in many regions, the standard deviation only increases in specific areas and seasons. In the North Pacific basin, for example, the variance decreases in MAM, except for some Asian coastal areas. The same happens in DJF, with the exception of an equatorial strip in the Central Pacific. In JJA, the picture is more fragmented, with some areas increasing both in the centre of the basin and along the Asian coasts. In SON, an increase is observed between 10° and 30°N. In the South Pacific Ocean, the variance increases near the northern coasts of South America in all seasons. In JJA, positive differences dominate at low latitudes, while in MAM, increases are observed at mid latitudes in the centre of the basin. The North Atlantic basin shows a decrease in variance in all seasons, while the South Atlantic shows a more varied seasonal behaviour, with an increase in the central area in SON and in high latitudes in DJF. Finally, in the Indian Ocean, similar patterns are observed in JJA and SON, with an increase in variance in the north-west and along the coasts, and a slight increase in the central part of the south basin. Negative values prevail in MAM, with the exception of a small southern area, while in DJF the variance increases along the equator and in the southern part approaching the African coast.

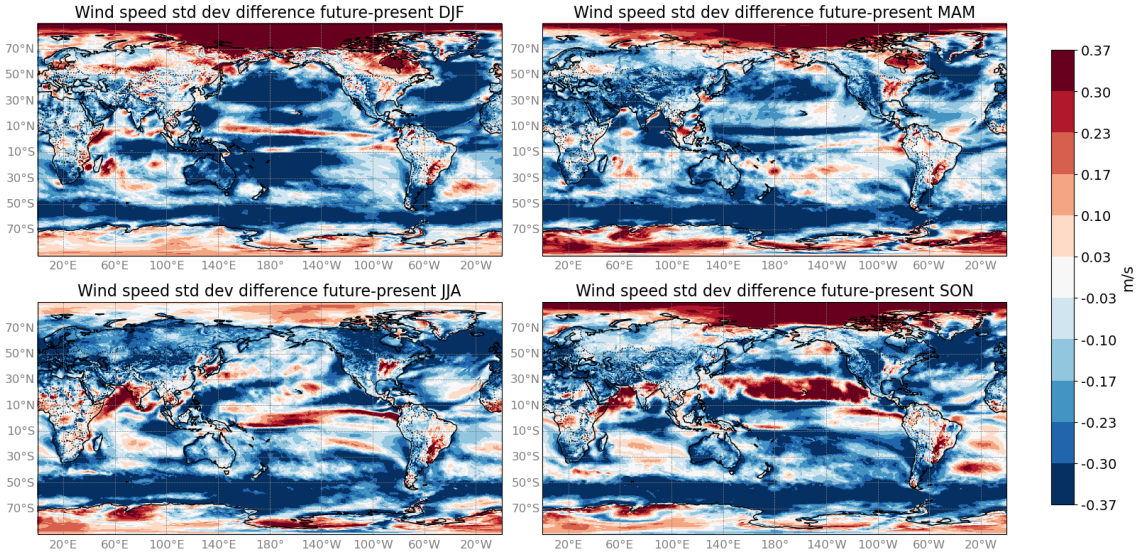

Figure 50: Difference of the standard deviation of the surface wind speed between the future and present temporal periods as simulated by the CMCC-CM3-LT model.

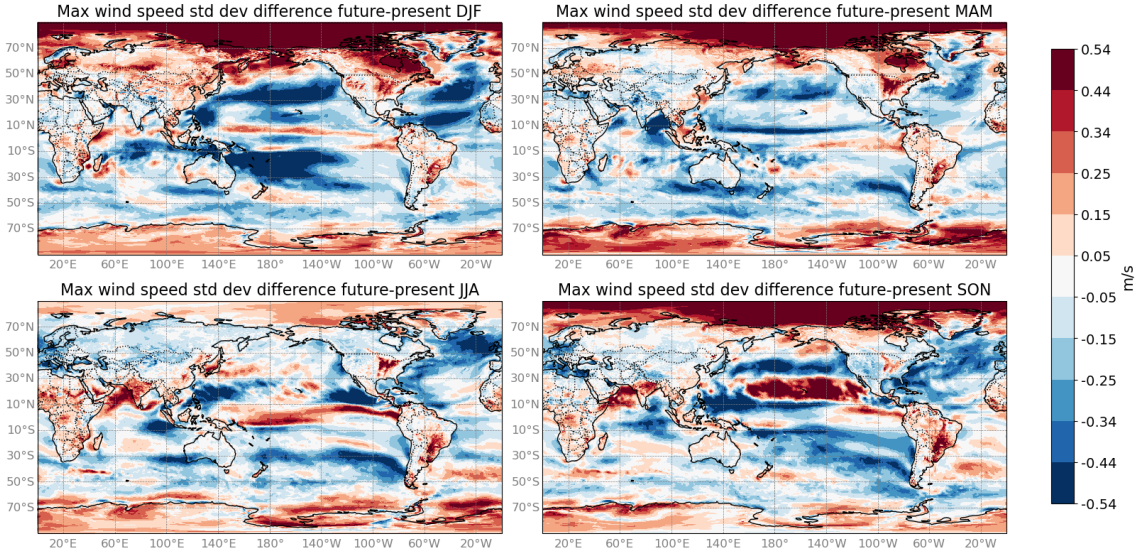

Figure 51: Difference of the standard deviation of the maximum surface wind speed every 6hr between the future and present temporal periods as simulated by the CMCC-CM3-LT model.

4.1 Projected changes in TC activity

After validating the tracking algorithm used through a comparison with the observational data collected in IBTrACS, and analyzing the comparison of the output on the reanalysis and climate simulation data on the present climate, in this section the future simulations are compared with the historical simulations to analyze the resulting change in TCs following the SSP5 scenario.

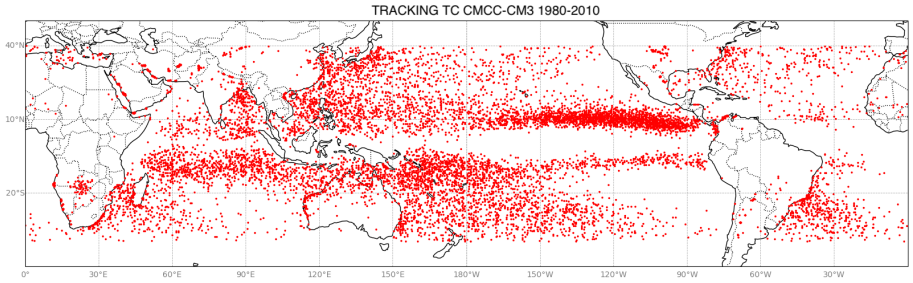

(a)

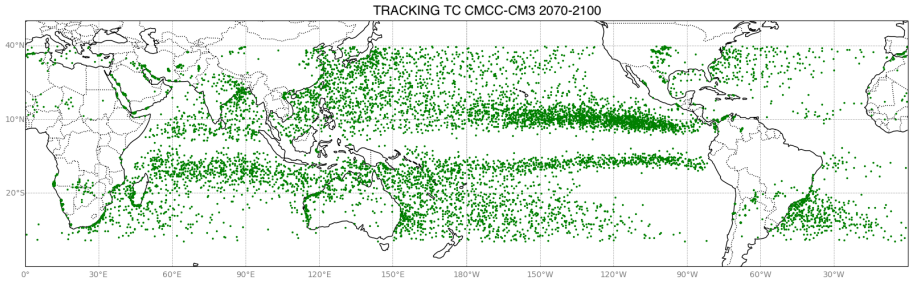

(b)

Figure 52: Initial points detected by CyTRACK using CMCC-CM3-LT simulation datasest of the present (a) and future climate (b).

The maps shown in figure 52 represent all the points of cyclonic genesis simulated by the CMCC-CM3-LS model in the two different periods. As noted in the figures 34, the spatial distribution of cyclones follows the trends described above, with areas of higher cyclonic activity in the past 30 years continue to stand out in future projections. However, as evidenced more clearly in the figures 53, there is a net decrease in the frequency of genesis in typically more active regions, such as the low latitudes of the Eastern North Pacific, the South Pacific, the Indian, and the Western Pacific Ocean. In parallel, there is a much softer increase in frequency of occurrences in areas where it was less frequent between 1980 and 2010, such as the central and Eastern North Pacific, the North Indian Ocean, and a strip immediately south of the equatorial line in the Eastern Pacific. Reddish colours also tend to prevail along the coasts, obviously the points most at risk.

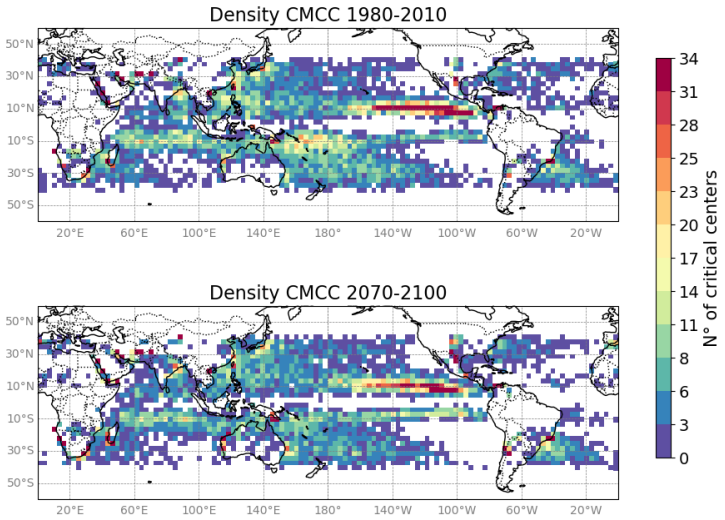

(a)

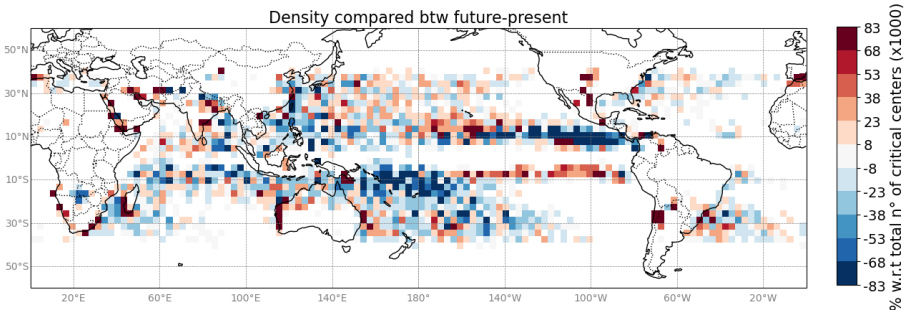

(b)

Figure 53: Density chart of initial points represented in figure 52 (a) and the difference between them (b), grouped in 3°x3° cells.

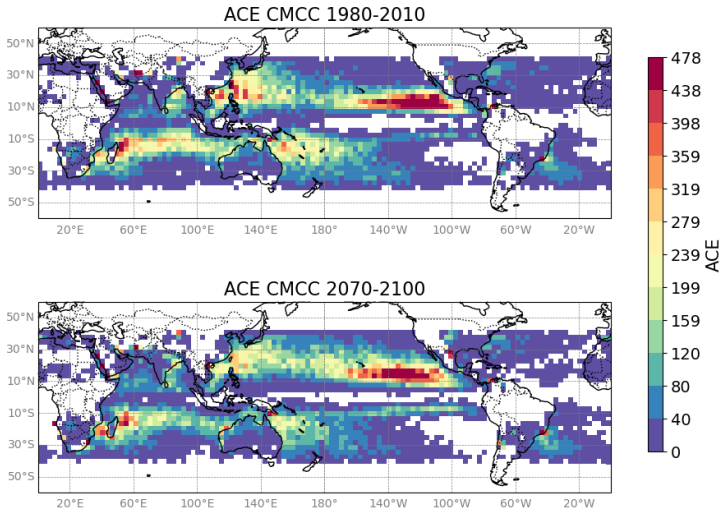

(a)

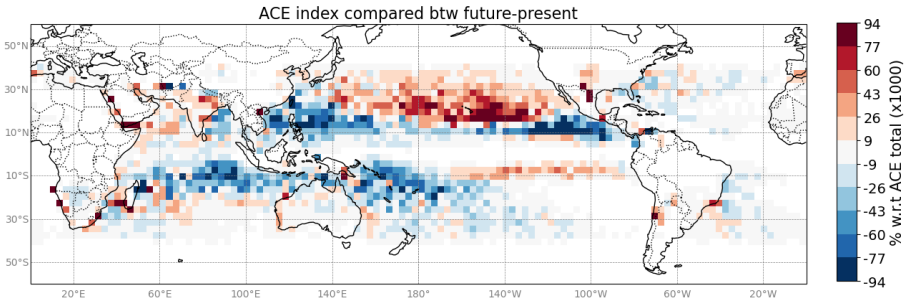

(b)

Figure 54: ACE index computed through the summation of the MSW square of all the points detected by CyTRACK in the future e present climate (a) and the difference between them (b). The values are scaled by a factor 10^4.

Similar behavior is observed for the ACE index (figure 54). The areas highlighted in red where the future index is higher than the index computed in the past 30 years largely coincide with the regions also identified in figure 53. Moreover, even where blue colours prevail, indicative of decreasing cyclonic activity, coastal areas characterized by positive values (reddish) are often noted, suggesting a possible increase in cyclonic intensity precisely near the most vulnerable areas. Figure 55 shows the MCP of cyclones detected by the model under current and future conditions, while figure 55b shows the difference between these minimum values, and figure 55c reports the change in mean central pressure. Consistent with previous results, the central and Eastern North Pacific show a decrease in both minimum and mean MCP values, while an increase in these values is observed in the Indian Ocean and Western Pacific low latitudes. In contrast, a more heterogeneous behavior is found in the North Indian Ocean, where, as visible in figure 55c, there is a marked decrease in mean central pressure in the southwestern domain of the ocean.

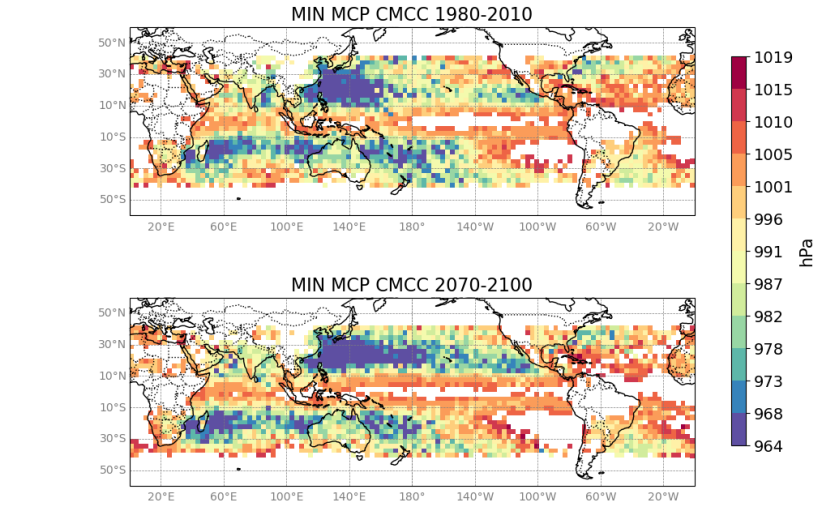

(a)

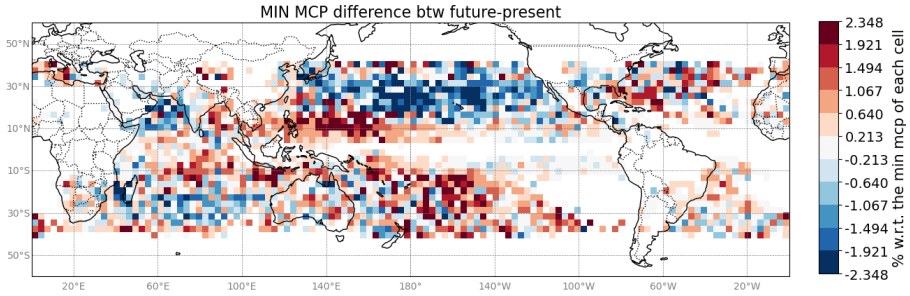

(b)

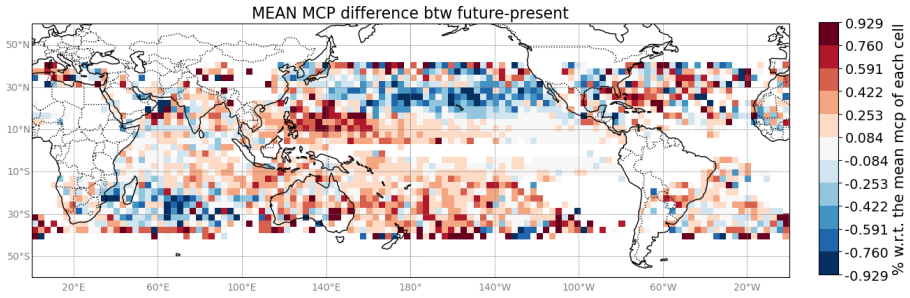

(c)

Figure 55: The three charts show the minimum values for each cell of the MCP found in the two temporal periods (a), their difference (b) and the comparison of the average values of the MCP computed in each cell (c).

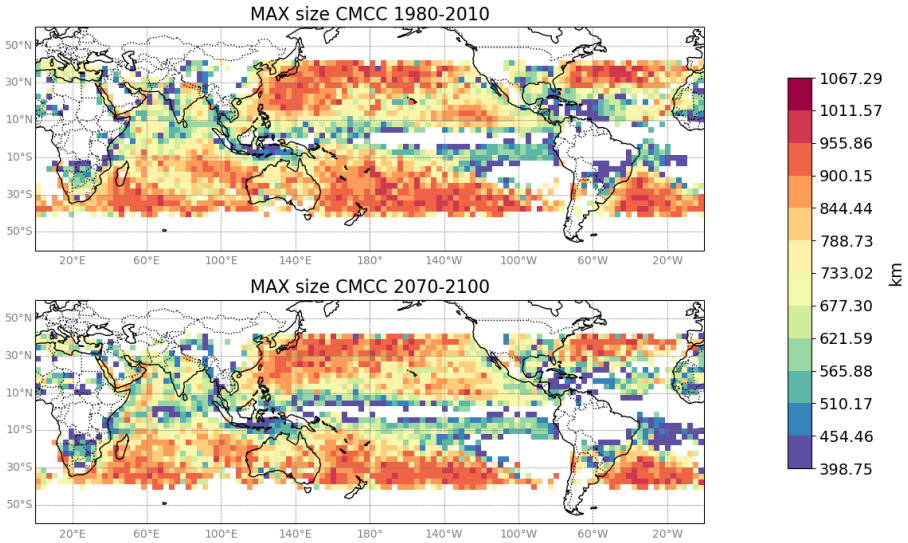

(a)

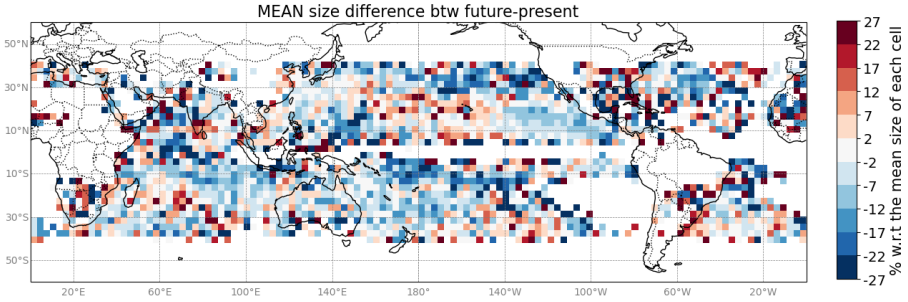

(b)

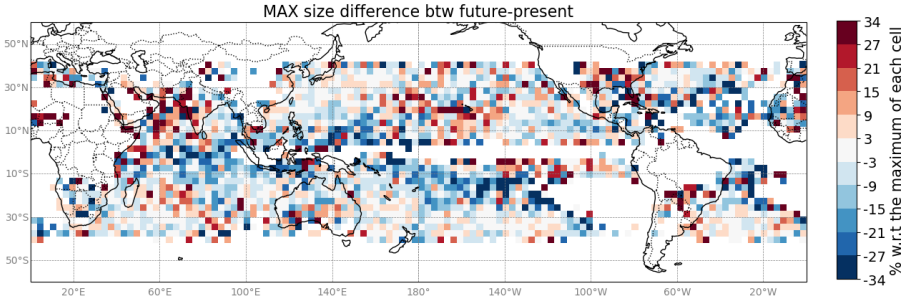

(c)

Figure 56

Regarding the TC size (figure 56), both mean and maximum, the trend near the coasts already observed with ACE is confirmed, where TCs are generally large in size. In general, the spatial distribution follows a pattern consistent with that of ACE and MCP, suggesting that greater cyclonic size is typically associated with greater intensity or density. However, some exceptions are noted, particularly in the Indian Ocean at low latitudes, where the behavior is more mixed, and in an upper stretch of the North Central Pacific where, despite other indices suggesting an increase in cyclonic activity, a decrease in size is observed. With respect to the other indices the areas where an increase in size is predicted seems less extended, while a global decreasing pattern is evident.
As anticipated, from the output of CyTRACK is obtained the value of the pressure at the outer isobar, which coincides with the pressure at ROCI. This data enables calculation of the pressure gradient between the PROCI and the MCP, a value that directly affects the intensity of the cyclone, with more intense winds occurring where the gradient is greater. It is therefore not surprising that the image 57, showing the difference in the pressure gradient between the future and the present tracking, follows a very similar pattern to that observed in figure 54b, relating to ACE. Again, the Central and Eastern North Pacific appear subject to a sharp increase in the pressure gradient, while the Atlantic Ocean appears colored mostly by blue, suggesting a weakening of future cyclonic activity in that region.

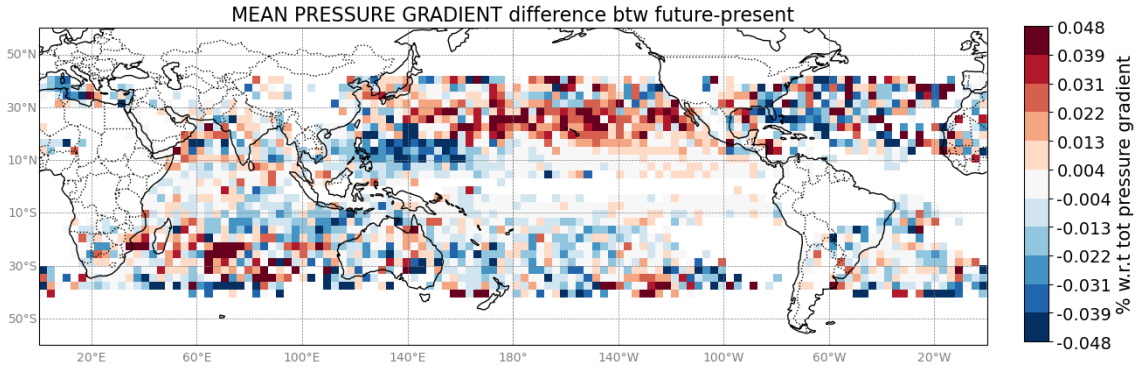

Figure 57: Comparison of the average baric gradient between the pressure of ROCI and the MCP computed for each cell as CyTRACK results of the present and future tracking.

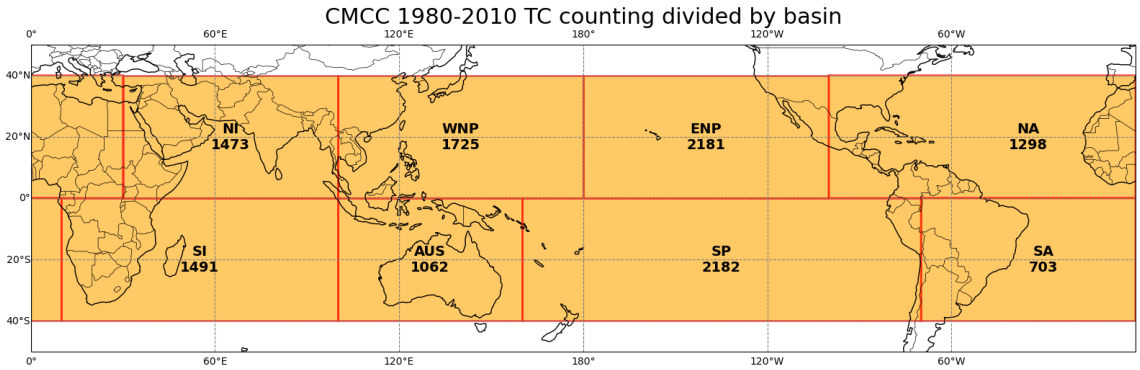

(a)

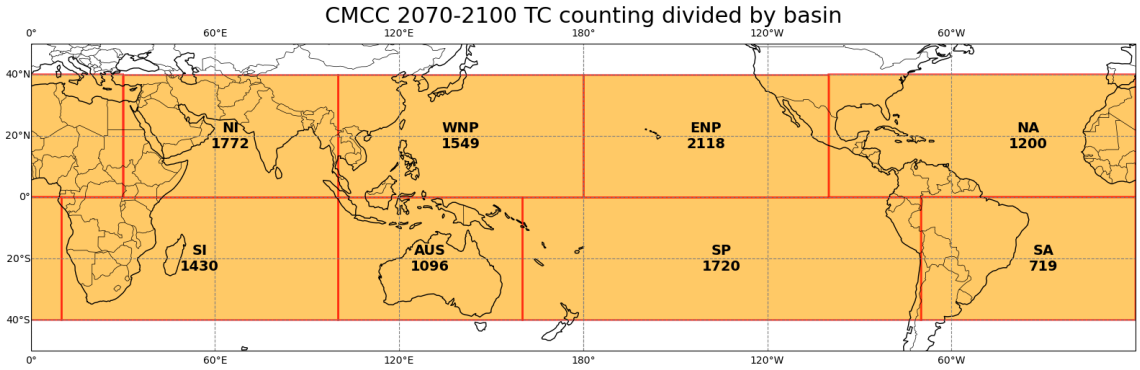

(b)

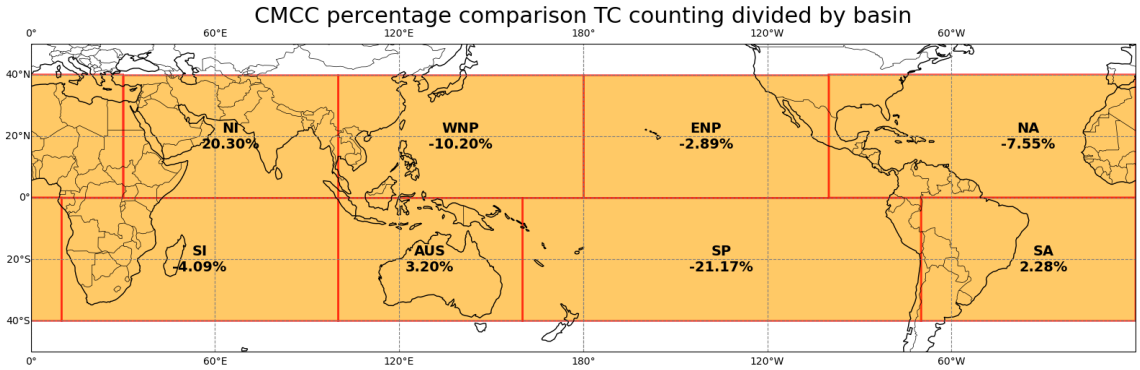

(c)

Figure 58: Number of initial points and changing rate represented in figure 52 divided by basin.

The figures 58 show the division of the analysed area into eight cyclonic basins: North Indian (NI), South Indian (SI), West North Pacific (WNP), East North Pacific (ENP), South Pacific (SP),

North Atlantic (NA) and South Atlantic (SA). The numbers displayed represent the centres of cyclonic origin detected in the different scenarios. The analysis shows that the only basin to show a net increase in cyclonic genesis is the North Indian Ocean (NI). In contrast, the West North Pacific (WNP) and South Pacific (SP) show a marked decrease in the number of cyclones generated. The North Atlantic (NA) also shows a reduction in the rate of cyclonic genesis in the future, while in the other basins (SI, SA, ENP) activity remains almost steady. Interestingly, although in the East North Pacific (ENP) basin other variables indicate an increase in cyclonic activity, the presence of a low-latitude zone near the coast of Mexico, where a significant reduction is expected, contributes to lowering the total number of events. This area, although geographically limited, has a significant weight as it is highly active.

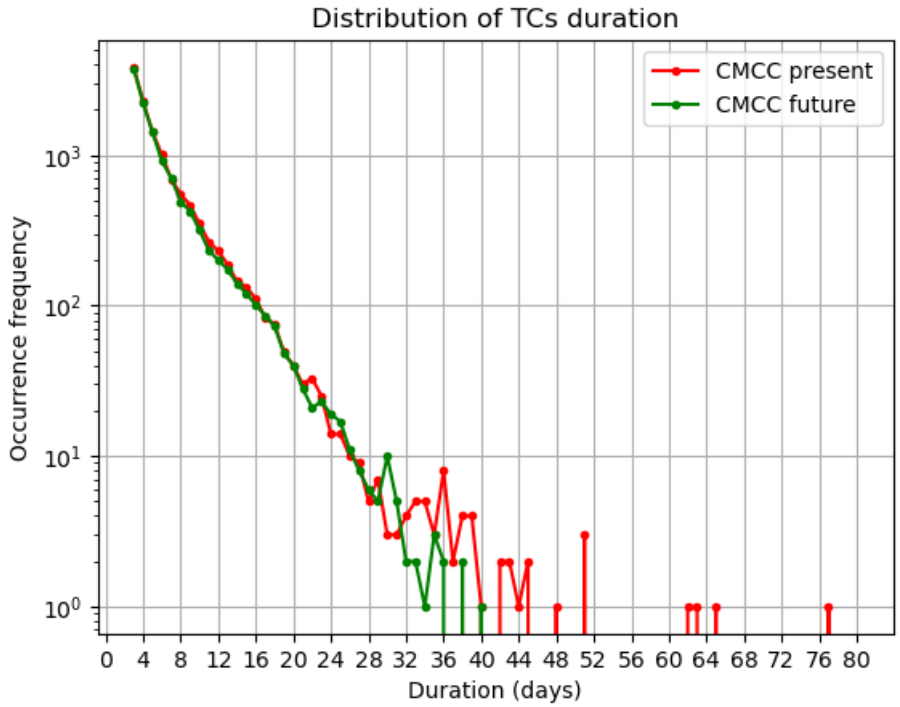

Figure 59: Graph in log-scale of the TCs timelife related to the number of TCs of the present (red line) and future climate (green line).

Interesting informations are provided by the comparison between the duration and frequency of past and future tropical cyclones (figure 59). The number of cyclones with short durations is, as expected, significantly higher than those with longer durations, showing a clear trend of exponential decrease. The differences between present and future become evident for cyclones with a duration of more than 30 days, which are significantly less frequent in the future scenario. Moreover, no future cyclone exceeds 40 days in duration, whereas in the present the last observed TC in terms of duration has a lifespan of 77 days.

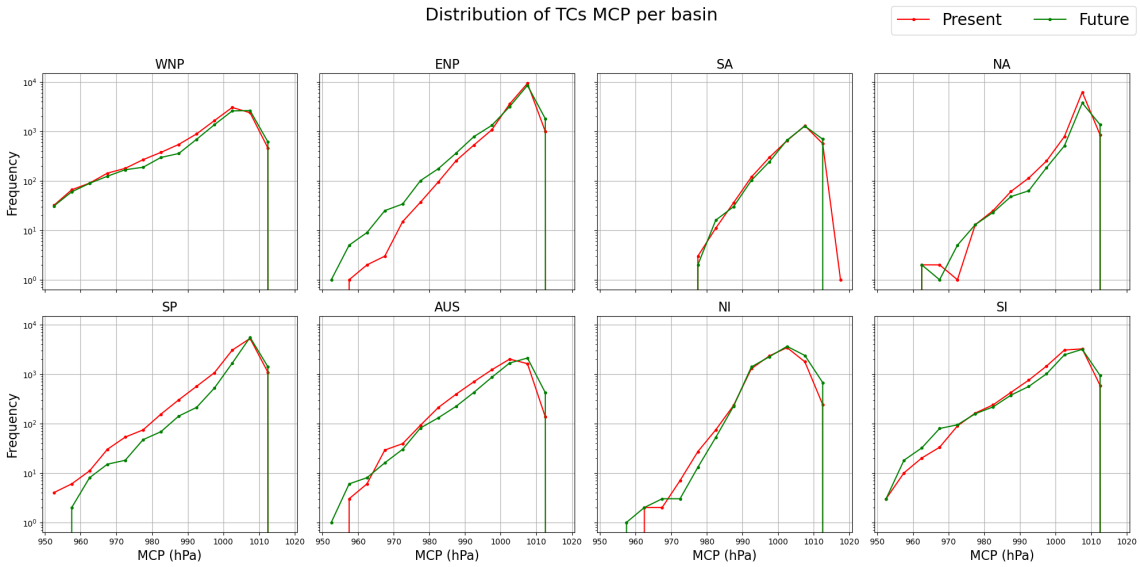

Figure 60: Graph in log-scale of the MCP distribution per basin related to the number of TCs of the present (red line) and future climate (green line).

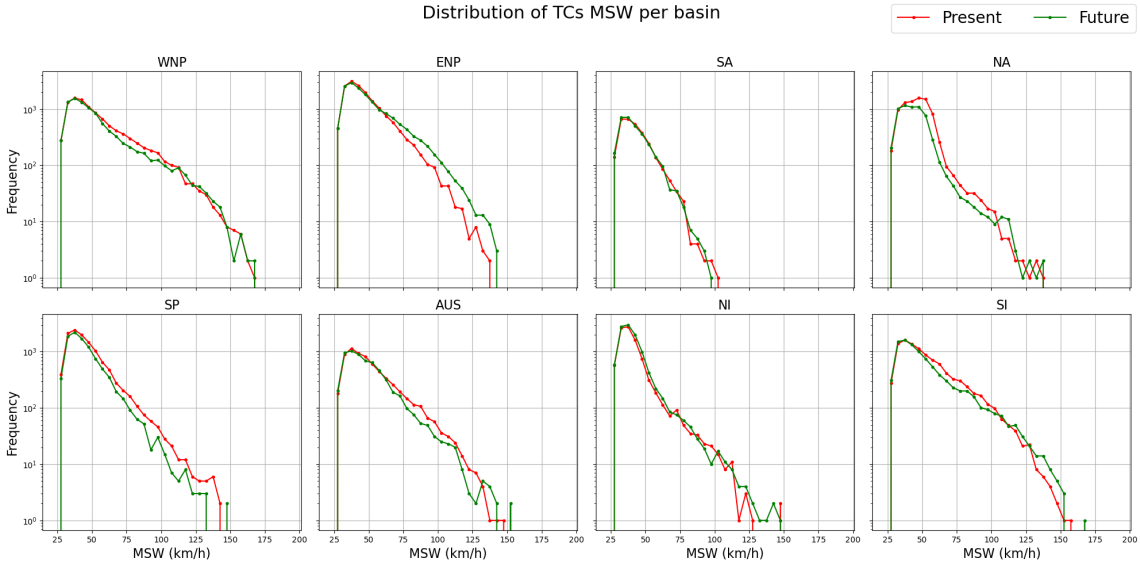

Figure 61: Graph in log-scale of the MSW distribution per basin related to the number of TCs of the present (red line) and future climate (green line).

The images 61 and 60 show that the basins where the previous images suggest increased cyclonic activity in terms of wind speed and MCP will be subject to higher frequencies of intense cyclones,

i.e. high MSW and low MCP. This is particularly noticeable in the ENP, NI, SI, and AUS basins, while the opposite occurs in SP. In SA, NA and WNP the trend is more heterogeneous or does not show clear differences between present and future. This therefore seems to be in line with the graph 59 suggesting that events are likely to be more intense and less frequent in the basins where activity seems to be increasing.

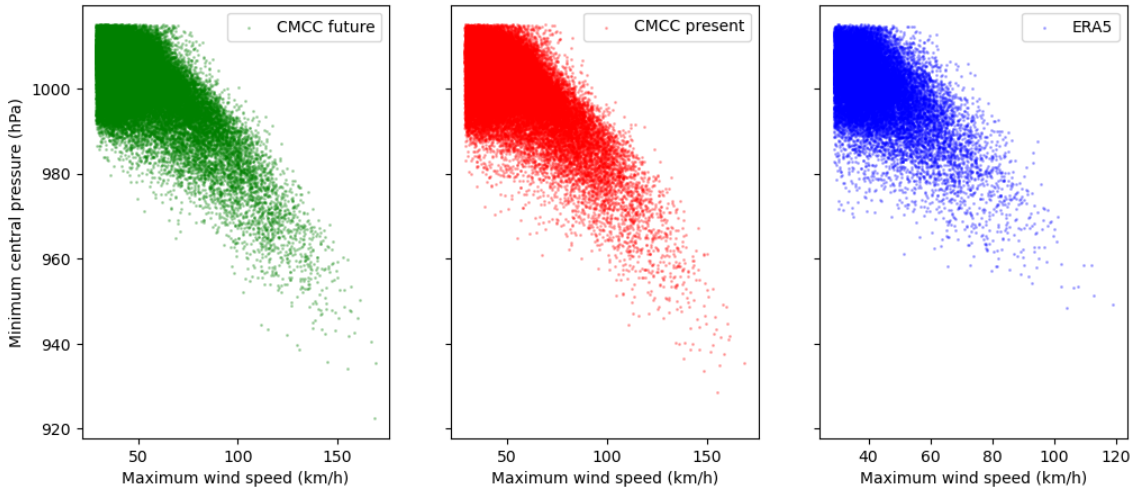

Figure 62: Graph showing the correlation between MSW and MCP of the TCs detected by CyTRACK across the three systems.

The correlation between MCP and maximum wind speed illustrated in the figure 62 is consistent with and acts as a proof of the opposite pattern obtained analyzing the ACE index and MCP values. Although the dispersion is high in areas with a high density of data, making it difficult to observe a clear relationship between the two variables, a more definite trend can be seen at the extreme values where low central pressures tend to be associated with higher maximum wind speeds. This shows an almost linear relationship under these conditions, confirming that cyclones with lower MCPs are generally associated with more intense winds.

4.2 Evaluation of TC changes in relationship with the large scale circulation

As seen in the previous section, the spatial pattern of the different derived TC parameters is recurrent. However, comparing the maps of cyclonic winds (figure 54), MCP (figure 55c) with the seasonal averages described before, some interesting behaviors emerge. Average precipitation seems to follow more closely the expected pattern of future cyclonic activity. Basins where cyclones are expected to increase, such as the North Indian Ocean and the Central and Eastern Pacific, indeed show an increase in rainfall, with the exception of the DJF and MAM periods in the Eastern Pacific (40). In contrast, the North Atlantic, South Atlantic and South Pacific oceans, where cyclonic activity is expected to decrease, show a corresponding decrease in rainfall. As for surface winds (48), with the exception of the Indian Ocean (where there is an increase in winds in MAM and

SON), the results are more heterogeneous and reflect the presence of extreme events that, being relatively rare (as shown in figure 59), do not significantly affect the seasonal average. For example, in the Central Pacific winds are expected to increase only in DJF and partially in SON, while in the Eastern Pacific a decrease is observed in all seasons. In the North and South Atlantic, the results are also discordant. In the North Atlantic a decreasing trend in cyclonic winds is confirmed by the mean climate, while in the South Atlantic mean winds seem to increase. Finally, with regard to the change in mean sea level pressure (figure 42), there are seasonal trends consistent with cyclone projections (figure 55c). In particular, in the North Indian Ocean, a decrease in MSLP is confirmed in DJF and SON, and in the South Indian Ocean in DJF and MAM. The Central and Eastern Pacific show a decrease in MSLP in JJA and SON, while in the South Pacific and Atlantic Ocean there is an upward trend in mean MSLP values, in line with the decrease in cyclonic activity.
The predicted increase in mean temperatures at 500 hPa and 300 hPa is in line with IPCC ([52]) predictions, according to which the increase in temperatures is linked to an increase in peak wind speeds and an intensification of tropical cyclones. The same increase in TC intensity suggested by the graph 59 along with a decrease in frequency.

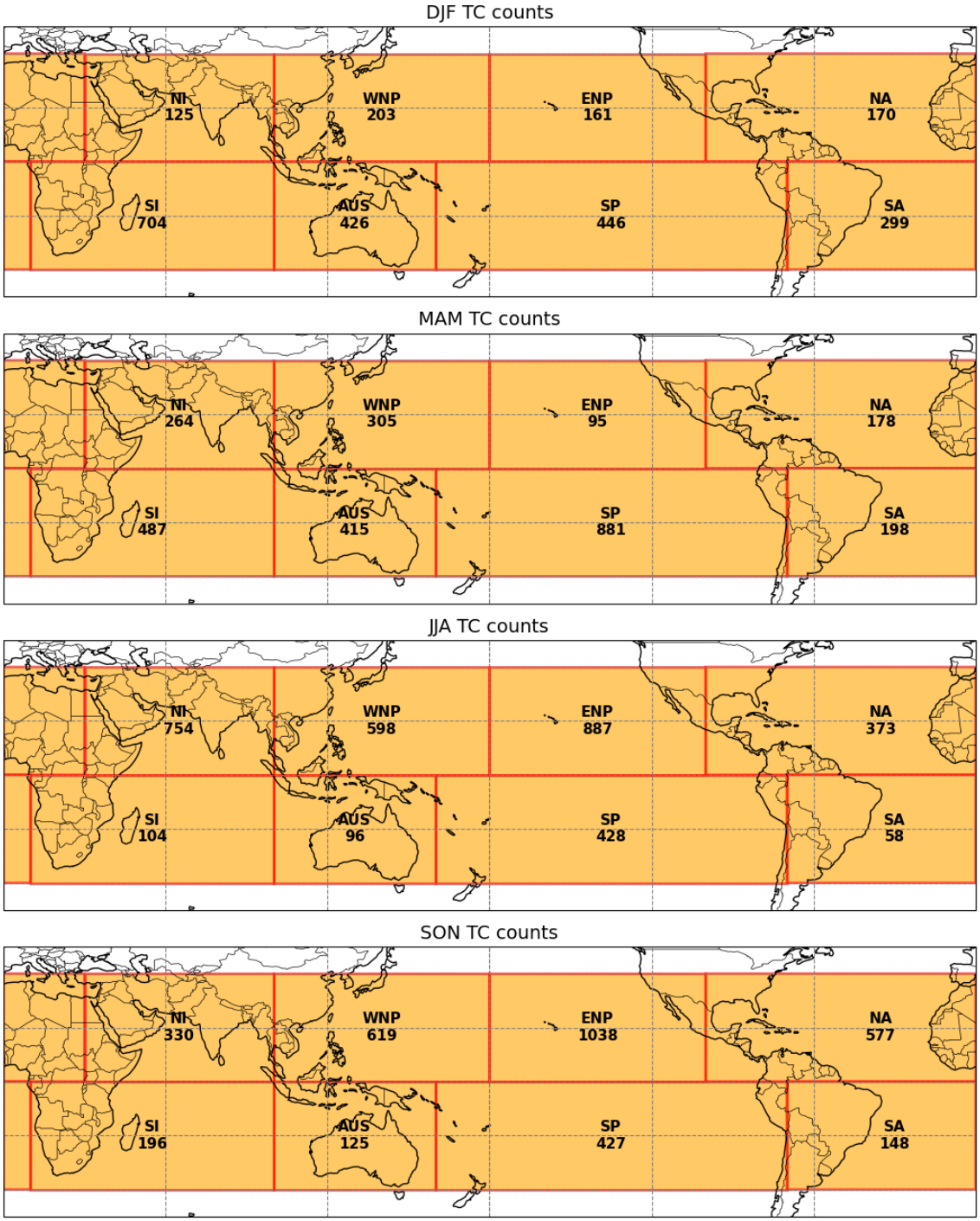

Figure 63: Charts showing the genesis of TCs during the past 30 years analyzed divided by basins and seasons, using the CMCC-CM3-LT model.

In order to better clarify the relationship between changes in mean climate and changes in future cyclonic activity, two significance tests were conducted. One is Pearson's test, which assesses the presence of a linear relationship between the variables, while the second, Spearman's test, analyses the possible monotonicity of the relationship. The tables below show the values of the correlation coefficients obtained with both methods, accompanied by their respective p-values, with a division by season and hemisphere. As also shown in the figure 63, cyclonic activity is more pronounced in the northern hemisphere during the JJA and SON seasons, while in the southern hemisphere it is more relevant during MAM and DJF. In this sense, the tables highlight the values of greatest interest in the seasons in which cyclonic activity is particularly relevant. Statistically significant correlations are present in most of the cases highlighted, with two exceptions in particular. Indeed, the relationship between MCP and temperature at 300 hPa during the JJA season shows excessively high p-values in both statistical tests, as does the relationship between MCP and precipitation in DJF. However, a consistency in the sign of the correlations is observed in the terms of interest, with the r coefficient positive ACE and negative for MCP.

Table 3: Spearman and Pearson correlation between change in mean ACE and MCP vs ta300

	Variables	**r (Spearman)**	**p (Spearman)**	**r (Pearson)**	**p (Pearson)**
NH	**ACE vs ta300 (JJA)**	**0.379**	**0.0000**	**0.050**	**0.3116**
	ACE vs ta300 (MAM)	-0.439	0.0000	-0.138	0.0070
	ACE vs ta300 (SON)	**0.535**	**0.0000**	**0.412**	**0.0000**
	ACE vs ta300 (DJF)	-0.025	0.5769	-0.011	0.8106
	MCP vs ta300 (JJA)	**-0.042**	**0.2776**	**-0.009**	**0.8210**
	MCP vs ta300 (MAM)	0.024	0.6488	-0.007	0.9008
	MCP vs ta300 (SON)	**-0.292**	**0.0000**	**-0.228**	**0.0000**
	MCP vs ta300 (DJF)	-0.140	0.0019	-0.013	0.7735
SH	ACE vs ta300 (JJA)	-0.126	0.0080	0.077	0.1062
	ACE vs ta300 (MAM)	**0.063**	**0.0763**	**0.064**	**0.0717**
	ACE vs ta300 (SON)	-0.015	0.7462	0.056	0.2080
	ACE vs ta300 (DJF)	**0.290**	**0.0000**	**0.246**	**0.0000**
	MCP vs ta300 (JJA)	-0.038	0.4335	-0.014	0.7807
	MCP vs ta300 (MAM)	**-0.124**	**0.0001**	**-0.134**	**0.0000**
	MCP vs ta300 (SON)	-0.160	0.0008	-0.108	0.0235
	MCP vs ta300 (DJF)	**-0.347**	**0.0000**	**-0.285**	**0.0000**

Table 4: Spearman and Pearson correlation between change in mean ACE and MCP vs ta500

	Variables	r (Spearman)	p (Spearman)	r (Pearson)	p (Pearson)
NH	**ACE vs ta500 (JJA)**	**0.239**	**0.0000**	**0.099**	**0.0429**
	ACE vs ta500 (MAM)	0.321	0.0000	0.143	0.0051
	ACE vs ta500 (SON)	**0.456**	**0.0000**	**0.329**	**0.0000**
	ACE vs ta500 (DJF)	0.157	0.0005	0.063	0.1680
	MCP vs ta500 (JJA)	**-0.287**	**0.0000**	**-0.198**	**0.0000**
	MCP vs ta500 (MAM)	-0.088	0.0977	-0.044	0.4113
	MCP vs ta500 (SON)	**-0.185**	**0.0000**	**-0.119**	**0.0003**
	MCP vs ta500 (DJF)	-0.155	0.0006	-0.032	0.4821
SH	ACE vs ta500 (JJA)	-0.216	0.0000	0.014	0.7729
	ACE vs ta500 (MAM)	**0.051**	**0.1550**	**0.047**	**0.1822**
	ACE vs ta500 (SON)	0.197	0.0000	0.147	0.0010
	ACE vs ta500 (DJF)	**0.398**	**0.0000**	**0.200**	**0.0000**
	MCP vs ta500 (JJA)	-0.107	0.0285	-0.043	0.3735
	MCP vs ta500 (MAM)	**-0.084**	**0.0096**	**-0.084**	**0.0097**
	MCP vs ta500 (SON)	-0.158	0.0009	-0.113	0.0179
	MCP vs ta500 (DJF)	**-0.248**	**0.0000**	**-0.249**	**0.0000**

Table 5: Spearman and Pearson correlation between change in mean ACE and MCP vs precipitation rate

	Variables	r (Spearman)	p (Spearman)	r (Pearson)	p (Pearson)
NH	**ACE vs pr (JJA)**	**0.414**	**0.0000**	**0.129**	**0.0086**
	ACE vs pr (MAM)	0.423	0.0000	0.222	0.0000
	ACE vs pr (SON)	**0.302**	**0.0000**	**0.088**	**0.0332**
	ACE vs pr (DJF)	0.138	0.0023	0.129	0.0043
	MCP vs pr (JJA)	**-0.085**	**0.0279**	**-0.050**	**0.2009**
	MCP vs pr (MAM)	-0.055	0.2986	-0.053	0.3145
	MCP vs pr (SON)	**-0.215**	**0.0000**	**-0.140**	**0.0000**
	MCP vs pr (DJF)	-0.012	0.7894	-0.044	0.3360
SH	ACE vs pr (JJA)	0.046	0.3365	0.033	0.4846
	ACE vs pr (MAM)	**0.260**	**0.0000**	**0.164**	**0.0000**
	ACE vs pr (SON)	0.185	0.0000	0.068	0.1310
	ACE vs pr (DJF)	**0.339**	**0.0000**	**0.311**	**0.0000**
	MCP vs pr (JJA)	0.014	0.7742	0.002	0.9603
	MCP vs pr (MAM)	**-0.185**	**0.0000**	**-0.097**	**0.0028**
	MCP vs pr (SON)	0.013	0.7828	0.048	0.3176
	MCP vs pr (DJF)	**-0.006**	**0.8651**	**-0.029**	**0.4150**

5 Summary and Conclusions

Several variables of the climate system have been analyzed in this study, focusing in particular on tropical cyclones, one of the extreme events that most affect our planet. The main objective was to evaluate the future evolution of these phenomena using data produced by the CMCC-CM3-LT climate model. After an initial comparison with observational satellite data and reanalysis data, it became possible to examine trends in variables directly or indirectly related to tropical cyclone activity, such as precipitation, sea surface temperature, surface winds, and sea-level pressure. In particular, wind and pressure fields were key inputs to the CyTRACK tracking algorithm, allowing simulations to be validated by comparing them with both observations in the IBTrACS database and results from reanalysis. Once the reliability of the model and tracking algorithm was established, for the future SSP5 scenario the projections presented in this thesis can be considered reliable for the 30-year period 2070-2100. The analysis shows that regions with the most intense cyclonic activity in the present climate, such as low latitudes in the Eastern and Western North Pacific and South Pacific, seem to move toward a decrease in activity. In contrast, areas with more moderate but still significant activity, such as the Central and Eastern Pacific and the North Indian Ocean, show an increase in indices such as the baric gradient and ACE and a decrease in mean MCP, indicating a potential intensification of cyclones. An interesting aspect concerns the temporal distribution of cyclone duration. Indeed, future and present simulations return a similar number of events with durations of less than 30 days, while occurrences of cyclones of very high durations, present in the present climate, tend to disappear. Thus, in line with several studies ([53], [54]) and the IPCC forecast of an increase in extreme events ([52]), this suggests a higher intensity of cyclones in the future, but with a general lower frequency and a slight reduction in activity in areas currently most affected by these extreme events. However, it is important to consider the inherent limitations of the study. The results obtained are indeed strongly influenced by both the tracker employed and the climate model used. A systematic comparison of different tracking algorithms and climate models would be helpful in order to ensure more robustness and reliability of the conclusions. In addition, the tracking algorithm was only applied to the surface component, as geopotential data, which are necessary for the vertical analysis of the cyclone structure, were not provided as inputs. Although this analysis is optional in the operation of the tracker and not strictly necessary for the identification of cyclones, its inclusion could have contributed to a more complete characterisation of cyclone systems.

A Tables

Table 6: Description of Dataset downloaded from ESGF: Precipitation (pr)

File Name	`pr_GPCP-SG_L3_v2.3_197901-201710.nc`
Time Range	1979-01-01 12:00:00 to 2017-10-01 12:00:00
Frequency	Monthly
Resolution	1.25-degree grid
Variable	Precipitation flux (Kg m^{-2} s^{-1})
Data Node	`dpesgf03.nccs.nasa.gov`
Index Node	`esgf-node.llnl.gov`
Model	Obs-GPCP
Institute	NASA-GSFC
Source ID	GPCP-V2.3
Size	19,348,352 bytes
Product	Observations
Project	obs4MIPs

Table 7: Description of Dataset downloaded from ESGF: Sea Surface Temperature (tos)

File Name	`tos_mon_ESA-CCI-SST-v2-1_BE_gn_198109-201712.nc`
Time Range	1981-09-01 00:00:00 to 2017-12-31 12:00:00
Frequency	Monthly
Variable	Sea Surface Temperature (degC)
Data Node	`esgf.ceda.ac.uk`
Index Node	`esgf.ceda.ac.uk`
Institution	University of Reading, Reading, U.K.
Resolution	Nominal 100 km
Source ID	ESA-CCI-SST-v2-1
Source Type	Satellite retrieval
Source Version	v2.1
Activity ID	obs4MIPs
Grid Label	native grid
Size	43,679,218 bytes

Table 8: Description of Dataset downloaded from ESGF: Eastward Near-Surface Wind (uas)

File Name	`uas_mon_QuikSCAT-v20110531_BE_gn_199908-200910.nc`
Time Range	1999-08-01 12:00:00 to 2009-10-31 12:00:00
Frequency	Monthly
Variable	Eastward Near-Surface Wind (m s^{-1})
Data Node	`aims3.llnl.gov`
Index Node	`esgf-node.llnl.gov`
Institution ID	NASA-JPL
Resolution	1x1 degree
Source ID	QuikSCAT-v20110531
Source Type	Satellite retrieval
Source Version	v20110531
Activity ID	obs4MIPs
Grid Label	native grid
Size	31,906,596 bytes

Table 9: Description of Dataset downloaded from ESGF : Northward Near-Surface Wind (vas)

File Name	`vas_mon_QuikSCAT-v20110531_BE_gn_199908-200910.nc`
Time Range	1999-08-01 12:00:00 to 2009-10-31 12:00:00
Frequency	Monthly
Resolution	1x1 degree
Variable	Northward Near-Surface Wind (m s^{-1})
Data Node	`aims3.llnl.gov`
Index Node	`esgf-node.llnl.gov`
Institution	NASA-JPL
Source ID	QuikSCAT-v20110531
Source Type	Satellite Retrieval
Source Version	v20110531
Activity ID	obs4MIPs
Grid Label	`native grid`
Size	31,906,596 bytes

Table 10: Description of simulation datasets derived from CMCC-CM3-LT

Time Range	1975-01-01 00:00:00 to 2014-12-31 18:00:00
Frequency	6 hr - daily
Variables	Surface wind, Wind at 850 hPa, MSLP, Precipitation rate, Air temperature (300 hPa, 500 hPa)
Model doi url	`https://doi.org/10.5065/D67H1H0V`
Grid Type	768 x 1152 (lat x lon)
Model	CMCC-CM3-LT
Atm component	CAM 6
Land component	CLM 5
Ice component	CICE 5
Ocean component	NEMO 4.0.5
Conventions	CF-1.0 (Climate and Forecast)
CDO	Climate Data Operators version 2.1.1

References

[1] United Nations Framework Convention on Climate Change. United nations framework convention on climate change. `https://unfccc.int/resource/docs/convkp/conveng.pdf`, 1992.

[2] IPCC. Climate change 2023: Synthesis report, 2023. Contribution of Working Groups I, II and III to the Sixth Assessment Report of the Intergovernmental Panel on Climate Change.

[3] S. Planton. Annex iii: Glossary. In T.F. Stocker, D. Qin, G.-K. Plattner, M. Tignor, S.K. Allen, J. Boschung, A. Nauels, Y. Xia, V. Bex, and P.M. Midgley, editors, *Climate Change 2013: The Physical Science Basis. Contribution of Working Group I to the Fifth Assessment Report of the Intergovernmental Panel on Climate Change*. Cambridge University Press, Cambridge, United Kingdom and New York, NY, USA, 2013.

[4] Richard B. Rood Andrew Gettelman. *Demystifying Climate Models*. Springer Berlin, Heidelberg, 2016.

[5] H. Le Treut, R. Somerville, U. Cubasch, Y. Ding, C. Mauritzen, A. Mokssit, T. Peterson, and M. Prather. Historical overview of climate change, 2007.

[6] J. T. Kiehl and Kevin E. Trenberth. Earth's annual global mean energy budget. *Bulletin of the American Meteorological Society*, 78(2):197 – 208, 1997.

[7] M. Oppenheimer, M. Campos, R. Warren, J. Birkmann, G. Luber, B. O'Neill, and K. Takahashi. Emergent risks and key vulnerabilities. In C.B. Field, V.R. Barros, D.J. Dokken, K.J. Mach, M.D. Mastrandrea, T.E. Bilir, M. Chatterjee, K.L. Ebi, Y.O. Estrada, R.C. Genova, B. Girma, E.S. Kissel, A.N. Levy, S. MacCracken, P.R. Mastrandrea, and L.L. White, editors, *Climate Change 2014: Impacts, Adaptation, and Vulnerability. Part A: Global and Sectoral Aspects*, pages 1039–1099. Cambridge University Press, Cambridge, United Kingdom and New York, NY, USA, 2014. Contribution of Working Group II to the Fifth Assessment Report of the Intergovernmental Panel on Climate Change.

[8] World Meteorological Organization. Characteristics of tropical cyclones. https://public.wmo.int/content/characteristics-of-tropical-cyclones, 2023.

[9] Haiyan Jiang and Edward J. Zipser. Contribution of tropical cyclones to the global precipitation from eight seasons of trmm data: Regional, seasonal, and interannual variations. *Journal of Climate*, 23(6):1526 – 1543, 2010.

[10] Shumin Chen and Weibiao Li. A review of typhoon inner core characteristics and their relationship with intensity changes. *Atmosphere*, 15(12):1522, 2024.

[11] Liguang Wu, Haikun Zhao, Chao Wang, Jian Cao, and Jia Liang. Understanding of the effect of climate change on tropical cyclone intensity: A review. *Advances in Atmospheric Sciences*, 2022.

[12] Yuqing Wang and Chun-Chieh Wu. Current understanding of tropical cyclone structure and intensity changes - a review. *Meteorol. Atmos. Phys.*, 87:257–278, 12 2004.

[13] Gabriele Villarini and Gabriel A. Vecchi. Projected increases in north atlantic tropical cyclone intensity from cmip5 models. *Journal of Climate*, 26(10):3231 – 3240, 2013.

[14] Keywan Riahi, Detlef P. van Vuuren, Elmar Kriegler, Jae Edmonds, Brian C. O'Neill, Shinichiro Fujimori, Nico Bauer, Katherine Calvin, Rob Dellink, Oliver Fricko, Wolfgang Lutz, Alexander Popp, Jesus Crespo Cuaresma, Samir KC, Marian Leimbach, Leiwen Jiang, Tom Kram, Shilpa Rao, Johannes Emmerling, Kristie Ebi, Tomoko Hasegawa, Petr Havlik, Florian Humpenöder, Lara Aleluia Da Silva, Steve Smith, Elke Stehfest, Valentina Bosetti, Jiyong Eom, David Gernaat, Toshihiko Masui, Joeri Rogelj, Jessica Strefler, Laurent Drouet, Volker Krey, Gunnar Luderer, Mathijs Harmsen, Kiyoshi Takahashi, Lavinia Baumstark, Jonathan C. Doelman, Mikiko Kainuma, Zbigniew Klimont, Giacomo Marangoni, Hermann Lotze-Campen, Michael Obersteiner, Andrzej Tabeau, and Massimo Tavoni. The shared socioeconomic pathways and their energy, land use, and greenhouse gas emissions implications: An overview. *Global Environmental Change*, 42:153–168, 2017.

[15] George J Huffman, Robert F Adler, Philip Arkin, Alfred Chang, Ralph Ferraro, Arnold Gruber, John Janowiak, Alan McNab, Bruno Rudolf, and Udo Schneider. The global precipitation climatology project (gpcp) combined precipitation dataset. *Bulletin of the american meteorological society*, 78(1):5–20, 1997.

[16] Long S. Chiu and Roongroj Chokngamwong. Microwave emission brightness temperature histograms (meth) rain rates for climate studies: Remote sensing systems ssm/i version-6 results. *Journal of Applied Meteorology and Climatology*, 49(1):115 – 123, 2010.

[17] Udo Schneider, Andreas Becker, Peter Finger, Anja Meyer-Christoffer, Bruno Rudolf, and Markus Ziese. Gpcc full data reanalysis version 7.0: Monthly land-surface precipitation from rain gauges built on gts based and historic data, 2016.

[18] Robert F Adler, Mathew RP Sapiano, George J Huffman, Jian-Jian Wang, Guojun Gu, David Bolvin, Long Chiu, Udo Schneider, Andreas Becker, Eric Nelkin, et al. The global precipitation climatology project (gpcp) monthly analysis (new version 2.3) and a review of 2017 global precipitation. *Atmosphere*, 9(4):138, 2018.

[19] D. Waliser, P. J. Gleckler, R. Ferraro, K. E. Taylor, S. Ames, J. Biard, M. G. Bosilovich, O. Brown, H. Chepfer, L. Cinquini, P. J. Durack, V. Eyring, P.-P. Mathieu, T. Lee, S. Pinnock, G. L. Potter, M. Rixen, R. Saunders, J. Schulz, J.-N. Thépaut, and M. Tuma. Observations for model intercomparison project (obs4mips): status for cmip6. *Geoscientific Model Development*, 13(7):2945–2958, 2020.

[20] Hans Hersbach, Bill Bell, Paul Berrisford, Shoji Hirahara, András Horányi, Joaquín Muñoz-Sabater, Julien Nicolas, Carole Peubey, Raluca Radu, Dinand Schepers, Adrian Simmons, Cornel Soci, Saleh Abdalla, Xavier Abellan, Gianpaolo Balsamo, Peter Bechtold, Gionata Biavati, Jean Bidlot, Massimo Bonavita, Giovanna De Chiara, Per Dahlgren, Dick Dee, Michail Diamantakis, Rossana Dragani, Johannes Flemming, Richard Forbes, Manuel Fuentes, Alan Geer, Leo Haimberger, Sean Healy, Robin J. Hogan, Elías Hólm, Marta Janisková, Sarah Keeley, Patrick Laloyaux, Philippe Lopez, Cristina Lupu, Gabor Radnoti, Patricia de Rosnay, Iryna Rozum, Freja Vamborg, Sebastien Villaume, and Jean-Noël Thépaut. The era5 global reanalysis. *Quarterly Journal of the Royal Meteorological Society*, 146(730):1999–2049, 2020.

[21] J Scott Armstrong (University of Pennsylvania) Kesten Green (International Graduate School of Business University of South Australia) Nongovernmental International Panel on Climate Change (NIPCC) Anthony Lupo (University of Missouri), William Kininmonth (Australian Climate Science Coalition). Global climate models and their limitations, 2013.

[22] V. Eyring, S. Bony, G. A. Meehl, C. A. Senior, B. Stevens, R. J. Stouffer, and K. E. Taylor. Overview of the coupled model intercomparison project phase 6 (cmip6) experimental design and organization. *Geoscientific Model Development*, 9(5):1937–1958, 2016.

[23] Albert Martínez-Botí, Lorenzo Sangelantoni, Riccardo Henin, Daniele Peano, and Enrico Scoccimarro. Report on climate change scenarios in coastal zones of europe (d2.3). Technical Report Deliverable D2.3, BlueAdapt Project (Action No. 101057764), CMCC, September 2024. Work Package 2: Development of Conceptual Framework: Trends and Horizon Scanning. Final version, Revision 1. Dissemination Level: Public. Submitted 30 September 2024.

[24] Peter H Lauritzen, Andrew J Conley, Douglas E Kinnison, Anne K Smith, Francis M Vitt, and Rolando R García. Description of the ncar community atmosphere model (cam 5.0). *Description of the NCAR Community Atmosphere Model (CAM 5.0)(2012) NCAR/TN-486+ STR*, 486, 2012.

[25] Gokhan Danabasoglu, J-F Lamarque, J Bacmeister, DA Bailey, AK DuVivier, Jim Edwards, LK Emmons, John Fasullo, R Garcia, Andrew Gettelman, et al. The community earth system model version 2 (cesm2). *Journal of Advances in Modeling Earth Systems*, 12(2):e2019MS001916, 2020.

[26] Christopher S. Bretherton and Sungsu Park. A new moist turbulence parameterization in the community atmosphere model. *Journal of Climate*, 22(12):3422 – 3448, 2009.

[27] A. Gettelman, H. Morrison, and S. J. Ghan. A new two-moment bulk stratiform cloud microphysics scheme in the community atmosphere model, version 3 (cam3). part ii: Single-column and global results. *Journal of Climate*, 21(15):3660 – 3679, 2008.

[28] Hayder Abdul-Razzak and Steven J. Ghan. A parameterization of aerosol activation: 2. multiple aerosol types. *Journal of Geophysical Research: Atmospheres*, 105(D5):6837–6844, 2000.

[29] A. Gettelman and H. Morrison. Advanced two-moment bulk microphysics for global models. part i: Off-line tests and comparison with other schemes. *Journal of Climate*, 28(3):1268 – 1287, 2015.

[30] Michael J. Iacono, Jennifer S. Delamere, Eli J. Mlawer, Mark W. Shephard, Shepard A. Clough, and William D. Collins. Radiative forcing by long-lived greenhouse gases: Calculations with the aer radiative transfer models. *Journal of Geophysical Research: Atmospheres*, 113(D13), 2008.

[31] Jean-Christophe Golaz, Vincent E Larson, and William R Cotton. A pdf-based model for boundary layer clouds. part i: Method and model description. *Journal of the atmospheric sciences*, 59(24):3540–3551, 2002.

[32] Shian-Jiann Lin and Richard B. Rood. Multidimensional flux-form semi-lagrangian transport schemes. *Monthly Weather Review*, 124(9):2046 – 2070, 1996.

[33] Gurvan Madec et al. Nemo ocean engine, 2015.

[34] Gurvan Madec and Maurice Imbard. A global ocean mesh to overcome the north pole singularity. *Climate Dynamics*, 12:381–388, 05 1996.

[35] Bruno Blanke and Pascale Delecluse. Variability of the tropical atlantic ocean simulated by a general circulation model with two different mixed-layer physics. *Journal of Physical Oceanography*, 23(7):1363 – 1388, 1993.

[36] Elizabeth Hunke and W. Lipscomb. Cice: The los alamos sea ice model documentation and software user's manual version 4.0 la-cc-06-012. *Tech. Rep. LA-CC-06-012*, 01 2010.

[37] Elizabeth C Hunke, William H Lipscomb, Adrian K Turner, Nicole Jeffery, and Scott Elliott. Cice: The los alamos sea ice model documentation and software user's manual version 5.0 la-cc-06-012. *T-3 Fluid Dynamics Group, Los Alamos National Laboratory*, 2013.

[38] W. D. Hibler. A dynamic thermodynamic sea ice model. *Journal of Physical Oceanography*, 9(4):815 – 846, 1979.

[39] Keith W Oleson, David M Lawrence, Gordon B Bonan, Rosemary A Fisher, Peter J Lawrence, and Stefan P Muszala. Technical description of version 4.5 of the community land model (clm). *Technical description of version 4.5 of the Community Land Model (CLM)(2013) NCAR/TN-503+ STR*, 503, 2013.

[40] David M Lawrence, Rosie A Fisher, Charles D Koven, Keith W Oleson, Sean C Swenson, Gordon Bonan, Nathan Collier, Bardan Ghimire, Léo Van Kampenhout, Daniel Kennedy, et al. The community land model version 5: Description of new features, benchmarking, and impact of forcing uncertainty. *Journal of Advances in Modeling Earth Systems*, 11(12):4245–4287, 2019.

[41] Zachary M. Subin, William J. Riley, and Dmitrii Mironov. An improved lake model for climate simulations: Model structure, evaluation, and sensitivity analyses in cesm1. *Journal of Advances in Modeling Earth Systems*, 4(1), 2012.

[42] C. D. Koven, W. J. Riley, Z. M. Subin, J. Y. Tang, M. S. Torn, W. D. Collins, G. B. Bonan, D. M. Lawrence, and S. C. Swenson. The effect of vertically resolved soil biogeochemistry and alternate soil c and n models on c dynamics of clm4. *Biogeosciences*, 10(11):7109–7131, 2013.

[43] B. Drewniak, J. Song, J. Prell, V. R. Kotamarthi, and R. Jacob. Modeling agriculture in the community land model. *Geoscientific Model Development*, 6(2):495–515, 2013.

[44] W. J. Sacks, B. I. Cook, N. Buenning, S. Levis, and J. H. Helkowski. Effects of global irrigation on the near-surface climate. *Climate Dynamics*, 33:159–175, 2009.

[45] W. J. Parton, J. W. B. Stewart, and C. V. Cole. Dynamics of c, n, p and s in grassland soils: a model. *Biogeochemistry*, 5(1):109–131, 1988.

[46] Albenis Pérez-Alarcón, Patricia Coll-Hidalgo, Ricardo M. Trigo, Raquel Nieto, and Luis Gimeno. Cytrack: An open-source and user-friendly python toolbox for detecting and tracking cyclones. *Environmental Modelling & Software*, 176:106027, 2024.

[47] Irina Rudeva and Sergey K. Gulev. Climatology of cyclone size characteristics and their changes during the cyclone life cycle. *Monthly Weather Review*, 135(7):2568 – 2587, 2007.

[48] Robert E. Hart. A cyclone phase space derived from thermal wind and thermal asymmetry. *Monthly Weather Review*, 131(4):585 – 616, 2003.

[49] Jennifer Gahtan, Kenneth R. Knapp, Carl J. III Schreck, Howard J. Diamond, James P. Kossin, and Michael C. Kruk. International best track archive for climate stewardship (ibtracs) project, version 4.01, 2024.

[50] Kenneth R. Knapp, Michael C. Kruk, David H. Levinson, Howard J. Diamond, and Charles J. Neumann. The international best track archive for climate stewardship (ibtracs): Unifying tropical cyclone data. *Bulletin of the American Meteorological Society*, 91(3):363 – 376, 2010.

[51] NOAA National Centers for Environmental Information. International best track archive for climate stewardship (ibtracs) technical documentation, 2024.

[52] V. Masson-Delmotte, P. Zhai, H.-O. Pörtner, D. C. Roberts, J. Skea, P. R. Shukla, A. Pirani, W. Moufouma-Okia, C. Péan, R. Pidcock, S. Connors, J. B. R. Matthews, C. Yang, X. Zhou, and L. Steg. *Global warming of 1.5°C: Summary for policy makers*. IPCC – Intergovernmental Panel on Climate Change, Geneva, Switzerland, 2018.

[53] Thomas Knutson, Suzana J. Camargo, Johnny C. L. Chan, Kerry Emanuel, Chang-Hoi Ho, James Kossin, Mrutyunjay Mohapatra, Masaki Satoh, Masato Sugi, Kevin Walsh, and Liguang Wu. Tropical cyclones and climate change assessment: Part ii: Projected response to anthropogenic warming. *Bulletin of the American Meteorological Society*, 101(3):E303 – E322, 2020.

[54] Eun Jeong Cha, Thomas R. Knutson, Tsz-Cheung Lee, Ming Ying, and Toshiyuki Nakaegawa. Third assessment on impacts of climate change on tropical cyclones in the typhoon committee region – part ii: Future projections. *Tropical Cyclone Research and Review*, 9(2):75–86, 2020.